4-2021

DESIGN OF GRAPHENE-BASED SENSORS FOR NUCLEIC ACIDS DETECTION AND ANALYSIS

Asma' Wasfi Fayez Mustafa

United Arab Emirates University

College of Engineering

DESIGN OF GRAPHENE-BASED SENSORS FOR NUCLEIC ACIDS
DETECTION AND ANALYSIS
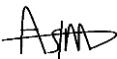
Asma' Wasfi Fayez Mustafa

This dissertation is submitted in partial fulfillment of the requirements for the degree
of Doctor of Philosophy

Under the Supervision of Professor Falah Awwad

April 2021

Declaration of Original Work

I, Asma' Wasfi Fayez Mustafa, the undersigned, a graduate student at the United Arab Emirates University (UAEU). I am the author of this PhD dissertation entitled "*Design of Graphene-based Sensors for Nucleic Acid Detection and Analysis*", hereby, solemnly declare that this dissertation is my own original research work that has been done and prepared by me under the supervision of Professor Falah Awwad, in the College of Engineering at UAEU. This work has not previously been presented or published, or formed the basis for the award of any academic degree, diploma or a similar title at this or any other university. Any materials borrowed from other sources (whether has been published or unpublished) and relied upon or included in my dissertation have been properly cited and acknowledged in accordance with appropriate academic conventions. I further declare that there is no potential conflict of interest with respect to the research, data collection, authorship, presentation and/or publication of this dissertation.

Student's Signature: _____   Date: 10/5/2021

Advisory Committee

1) Advisor: Professor Falah Awwad

Title: Professor

Department of Electrical Engineering

College of Engineering

2) Co-advisor: Professor Naser Naim Qamhieh

Title: Professor

Department of Physics

College of Science

3) Member: Dr. Mahmoud F. Al Ahmad

Title: Associate Professor

Department of Electrical Engineering

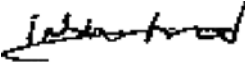College of Engineering

Approval of the Doctorate Dissertation

This Doctorate Dissertation is approved by the following Examining Committee Members:

1) Advisor (Committee Chair): Professor Falah Awwad

   Title: Professor

   Department of Electrical Engineering

   College of Engineering

   Signature _____   Date April 26, 2021

2) Member: Dr. Amine El Moutaouakil

   Title: Assistant Professor

   Department of Electrical Engineering

   College of Engineering

   Signature _____   Date April 26, 2021

3) Member: Professor Saleh Thaker

   Title: Professor

   Department of Physics

   College of Science

   Signature _____   Date April 26, 2021

4) Member (External Examiner): Professor Fathi M. Salem

   Title: Professor

   Department of Electrical and Computer Engineering

   Institution: Michigan State University, USA

   Signature _____   Date April 26, 2021

This Doctorate Dissertation is accepted by:

Dean of the College of Engineering: Professor James Klausner

Signature _James F. Klausner_   Date _14/6/2021_

Dean of the College of Graduate Studies: Professor Ali Al-Marzouqi

Signature _Ali Hassan_   Date _14/6/2021_

Copy ____ of ____

Abstract

DNA (Deoxyribonucleic Acid) is the blueprint of life as it encodes all genetic information. In genetic disorder such as gene fusion, Copy Number Variation (CNV) and single nucleotide polymorphism, Nucleic acids such as DNA bases detection and analysis is used as the gold standard for successful diagnosis. Researchers have been conducting rigorous studies to achieve genome sequence at low cost while maintaining high accuracy and high throughput. Quick, accurate, and low cost DNA detection approach would revolutionize medicine. Genome sequence helps to enhance people's perception of inheritance, disease, and individuality. This research aims to improve DNA bases detection accuracy, efficiency, and reduce the production cost, thus novel based sensors were developed to detect and identify the DNA bases. This work aims at first to develop specialized field effect transistors which will acquire real time detection for different concentration of DNA. The sensor was developed with a channel of graphite oxide between gold electrodes on a substrate of silicon wafer using Quantumwise Atomistix Toolkit (ATK) and its graphical user interface Virtual Nanolab (VNL). The channel was decorated with trimetallic nanoclusters that include gold, silver, and platinum which have high affinity to DNA. The developed sensor was investigated by both simulation and experiment. The second aim of this research was to analyze the tissue transcriptome through DNA bases detection, thus novel graphene-based sensors with a nanopore were designed and developed to detect the different DNA nucleobases (Adenine (A), Cytosine (C), Guanine (G), Thymine (T)). This research focuses on the simulation of charge transport properties for the developed sensors. This work includes experimental fabrication and software simulation studies of the electronic properties and structural characteristics of the developed sensors. Novel sensors were modeled using Quantumwise Atomistix Toolkit (ATK) and its graphical user Interface Virtual Nanolab (VNL) where several electronic properties were studied including transmission spectrum and electrical current of DNA bases inside the sensor's nanopore. The simulation study resulted in unique current for each of the DNA bases within the nanopore. This work suggests that the developed sensors could achieve DNA sequencing with high accuracy. The practical implementation of this work represents the ability to predict and cure diseases from the genetic makeup perspective.

Title and Abstract (in Arabic)

تصميم أجهزة مستشعرة من مادة الجرافين للكشف عن الحمض النووي

الملخص

الحمض النووي (DNA) هو مخطط الحياة لأنه يشفر جميع المعلومات الجينية مثل الاضطرابات الوراثية كما أنه يتم استخدام تسلسل الحمض النووي كمعيار ذهبي للتشخيص الناجح. أجرى الباحثون دراسات عديدة لتحقيق تسلسل الحمض النووي بتكلفة منخفضة مع الحفاظ على الدقة العالية والإنتاجية العالية حيث تم تصنيع أجهزة التسلسل التي أدت إلى تطور هذه التكنولوجيا. إن تسلسل الحمض النووي السريع والدقيق والمنخفض التكلفة من شأنه أن يحدث ثورة في الطب حيث أنه سيوفر ثروة من المعلومات الطبية لكل فرد. يهدف هذا البحث إلى تطوير وتصنيع جهاز لإيجاد تسلسل الحمض النووي بدقة وبسعر مناسب. سيتم تصنيع نوعين من المستشعرات (Sensors) في هذا المشروع حيث سيتكون الجهاز الأول من أقطاب كهربائية ذهبية وقناة من أكسيد الجرافيت (Graphite Oxide) على شريحة من السيليكون للكشف عن التراكيز المختلفة من الحمض النووي. كما سيتم إضافة جسيمات نانوية (nanoclusters) معدنية للجهاز ودراسة تأثيرها. بينما سيتكون الجهاز الثاني من الجرافين (Graphene) على شريحة وسيتم احداث ثقب بحجم النانو (nanopore) في منتصف طبقة الجرافين. وسيتم تمرير الحمض النووي بهذا الثقب وتمرير تيار كهربائي في الجهاز ودراسة للخصائص الكهربائية أثناء مرور الحمض النووي. وقد تمت ملاحظة أن قواعد الحمض النووي الأربعة (الأدينين والجوانين والسيتوزين والثايمين) ستؤثر على التيار الكهربائي بطريقة فريدة. وبالتالي فإن القراءات الناتجة عن مرور الحمض النووي أمكنت الباحثين من تمييز القواعد الأربعة وقراءة تسلسل الحمض النووي بدقة. يشير هذا العمل إلى أن المستشعرات المطورة يمكنها تحقيق تسلسل الحمض النووي بدقة عالية.

مفاهيم البحث الرئيسية: تسلسل الحمض النووي ، الجرافين ، أكسيد الجرافيت ، الأشرطة النانوية ، الثقوب النانوية ، النقل الإلكتروني ، جسيمات نانوية ، الترانزستور.

Acknowledgements

First of all, I would like to thank Allah for giving me the faith, luck and strength to successfully complete my work. My deepest thanks go to my husband, daughter, parents, mother in law and my family who have supported me, and given me strength and encouragement to complete this work. I would like to express my deepest thanks to everyone who helped me during this unforgettable period of my life.

I would like to thank and show my deep appreciation to my supervisor Prof. Falah Awwad for his unlimited support, and guidance. He was always approachable, punctual and provided me with precious knowledge and advice during this entire research work. I would like to thank Prof. Ahmad I. Ayesh, Department of Mathematics, Statistics and Physics, Qatar University, for his support and guidance. Also, I greatly appreciate and thank Prof. Naser Naim Qamhieh, Department of Physics, for his help and guidance and for his valuable discussions and feedback. My thanks extend to Prof. Rabah Iratni, Department of Biology, who provided me with materials, equipment and guidance for doing research. I would also like to thank my committee members for their guidance and valuable comments on my thesis. My acknowledgments are extended to all faculty members of the Department of Electrical Engineering and Department of Physics at United Arab Emirates University for their continuous support and encouragement.

Dedication

To my beloved parents, family, and friends

Table of Contents

List of Figures

List of Abbreviations

A	Adenine
AGNR	Armchair Graphene Nanoribbon
ATK	Quantumwise Atomistix Toolkit
C	Cytosine
CNV	Copy Number Variation
DFT	Density Functional Theory
DFTB	Density Functional Theory with tight binding
DG-ZGNR	Dual Gate Z-shaped Graphene Nanoribbon
DNA	Deoxyribonucleic acid
EDS	Energy-Dispersive X-Ray Spectroscopy
EH	Extended Hückel
EHT	Extended Hückel Theory
FET	Field Effect Transistor
G	Guanine
GGA	Generalized Gradient Approximation
GO	Graphene Oxide
HPC	High Performance Computing
LB	Lysogeny Broth
LCAO	Linear Combination of Atomic Orbitals
LDA	Local Density Approximation
MO	Molecular Orbitals
MOSFET	Metal Oxide Semiconductor Field Effect Transistor
NEGF	Non-equilibrium Green's Function

NiCr	Nickel-chrome
ONT	Oxford Nanopore Technologies
PCR	Polymerase Chain Reaction
PZ	Perdew–Zunger
QMF	Quadrupole Mass Filter
SC	Self-Consistent
SEM	Scanning Electron Microscope
SPR	Surface plasmon resonance
ssDNA	single stranded DNA
STEM	(Scanning) Transmission Electron Microscopy
STM	Scanning Tunneling Microscope
STO	Slater-type orbital
T	Thymine
TEM	Transmission Electron Microscopy
UHV	Ultra-high Vacuum Compatible System
UV-Vis	Ultraviolet-visible
VNL	Virtual Nanolab
ZGNR	Zigzag Graphene Nanoribbon

Chapter 1: Introduction

1.1 Overview

DNA Sequencing is one of the most important innovations during this decade. That is why it is highly important to achieve cheap, reliable and fast DNA sequencing approach. It is a vastly advancing technology to obtain the bases sequence in human genome. This sequence information significantly affects the recognition and medication of disease. Acquiring reliable, quick, and cheap DNA sequencing facilitates personalized medicine procedure where right medication will be given to patients. Each individual has his own unique DNA signature. Knowing this sequence could potentially mean that people might know many of the diseases, they could face during their lifetime. DNA Sequencing helps to interpret genetic data into clear answers enabling people to make informed decisions based on their genetic prepositions and risks. Analyzing DNA unlocks individual's Genetic profile and helps finding the genetic risk and common diseases.

Finding the DNA sequence will (i) identify individuals because each individual has a unique genetic sequence, (ii) determine Gene Structure, (iii) find genetic disorder, and (iv) develop personalized medicine to improve human health.

Several studies have been conducted by researches to fabricate sensors that will achieve cheap genome sequencing with accurate and quick results. Recently, nanotechnology-based methodologies such as nanopore sequencing approaches are being deeply studied and established. Various nanopore methods have been developed, explored, and studied to pave the way for successful and reliable sequencing. Due to graphene unique properties and structure, a variety of graphene-based biosensors were

proposed and studied theoretically and experimentally. There are various approaches for DNA sequencing using graphene such as nanopores, nanoribbons, nanogaps, and DNA physisorption in graphene (Heerema & Dekker, 2016; Wasfi, Awwad, & Ayesh, 2018). DNA sequencing using graphene nanopore and nanogap methodology will be applied in this research.

1.2 Objectives

This work was aimed at first building a specialized Field Effect Transistor (FET) that performs real-time detection of the concentration of the DNA in a biological fluid sample. The second aim of this work was to analyze the cell/ tissue through DNA bases detection. To achieve the second objective, a device based on nanoporous material was designed and tested to identify the signatures of each nucleotide (Adenine, Cytosine, Guanine, and Thymine). Moreover, this research work focuses on the software simulation of charge transport properties of the above devices.

This work involves software simulation and fabrication experiments studies of the electronic as well as structural properties of these sensing devices. The novel devices designed in this work assist the international efforts that aim to determine the DNA bases using sensitive, cheap, and reliable methods. The results obtained from this work were analyzed and compared to the software simulation results based on molecular dynamics, as well as the previous relevant studies.

1.3 Relevant Literature

In this section, the significance, history, advances, generations, applications, methods, and potentials of DNA detection are reviewed.

1.3.1 DNA

DNA is made up of nucleotides. Each nucleotide consists of a sugar group, a phosphate group and a nitrogen base. The four types of nucleobases are Adenine (A), Thymine (T), Guanine (G) and Cytosine (C). The chemical structure of DNA is displayed in Figure 1. The DNA sequence or the genetic code is determined by the order of the four nucleobases. DNA sequencing is the process of reading off the sequence of bases within a DNA molecule. It includes all techniques or methods used in determining the order of the four bases A, G, C, and T in a DNA strand. DNA sequencing has become substantial in biological research, and in various fields such as biotechnology, medical diagnosis, forensic biology and medical systems. DNA sequencing is a promising process that is why there has been a huge effort to develop DNA sequencing techniques through the years. The advancement toward fast, reliable and cheap sequencing has witnessed huge improvement since the Human Genome Project in 2001 (Lander et al., 2001) .
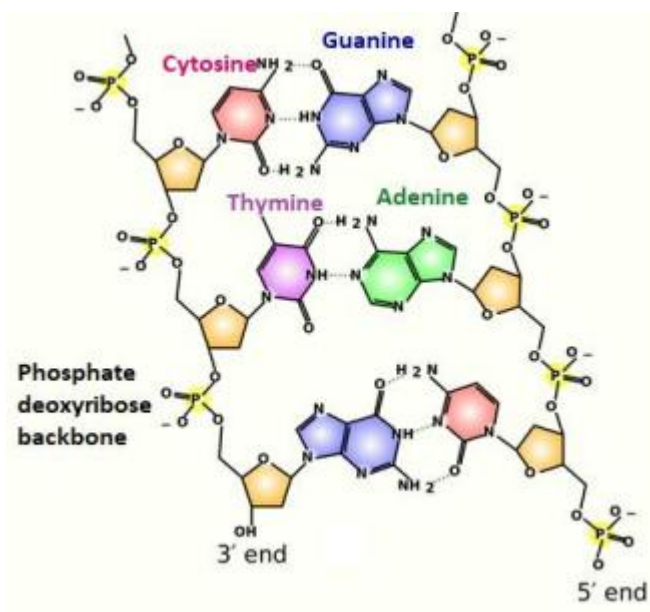
Figure 1: DNA Chemical Structure. (Wasfi et al., 2018)

1.3.2 History of DNA Sequencing

Over the last fifty years a huge number of DNA sequencing techniques were established. This period of time witnessed a massive improvement in these techniques from sequencing few DNA bases to millions of DNA bases such as a whole gene.

1.3.2.1 First-generation DNA Sequencing

In 1965, the first whole nucleic acid sequence was produced (Holley et al., 1965) and a related technique was introduced during the same year by Fred Sanger (Sanger, Brownlee, & Barrell, 1965). The first complete protein-coding gene was sequenced in 1972 (Jou, Haegeman, Ysebaert, & Fiers, 1972). Few years later, a complete nucleotide sequence of bacteriophage MS2 RNA was performed (Fiers et al., 1976). During mid-1970s Sanger developed a new rapid technique 'chain-termination' to determine the sequence of nucleotide in single strand DNA and Maxam and Gilbert's used chemical agents to break the DNA molecule to its bases in order to find out the sequence (Maxam & Gilbert, 1977; Sanger & Coulson, 1975). Sanger and Maxam techniques were adopted widely and considered as the birth of first generation DNA sequencing. These first generation techniques provided a very short read length where DNA is broken into short fragments before sequenced.

1.3.2.2 Second-generation DNA Sequencing

Second generation techniques differed from the previous ones in that they did not affect nucleotide identity. These techniques started in 2005 with a report of parallel pyrosequencing from 454 Life sciences (biotechnology company) (Margulies et al., 2005). Sequencing machines produced by 454 Life sciences allowed the parallelization of the sequencing reactions which increased the DNA amount that can be sequenced

in one run (Margulies et al., 2005). Various parallel sequencing techniques were established after the success of 454 Life sciences' sequencing machines such as Solexa technique (Voelkerding, Dames, & Durtschi, 2009). Another notable second generation sequencing technique is "DNA nanoballs" which is based on sequence by ligation (Drmanac et al., 2010). In 2011 one more remarkable technique called post-light sequencing was developed by Jonathan Rothberg (Rothberg et al., 2011). Illumina sequencing techniques which provides the lowest cost and highest throughput is considered the most successful second generation sequencing technique (Greenleaf & Sidow, 2014).

1.3.2.3 Third-generation DNA Sequencing

Third generation techniques are those capable of single molecule sequencing without the need for amplification. These techniques will lead to cost reduction and procedure simplification. One of the most widely used third generation techniques are the single-molecule real-time sequencing techniques (Clarke et al., 2009). Nanopore sequencing is the most promising third generation technique. Nanopore techniques include biological, solid state and hybrid nanopores. Oxford Nanopore Technologies (ONT) is one of the leading companies in nanopore technology (Clarke et al., 2009; Eisenstein, 2012). Nanopore sequencing is based on the conductivity of the pore where the ion currents change when the pore is blocked by a nucleobase. Each nucleobase blocks the ionic current in a different way (Branton et al., 2008). Nanopore techniques do not need polymerase chain reaction PCR amplification or other molecule modification and promise cost reduction, speed increment of DNA sequencing, error rate reduction and an increment in the read length of DNA fragments. The crucial challenge with nanopore technique is slowing down the DNA translocation speed

through the nanopore.

1.3.3 Graphene for DNA Sequencing

Graphene-based DNA sequencing has grown tremendously because of graphene unique structure and properties. Graphene or Graphene Oxide (GO) is a unique material that provides novel opportunities and approaches for DNA sequencing. Graphene is a one-layer carbon atoms that are bonded in a repeating hexagon pattern. It is an extremely thin material that is considered two dimensional. Graphene has a number of superb properties: it is (i) extremely thin, (ii) highly strong because of the strong bonds between the carbon atoms, (iii) very flexible, (iv) transparent, (v) conductive since it allows electrons to move quickly and (vi) cheaply produced (Sheka, 2014). Graphene and its derivatives such as Graphene Oxide and Graphite Oxide are unique materials that provide novel opportunities and approaches for DNA detection. Graphene Oxide is an oxidized form of graphene, while Graphite Oxide is multilayer of Graphene Oxide. There are various graphene-based DNA sequencing approaches.

Graphene nanoribbons can be produced by cutting graphene through a method called chirality vector. The two types of Graphene Nanoribbons (GNRs), based on carbon atoms arrangement and edge termination, are: Zigzag Graphene Nanoribbons (ZGNR) and Armchair Graphene Nanoribbons (AGNR) (Qiu, Nguyen, & Skafidas, 2014). AGNR behaves like a semiconductor or a metal depending on the number of carbon chains within the width which is denoted by Na. For $Na = 3p + 2$, AGNR is metallic, while for $Na = 3p + 1$ or $Na = 3p$, it is semiconducting, where p represents a positive integer. Alternatively, ZGNR behaves like a metal (Qiu et al., 2014).

1.3.3.1 Graphene-Based DNA Sequencing Approaches

1.3.3.1.1 Graphene Nanopore for DNA Sequencing

The first approach is ionic current detection through a graphene nanopore where DNA molecule bases block the ionic current passing through nanopore in a graphene sheet as shown in Figure 2. The concept of DNA sequencing through graphene nanopore is simple, where a single nanopore is created in a graphene membrane immersed in an electrolyte solution. Nanopores are fabricated in graphene membrane using Focused Electron Beam (FEB) or Focused Ion Beam (FIB) drilling . An ionic current will be induced through the pore after applying a voltage to the membrane and ions will be driven through the pore. The graphene membrane has a pore that is sandwiched between two compartments containing an electrolytic solution. Then the voltage is applied across the graphene membrane. After that, the ionic current is induced through the pore. DNA bases will pass through the pore and each base will affect the ionic current differently. The duration of current blockage and variations in its magnitude will provide an indicator to determine the sequence of the DNA bases.

Nanopores are categorized into three types: (i) Biological nanopores based on proteins, (ii) solid state nanopore fabricated using solid substrates such as graphene and (iii) hybrid which is a combination of both. In general, the channel constituting the solid-state nanopores is considered to be very long compared to the DNA bases. It is approximately 100 times the distance between two DNA bases which is a major limitation (Schneider et al., 2010). Graphene provides an ideal solution for this issue since graphene thickness is $\sim$0.3 nm which is only one atomic layer (Novoselov et al., 2004). This means that graphene thickness is the same as the distance between two bases.

Solid-state nanopores such graphene nanopores have many advantages: high stability, lower sensitivity and well-suited for massive upscaling. On the other hand, it has increased noise levels and lack of atomic control. The simulations revealed some challenges with DNA sequencing via solid-state nanopores, as they showed that sequencing errors occur since the bases move stochastically through the pore and conformational fluctuations of the bases occur (Heerema & Dekker, 2016).
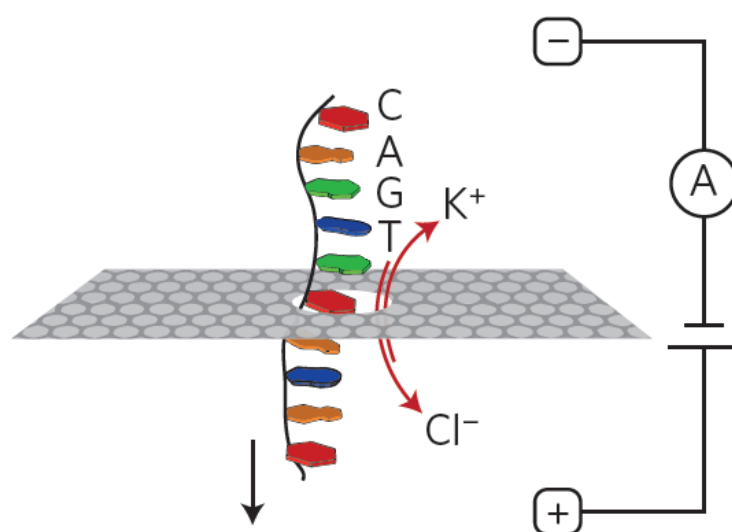
Figure 2: Schematic display for DNA sequencing through graphene nanopore. (Heerema & Dekker, 2016).

1.3.3.1.2 Tunneling across a Graphene Nanogap

Figure 3 displays tunneling across a graphene nanogap approach where each base within a nanogap leads to a different tunneling current through the gap since different bases have different electronic level of structure. The idea is to measure the conductance through two graphene electrodes and to control the current variations when DNA bases go through the nanogap. When different DNA bases fall within the voltage window of the two electrodes, a special and different current will be noticed (Heerema & Dekker, 2016). The transverse conductance of the DNA passing through

the graphene nanogap results in a nonlinear current-voltage characteristic where the current changes by 5 orders of magnitude (the reference for the change is 10). This will help in finding out the nucleobase type independently without being affected by the width of the nanogap. The expected sequencing error is based on the nanogap width. The nanogap sequencing can be done with a very small gap with a size ranging from 1-2 nm (Prasongkit, Grigoriev, Pathak, Ahuja, & Scheicher, 2011) . Graphene layers thickness is not critical when using this approach since the tunneling current is sensitive to the distance between the nucleobase and the electrodes. In this approach, the use of graphene layer as the membrane and electrodes resolves the issue of fabricating nanoelectrodes aligned with the nanogap.   (Arjmandi-Tash, Belyaeva, & Schneider, 2015; Bayley, 2010; Heerema & Dekker, 2016).

Graphene nanogaps can be fabricated using various methods such as nanolithography with an STM (Tapasztó, Dobrik, Lambin, & Biró, 2008), electromigration (Venema et al., 1997), local anodic oxidation (Weng, Zhang, Chen, & Rokhinson, 2008), TEM nanofabrication (Fischbein & Drndic, 2008), or catalytic nanocutting (Ci et al., 2008; Datta, Strachan, Khamis, & Johnson, 2008). The optimal nanogap width is 1-1.5 nm to achieve single stranded DNA (ssDNA) sequencing.

There are many theoretical studies for DNA detection using graphene nanogaps, but till now there is no experiment on DNA sequencing. This approach is promising, but unfortunately there are no experimental studies. The experimental challenges for DNA detection using graphene nanogap are (i) the small tunneling current, (ii) large fluctuations, (iii) the high DNA translocation speed and (iii) the high noise rate (Heerema & Dekker, 2016).
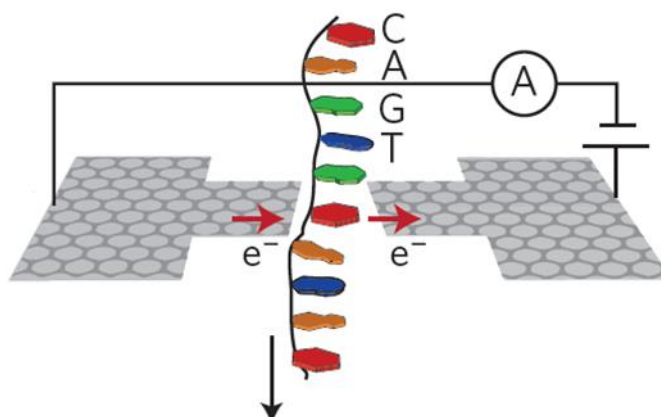
Figure 3: Schematic display of DNA sequencing using tunneling across graphene nanogap. (Heerema & Dekker, 2016).

1.3.3.1.3 In-plane Transport of a Graphene Nanoribbon with a Nanopore

Figure 4 displays the third approach which is in-plane transport of graphene nanoribbon where DNA bases modulate the ionic current passing through graphene nanoribbon differently. This approach has an advantage over the previous one since the current in the nanoribbons is larger. It is predicted that graphene nanoribbons will provide better base recognition results (Heerema & Dekker, 2016).

The interactions between the nucleobases and the graphene pore modulate the nanoribbon current. The different coupling strength of the nucleobases with the graphene nanoribbon enabled the researchers to identify the base type and find the DNA sequence (Heerema & Dekker, 2016). In this approach, the nucleobases pass through the pore in graphene nanoribbon. The conductance spectra and the charge densities were analyzed for each nucleobase in the graphene nanopore. The fabricated device has enough sensitivity to distinguish between the different nucleobases. This technique is helpful for developing fast and low-cost DNA sequencing (Nelson,

Zhang, & Prezhdo, 2010). In 2013, the first experimental study for DNA sequencing using DNA translocation through graphene nanoribbons with nanopores was reported (Traversi et al., 2013). This study showed that graphene nanoribbon transistor can be integrated with solid state nanopore to fabricate a DNA biosensor. This graphene nanoribbon transistor consists of two gold electrodes connected through a graphene nanoribbon channel where a nanopore is placed in the middle and a gate underneath the channel. Using this sensor, DNA sequence is detected by measuring the ionic current drops and the changes in the transistor local voltage. The fabricated device measures the ionic current in real time to accomplish real time sequencing (Traversi et al., 2013).
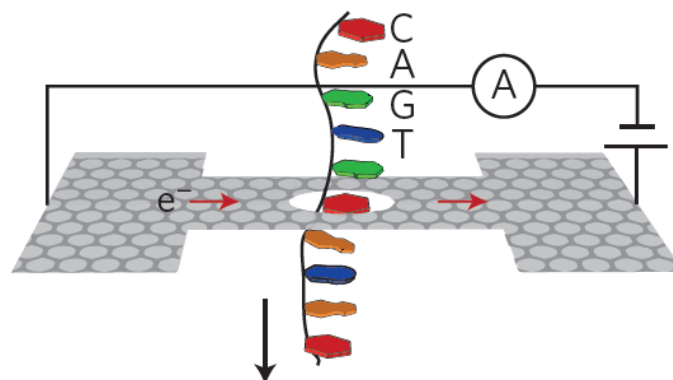
Figure 4: Schematic display of in-plane transport of a graphene nanoribbon with a nanopore. (Heerema & Dekker, 2016). The red arrow indicates the electrons direction which is the opposite to the positive current direction and the black arrow indicates the DNA strand direction.

1.3.3.1.4 DNA Physisorption on Graphene Nanostructures

This approach is shown in Figure 5. It is based on the graphene current modulation due to DNA physisorption, which is located on top of the graphene layer, The different measurements are due to the variations in the electrochemical activity, or the adsorption and desorption of DNA strand (Dontschuk et al., 2015; Vicarelli,

Heerema, Dekker, & Zandbergen, 2015).

Due to graphene-DNA complex binding nature, various mechanisms have been studied such as electrostatic, van der Waals, π–π stacking and hydrophobic interactions (Oliveira-Brett & Paquim, 2003). Studies showed that single-stranded DNA binds to graphene strongly compared to double-stranded DNA. The strength of the interaction varies based on the DNA bases polarizability (Lee, Choi, Kim, Scheicher, & Cho, 2013; Sh, Scheicher, Ahuja, Pandey, & Karna, 2007). It was reported that G-base has stronger binding to graphene compared to the other DNA bases (A, T, and C), while A, T, and C bases have similar or lower interaction strength compared to G-base (Antony & Grimme, 2008; Le, Kara, Schröder, Hyldgaard, & Rahman, 2012; Sh et al., 2007).

DNA adsorption onto graphene nanostructures such as nanoribbons can potentially help in identifying the DNA bases. The DNA adsorption studies showed that the base fluctuations are minimized using this approach which leads to lower noise rate (Heerema & Dekker, 2016).
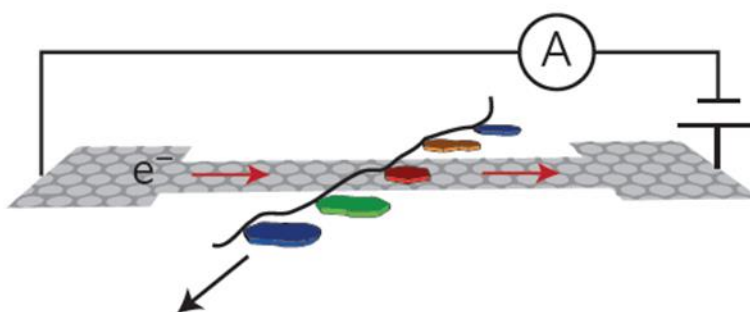
Figure 5: Schematic display of DNA sequencing using DNA physisorption on graphene. (Heerema & Dekker, 2016).

1.3.4 DNA Sequencing Applications

DNA sequencing ultimate goal is to achieve cheap, fast, and accurate sequencing. Below are some of the DNA sequencing applications:

1.3.4.1 Developing Personalized Medicine

Three decades ago, one drop of human blood was used to identify to which one of the four groups the human blood belongs. Nowadays, this drop is used to identify the genetic information of human and provide interesting opportunities in biomedical treatment (Schuster, 2008). Nanopore sequencing technologies enabled better thoughtful of the basis of genetic diseases. Recent developments have explained the clinical applications of sequencing techniques in describing the genetic mechanisms of tumor development pathways, inherited diseases, and specific medication response (Jones et al., 2009). Although the difficulties facing the genome analysis and the needed studies to make sure that these technologies will be applied within clinics in an ethically and medically responsible way, latest genome findings and the developed genome sequencing potential are showing a promising future of personalized treatment and individualized medicine (Robinson et al., 2011). Researchers are still arguing the need for healthy people should sequence their genome.

Other than finding a new way for drugs generation, diseases prevention, and treatment methods, DNA sequencing techniques can be used to achieve better knowledge of genotype-phenotype connections, offering precious details regarding susceptibility to diseases, defining family pedigrees as well as predicting individual's adaptability and vulnerability to an environment. Moreover, various efforts are done to use the DNA sequence to investigate the associated genes with skin aging and

develop personalized skin care products.

1.3.4.2 Better Perception of Ourselves

Genome sequencing can be used to obtain better insight of species which is hard to be cultivated inside the lab such as archaea in marine sediments (Lloyd et al., 2013) or to evaluate the diversity of genes encoded from microbial communities (Hugenholtz & Tyson, 2008).

1.3.4.3 Safe Food

The entire genome sequencing for the meat of animals, food from plants, and wheat bread is highly important for their genetic improvement and evolution (Ling et al., 2013). The quick analysis of genome for foodborne pathogens will enable us to have a better understanding of outbreaks and develop better diagnostic (Chin et al., 2011).

1.3.4.4 Data Storage

DNA is considered as a stable material to store data, which encodes the entire required information for the function and development of living organisms. Thus, data can be stored in the DNA base sequence. It is reported in Nature journal that approximately 5 megabits of data were encoded completely by Agilent Technologies' OLS (Oligo Library Synthesis) and restored with accuracy of 100% (Goldman et al., 2013). This process was highly expensive. However, the reduction in the cost of DNA sequencing and synthesis is showing a promising future for finding a practical way for DNA based data storage.

1.3.5 Nucleic Acid Detection via Field Effect Sensors

Immediate bio-molecule detection is highly critical in several areas such as health and food analysis (Bunney et al., 2017; Haque, Li, Wu, Liang, & Guo, 2013; Pantelopoulos & Bourbakis, 2010) toxicity identification (Ligler et al., 2003), and cancer detection (Tothill, 2009). Traditional detection methods of bio-molecules require labels which provide high sensitivity, but these methods don't provide real time detection and they are costly. Various studies are aiming to design label free sensors to detect the target molecule, where a number of transduction techniques are being tested by researchers. Surface Plasmon Resonance (SPR) method achieved high sensitivity for label free biological detection (Homola, 2008; Jordan, Frutos, Thiel, & Corn, 1997; Nelson, Grimsrud, Liles, Goodman, & Corn, 2001). Various sensors such as carbon nanotube (Allen, Kichambare, & Star, 2007), and silicon nanowire Field Effect Transistors (FETs) are showing high sensitivity (Curreli et al., 2008; Stern, Vacic, & Reed, 2008). One-dimensional based sensors such as carbon nanotubes and nanowires are being utilized for immediate identification of various bio-molecules with high sensitivity (Bunimovich et al., 2006; Duan et al., 2012; Ganguly et al., 2009; Hahm & Lieber, 2004; Mu, Droujinine, Rajan, Sawtelle, & Reed, 2014; Okuda et al., 2012; Palaniappan et al., 2010; Wang, Chen, Lin, Fang, & Lieber, 2005; Zheng, Patolsky, Cui, Wang, & Lieber, 2005).

The first biosensor is an enzyme electrode sensor, and it was introduced in 1962 by Clark and Lyons (Clark & Lyons, 1962). After that, various bio-molecular sensors and mechanism emerged. One type of the most interesting mechanism is FET based sensors due to their novel features such as quick development, cheap production, fast response, and high sensitivity (Syu, Hsu, & Lin, 2018). Moreover, the availability

of mature manufacturing techniques offers the advantage of integration with other systems and circuits which is highly important in sensors development. Nanomaterial based FETs are promising candidates for bio-molecular detection by utilizing electronic measurements (Veigas, Fortunato, & Baptista, 2015; Zhang & Lieber, 2016). Transistor-based sensors consist of three electrodes: source, drain, and gate where the channel connecting the two electrodes works as the biological detection area that interacts with the molecules to sense their electrical measurements, concentrations, and presence (Chaplin & Bucke, 1990).

The current passing through the source and drain can be adjusted by manipulating the gate and source potential. The current is generated by carriers such as holes or electrons. The type of carriers depends on the type of semiconductor (n-type or p-type). N-Channel Metal Oxide Semiconductor Field Effect Transistors (MOSFETs) use electron flow as the charge carrier, while P-Channel MOSFETs use hole flow as the charge carrier. When a negative gate potential is applied to the n-type MOSFET, a depletion layer is formed and works as an insulator. While, when positive gate potential is applied to the n-types MOSFET, it attracts the electrons to the surface of the MOSFET and a conductive channel is formed which allows the current to pass across the source and drain. For p-type MOSFETs the opposite effect occurs. The channel conductance can be changed by the gate voltage where it can be changed from OFF to ON. During the ON state, the current flowing between the source and drain can vary with both drain voltage and gate voltage. The device transfer characteristics and electrical parameters allow the evaluation of the device performance such as carriers mobility, threshold voltage, and ON/OFF current ratio (Wu, Mu, Wang, & Zhao, 2018).

Field Effect Transistors (FETs) are considered the basis for developing new approaches to detect and characterize the DNA because of FET's quick measurement capabilities and high signal to noise ratio (Wu et al., 2018). In recent years, biological detection via field-effect devices has spread rapidly. In specific, FET is considered one of the most common methods in electrical DNA characterization and detection (Wu et al., 2018).

Nanotechnology evolution triggers the utilization of nanostructures such as nanotubes, nanowires, and nanoclusters in the bio-molecular detection field. It is highly important to take into consideration the material used to fabricate the bio-molecular transistor-based sensor. Graphene has outstanding characteristics such as high mobility (Bolotin et al., 2008; Wasfi et al., 2018), very large area (Chandran, Li, Ogata, & Penner, 2017), ultra-high mechanical strength (Li, Liu, Sun, & Gao, 2015), and unique electrical properties (Wakabayashi, Takane, Yamamoto, & Sigrist, 2009) which made it the perfect material in bio-molecular transistor applications. Graphene is considered the ideal membrane for DNA identification (Akhavan, Ghaderi, & Rahighi, 2012; Antony & Grimme, 2008; Heerema et al., 2018; Sathe, Zou, Leburton, & Schulten, 2011; Sh et al., 2007; Torrisi & Carey, 2018; Wang et al., 2011; Wu, Kempaiah, Huang, Maheshwari, & Liu, 2011) since transistor-based sensors with graphene channel offer quick, accurate, real-time, and label-free detection. But it is inefficient to produce large amounts of graphene membranes. Therefore, graphite oxide is being used as an alternative. Graphite oxide can be used as a promising alternative of graphene since it is easier to produce, more economical, and has the required sensing features. Graphite oxide is attracting researchers' interest since it can be easily diluted in water and used in various applications such as nano-electronic

devices (Scheuermann, Rumi, Steurer, Bannwarth, & Mülhaupt, 2009).

1.3.6 Metallic Nanoclusters

Metal nanoculsters are made of few atoms approximately in tens. These nanoclusters consist of single or multiple elements and are characterized by their attractive optical, electronic, and chemical properties. As such, decorating the sensor with metallic nanoclusters improves its sensitivity and response time (Said et al., 2018; Said et al., 2017). Additionally, the nanoclusters have the ability to change the surface to volume ratio of the sensor (Ayesh, Mahmoud, Ahmad, & Haik, 2014). Nanoclusters can be generated using an inert gas aggregation technique inside an Ultra-High Vacuum Compatible system (UHV) (Ayesh, Ahmed, Awwad, Abu-Eishah, & Mahmood, 2013) which has some advantages over other chemical techniques such as high purity and size selection (Ayesh, Karam, Awwad, & Meetani, 2015; Ayesh, Thaker, Qamhieh, & Ghamlouche, 2011).

Noble metal nanoclusters have been vastly used for diverse applications including biomedical ones (Akhtar, Panwar, & Yun, 2013; Demirbas, Yilmaz, Ildiz, Baldemir, & Ocsoy, 2017; Elahi, Kamali, & Baghersad, 2018; Rai, Ingle, Birla, Yadav, & Santos, 2016; Xu, Peng, Yu, & Zheng, 2017) where of the most used noble metals nanoclusters are gold, silver, and platinum. Noble bimetallic and trimetallic nanoclusters are attracting researchers' interest because of the possibility to design their properties by controlling their composition, biocompatibility (Liu, Wang, & Li, 2012; Srinoi, Chen, Vittur, Marquez, & Lee, 2018; Toshima & Yonezawa, 1998; Zhang, Ahn, Kim, Wu, & Qin, 2018), and surface modifications (Adekoya, Dare, & Mesubi, 2014; Zhang, Xie, Lee, Zhang, & Boothroyd, 2008). Bimetallic and trimetallic

nanoclusters have diverse morphology (Akbarzadeh, Abbaspour, Mehrjouei, & Kamrani, 2018; Rodriguez-Proenza et al., 2018), improved antimicrobial action (Yadav et al., 2018), enhanced catalytic activity (Fauzia et al., 2019; Huang et al., 2017; Li et al., 2018; Pandey & Pandey, 2016; Sahoo, Tripathy, Dehury, & Patra, 2015; Zhang et al., 2014), very good stability (Carrillo-Torres et al., 2016; Li & Du, 2017), and high sensitivity and selectivity (Li, Zheng, Guo, Qu, & Yu, 2019; Liu, Yan, Lai, & Su, 2019; Zhai et al., 2018). As an example of composite metallic nanoclusters, mixing Au with Ag improves the antibacterial activity and the therapeutic concentration because of the strong electronic ligand impact. Ag/Au/pt trimetallic composite have shown impressive outcomes in bio-sensing applications (Yadav et al., 2018). These promising characteristics are assigned to the multi-functional influence stimulated by two or three metals within the nanocluster. Previous work shows that using trimetallic nanocluster such as Cu/Au/Pt has stronger catalytic activity than bimetallic or monometallic nanoclusters. Therefore, trimetallic nanoclusters can be investigated for biosensing applications such as nucleic acid, cancer cell and glucose detection (Wu et al., 2019; Ye et al., 2019).

1.3.7 Atomistic Software Methods

In this section, the methods used to study nanoscale sensors are presented. The calculation process for charge transport through the nanoscale sensors is explained. Then, the actual methods used in generating the calculations are demonstrated.

1.3.7.1 Molecular Sensors Charge Transport

The molecule can be managed as a group of nuclei where the electrons are represented by wave functions named Molecular Orbitals (MO) (Petrucci, Harwood,

Herring, & Madura, 2007). Molecule orbitals are discrete for an isolated molecule. The electrons fill the orbitals with low energy first as explained by Pauli exclusion principle (Pauli, 1925). The system Fermi-level must align to reach equilibrium when a molecule is placed and coupled among two metallic electrodes. Thus, molecule orbitals above Fermi-level will be empty of electrons, while molecule orbitals below Fermi-level will be filled with electrons. The coupling induced charge and potential perturbation produce a shift in the molecular levels relative to the electrode's Fermi level (Xue & Ratner, 2003). The occupied levels migrate upwards and the unoccupied ones migrate downwards in energy. This phenomenon can be attributed to the formation of image charges in the electrodes owing to the movements of electrons (either added to or removed from the molecules) (Datta, 1995; Xin et al., 2019).. Heisenberg's uncertainty principle describes the broadening in the energy level as displayed in Equation 1.1 :

$$\Delta t \gamma = \hbar \qquad (1.1)$$

Δt refers to the time needed for an electron to go between two electrodes within the molecule orbital (Datta, 2005), γ represents the broadening, $\hbar = h/2\pi$, and h refers to planck's constant .

Assuming a specific bias is applied to the two electrodes, each electrode will act differently. The left electrode prefers to fill the molecular orbital since it is less than its chemical potential while the right electrode prefers to empty it since it is more than its chemical potential(Mahmoud & Lugli, 2012). This non-equilibrium state leads to flow of charges across the molecule (Mahmoud & Lugli, 2012; Xin et al., 2019).

It is possible to fill each orbital with two electrons only. The required electrons number by the electrodes to fill the molecular orbital are calculated using Equation 1.2 and Equation 1.3:

$$N_L = 2f(E_{MO} - \mu_L) \tag{1.2}$$

$$N_R = 2f(E_{MO} - \mu_R) \tag{1.3}$$

$f(E - E_F = \frac{1}{1+e^{\frac{E}{KT}}})$, represents the Fermi equation, E_{MO} refers to molecular orbital energy, and μ_L, μ_R is the chemical potential of the left and right electrodes, respectively. The current from left electrode is calculated as in Equation 1.4:

$$I_L = e\frac{N_L - N}{\Delta t} = e\frac{\gamma_L}{\hbar}(N_L - N) \tag{1.4}$$

N refers to the actual electrons number in the molecular orbital and γ_L is the broadening due to the left electrode coupling (Mahmoud & Lugli, 2012). The current equation from the right electrode is the same and calculated using Equation 1.5:

$$I_R = e\frac{\gamma_R}{\hbar}(N_R - N) \tag{1.5}$$

Kirchhoff current law states that the negative current coming from the right electrode is equal to the current from the left electrode $-I_R = I_L$. Therefore, the actual number of electrons can be calculated using Equation 1.6:

$$N = \frac{\gamma_L N_L + \gamma_R N_R}{\gamma_L + \gamma_R} \tag{1.6}$$

By substituting in Equation 1.5, the current magnitude can be calculated using

Equation 1.7:

$$I = \frac{2e}{\hbar} \frac{\gamma_L \gamma_R}{\gamma_L + \gamma_R} |f(\mu_L, E_{MO}) - f(\mu_R, E_{MO})| \tag{1.7}$$

It was supposed that the whole molecule orbital contributes in the conduction. But, the

broadening compels the level of energy from a density of states $D(E)$, where

$\int_{-\infty}^{\infty} D(E) = 1$. This changes Equation 1.7 where only the states located between the

chemical potentials of the two electrodes contributes in the current. Therefore, the

updated Equation 1.8 is as below:

$$I = \frac{2e}{\hbar} \frac{\gamma_L \gamma_R}{\gamma_L + \gamma_R} \int_{\mu_L}^{\mu_R} D(E) |f(E - \mu_L) - f(E - \mu_R)| dE \tag{1.8}$$

In the previous discussion, the energy level of each molecule orbital which

contributes in the conduction is fixed before and after bias which is not accurate for

small devices. The number of electrons that occupies the molecule orbitals is different

than the number calculated from Equation 1.6. The induced charge interacts with

molecule charges and the molecular nuclei which will result in shifting the molecule

orbitals. The calculation should include the new state of the molecule orbitals to get

the actual number of charges. The procedure is required to be iterative till the charge

variation among two iterations is lower than the required accuracy. This procedure is

called the self-consistent calculations.

The effect of the induced charges is less when the molecules' size increase.

This behavior is noticed in large molecules where the molecule orbitals position hardly

changes due to different biases.

1.3.7.2 Background of Simulation Methods

The nanoscale sensors charge transport is generated by Non-Equilibrium Green's Function Formalism (NEGF). In order to evaluate the device electronic structure, NEGF needs to be coupled to either semi-empirical approaches or first-principle approaches. These approaches are illustrated in this section.

1.3.7.2.1 Molecule's Schrödinger

A wave function Ψ can be used to describe any system based on quantum mechanics. Moreover, a wave function utilizing Schrödinger equation can be used to describe chemical system such as molecule. Schrödinger equation assumes that the observable property of the system is the Energy (E) and introduces the Hamiltonian $\hat{H}$ to characterize the system total energy. Thus, the Schrödinger equation used to describe the molecular system is written as Equation 1.9:

$$\hat{H}\Psi = E\Psi \qquad (1.9)$$

The system energy is usually defined by five components, in the absence of any magnetic or electric effects. These components are: nuclei-electron interaction, inter-nuclei repulsion, inter-electron interaction, and the kinetic energies of both nuclei and electrons. The nuclei kinetic energy can be ignored in calculation because its movement can be discarded when compared with electron movement. For fixed nuclei coordinate, inter nuclei repulsion is constant. Moreover, wave functions are fixed for constant terms. Thus, these terms are not needed to solve Schrödinger equation. This kind of approximation is recognized as Born-Oppenheimer approximation which

makes it possible to compute large molecules wave-functions (Born & Oppenheimer, 1927). Thus, the Hamiltonian can be calculated as Equation 1.10:

$$\hat{H} = -\sum_i \frac{\hbar^2}{2m_e} \nabla_i^2 - \sum_{i<j} \frac{e^2}{r_{ij}} + \sum_i \sum_k \frac{e^2 Z_k}{r_{ik}} \qquad (1.10)$$

m_e refers to the electron mass, ∇^2 is Laplacian operator, the indexes of j and i run over electrons, k runs over nuclei, Z is the atomic number, r_{ik} is the interval between nucleus k and electron i, and r_{ij} is the interval among the electrons j and i.

1.3.7.2.2 Secular Equation Derivation

It was noticed that substituting infinite wave functions in Equation 1.9 results in a different energy eigenvalue for each one of them. Since the real system usually has the lowest ground state energy, Ψ_o can be assumed to be the best wave function to describe the system with the lowest energy E_o. Equation 1.9 can be regenerated as below where any guessed wave function Ψ_G results in eigenvalue E_G greater or equal to E_o which results in Equation 1.11.

$$\hat{H}\Psi_G \geq E_o \Psi_G \qquad (1.11)$$

The equation was multiplied by Ψ_G and integrated over space as shown below:

$$\int \Psi_G \hat{H}\Psi_G \, dr \geq \int \Psi_G E_o \Psi_G \, dr$$

$$\frac{\int \Psi_G \hat{H}\Psi_G \, dr}{\int \Psi_G \Psi_G \, dr} \geq E_o \qquad (1.12)$$

The quality of the guessed wave function can be estimated from the calculation of the

left side of the above Equation 1.12; this is called the variational principle.

Ψ_o can be assumed to be a linear combination of wave functions which results in a critical rule in computational chemistry called as the Linear Combination of Atomic Orbitals (LCAO) approximation for molecular orbitals (Lennard-Jones, 1929). This means that good approximation for molecular wave function can be calculated using the linear combination of atomic orbitals (Φ_i).

$$\Psi_G = \sum_{i=1}^{N} c_i \Phi_i \tag{1.13}$$

c_i refers to the coefficient of the atomic orbital Φ_i. The higher the number of the atomic orbitals (N) results in better estimation. Equation 1.14 results from substituting Equation 1.13 into 1.12:

$$E_G = \frac{\int \sum_{i=1}^{N} c_i \Phi_i \hat{H} \sum_{j=1}^{N} c_j \Phi_j dr}{\int \sum_{i=1}^{N} c_i \Phi_i \sum_{j=1}^{N} c_j \Phi_j dr}$$

$$= \frac{\sum_{i=1,j=1}^{N} c_i c_j \int \Phi_i \hat{H} \Phi_j dr}{\sum_{i=1,j=1}^{N} c_i c_j \int \Phi_i \Phi_j dr}$$

$$= \frac{\sum_{i=1,j=1}^{N} c_i c_j w_{ij}}{\sum_{i=1,j=1}^{N} c_i \chi_{ij}} \tag{1.14}$$

χ represents the overlap integral and ω refers to the resonance integral. ω_{ij} is physically explained as the ionization potential of the orbitals (Cramer, 2002). Decreasing E_G in Equation 1.14 helps to acquire the optimum wave function to describe the molecular system (Cramer, 2002). To get the function's slowest value, the function derivative should be zero for all the free variables c_i. This partial

differentiation for N variables to Equation 1.14 results to N equations that should be satisfied, explicitly. Equation 1.15 is shown below:

$$\sum_{i=1}^{N} c_i(w_{ji} - E_G \chi_{ji}) = 0 \quad \forall_j \tag{1.15}$$

A non-trivial solution can be obtained for the N-equations by making the determinant composed of the coefficients of each variable equal to zero. This determinant is called the Secular determinant.

1.3.7.2.3 Density-Functional Theory

Hartree-Fock is one of the most common first principles methods which assumes independent electrons to overcome the computational complexity (Slater, 1951). This method uses a new term for the electron-electron interaction. Moreover, it uses a recursive self-consistence field to solve secular determinate.

Density-Functional Theory (DFT) is the most commonly used first principle approach. It allows an easier computational process by utilizing the electron density as the system observable (Becke, 1988; Brandbyge, Mozos, Ordejón, Taylor, & Stokbro, 2002; Hohenberg & Kohn, 1964; Taylor, Guo, & Wang, 2001). The external potential is computed by the electron density which enables the Hamiltonian evaluation (Cramer, 2002). The energy is evaluated by solving Schrödinger equation.

DFT begins the computation by presuming an imaginary non-interacting system of electrons with a similar electron density of the real device. Then, the secular matrix is determined by the electron density by applying Kohn-Sham self-consistent field. Moreover, the electron density should by calculated at the same time by solving

the secular equations from the derived orbitals (Cramer, 2002; Kohn & Sham, 1965). Since standard DFT computations do not deal properly with the exchange interaction. Exchange correlation functions such as density gradient corrections and local density approximation are used to overcome this limitation (Zupan & Causà, 2004).

A semi first-principles method that can be used is DFT with Tight-Binding approximation (DFTB) (Porezag, Frauenheim, Köhler, Seifert, & Kaschner, 1995). DFTB ignores the molecule core electrons which reduces the secular determinant size. The integral calculation is deployed explicitly. The computational cost is reduced highly due to the size reduction of secular determinant (Koskinen & Mäkinen, 2009; Pecchia & Di Carlo, 2004). DFTB method resulted in reliable and successful results for various molecules despite the approximation. Thus, many research groups conducted outstanding publications by using DFTB (Andrews, Solomon, Duyne, & Ratner, 2008; Pecchia, Penazzi, Salvucci, & Di Carlo, 2008; Penazzi et al., 2013; Solomon et al., 2006). DFTB is utilized in combination with NEGF formalism for simulation studies in this research work (Wasfi & Awwad, 2019a; Wasfi, Awwad, & Ayesh, 2020).

1.3.7.2.4 Standard and Extended Hückel Theories

Solving systems with large molecules by first principles approach requires high computational resources. Investigating such systems with semi-empirical computation received wide acceptance. Semi-empirical approaches employ parametric models in computation for approximation. These parameters are chosen to achieve best fitting to experimental data (Dewar, Hashmall, & Venier, 1968; Stewart, 1990; Thiel & Voityuk, 1996; Zerner, 2007). Various factors supported the semi-empirical methods development such as the experimental data availability and the need to facilitate the

computation for large molecules (Cramer, 2002; Zerner, 2007).

Standard Hückel uses the empirical and approximate parameters. The secular determinant can be solved easily by these parameters for the unsaturated hydrocarbons and planner aromatic. The method assumes that each carbon atom basis set is formed from the $2p_Z$ orbital. Therefore, the overlap integrals for the equal atomic orbital (χ_{ii}) is one (Kronecker delta function) and zero between the different atomic orbitals (χ_{ij}). For the resonance integrals (ω_{ij}), constant empirical values are used. Equation 1.16 is displayed below:

$$\omega_{ij} = \begin{cases} \alpha & when\ i = j, \\ \beta & when\ atom\ \text{"i" is bonded to atom "j"}. \\ 0 & otherwise \end{cases} \tag{1.16}$$

α refers to a constant value equal to negative the ionization energy of methyl radical and β is a constant value equal to negative energy relevant to pi-bond stability. Therefore, the energies of the molecule can be easily calculated.

Roald Hoffmann developed Extended Hückel Theory (EHT) in 1963 which is one of the most popular semi-empirical approaches (Cerdá & Soria, 2000; Hoffmann, 1963; Magoga & Joachim, 1997). EHT ignores the core electrons and only considers the valence electrons. Thus, the secular determinate size is decreased to the valence orbitals number. The system electronic structure is displayed in Linear Combination of Atomic Orbitals (LCAO) basis set. Slater-Type Orbital (STO) is used to describe the valence orbital as driven by Equation 1.17:

$$STO = \Phi_{nlm}(\boldsymbol{r}, \varsigma) = \frac{(2\varsigma)^{n+\frac{1}{2}}}{\sqrt{2(n)!}} r^{n-1} e^{-\varsigma} \Upsilon_l^m(\theta, \varphi), \tag{1.17}$$

$\boldsymbol{r}, \theta, \varphi$ spherical coordinates are used. l, n, and m refers to angular momentum, principal, and magnetic quantum numbers, respectively. $\Upsilon_l^m(\theta, \varphi)$ is the real-valued spherical harmonics. ς is named the orbital exponent which is calculated based on a set of predefined rules (Slater, 1930).

The Hamiltonian matrix diagonal elements are equal to the corresponding orbital ionization potential. The Hamiltonian matrix off-diagonal elements are generated by Helmholtz and Wolfsberg approximation which relates the off-diagonal element (H_{ij}) to orbitals i and j average ionization potential. Equation 1.18 is displayed below:

$$\omega_{ij} = K\chi_{ij} \frac{\omega_{ij} + \omega_{ij}}{2} \tag{1.18}$$

K refers to Wolfsberg-Helmholtz constant.

The diagonal and non-diagonal matrix elements are evaluated first. Then wave-functions and energies of valence orbitals are calculated by resolving a standard eigenvalue equation. Despite that the electron-electron interaction is not included in EHT calculation, it is not neglected. It is incorporated in an average way while deriving the Hamiltonian matrix using the data from experiment (Cramer, 2002).

1.3.7.2.5 Non-Equilibrium Green's Functions

Nano devices are treated as an infinite system, therefore the system is split into

electrode and scattering areas. Periodic boundary conditions are imposed to the electrodes regions since they are assumed to be semi-infinite which allows restoring the bulk behavior of the electrodes. The scattering area maintains the major part of the device and a part of the contact to ensure consistent charge density with the electrodes (Pecchia & Di Carlo, 2004). The following assumes two-terminal devices for simplicity; however, the method works for multi-terminal devices.

The previously illustrated first principle and semi-empirical methodologies enable the computation of the electronic structure of a system and provide the Hamiltonian matrix which is needed for every system analysis. However, the charges induced due to the bias conditions have to be included while computing the Hamiltonian. NEGF is usually coupled with these methodologies to account for non-equilibrium conditions (Elstner et al., 1998; Pecchia & Di Carlo, 2004; Stokbro et al., 2010). NEGF computes the bias based calculation of charge density and current.

The system subdivision is translated to Hamiltonian subdivision and wave-function of Schrödinger equation as displayed in Equation 1.19:

$$\begin{pmatrix} \hat{H}_1 & \tau_1 & 0 \\ \tau_1^\dagger & \hat{H}_S & \tau_2^\dagger \\ 0 & \tau_2 & \hat{H}_2 \end{pmatrix} \begin{pmatrix} \Psi_1 \\ \Psi_S \\ \Psi_2 \end{pmatrix} = E \begin{pmatrix} \Psi_1 \\ \Psi_S \\ \Psi_2 \end{pmatrix} \tag{1.19}$$

$\hat{H}_1, \hat{H}_2, and \ \hat{H}_S$ are the Hamiltonian of the right electrode, left electrode, and scattering region, respectively; $\tau_1 \ and \ \tau_2$ refers to the interaction between the electrodes and the scattering region (Paulsson, 2002).

With infinite systems, two solutions can be driven which correspond to

incoming (advanced) and outgoing (retarded) waves. A and R superscripts refer to the solutions of advanced and retarded, respectively. The system Green's function $G(E)$ is defined in Equation 1.20 below:

$$\left(E - \hat{H}\right)G(E) = I \tag{1.20}$$

$G(E)$ is divided into sub-matrices as displayed in Equation 1.21 because of the various scattering and electrodes regions;

$$G(E) = \begin{pmatrix} G_1 & G_{1S} & G_{12} \\ G_{S1} & G_S & G_{S2} \\ G_{21} & G_{2S} & G_2 \end{pmatrix} \tag{1.21}$$

η refers to a constant perturbation which is induced to Schrödinger Equation 1.22:

$$H\Psi = E\Psi + \eta \tag{1.22}$$

To provide the system response to such perturbation, the Green's function in Equation 1.23 is used:

$$(E - H)\Psi = -\eta \implies \Psi = -G(E)\eta \tag{1.23}$$

Many devices behavior can be evaluated by the Green's function such as the isolated electrodes wave function. For example, the first row in Equation 1.18 can be used to generate the first electrode behavior as in Equation 1.24:

$$\hat{H}_1\Psi_1 + \tau_1\Psi_S = E\Psi_1$$

$$\left(E - \hat{H}_1\right)\Psi_1 = \tau_1\Psi_S$$

$$\Psi_1 = g_1\tau_1\Psi_S \qquad (1.24)$$

g_1 refers to first isolated electrode Green's function $\big((E - H_1)g_1 = I\big)$. The isolated electrodes Green's functions can be evaluated in a simple mathematical way to exploit the periodicity property of the electrode material (Zahid, Paulsson, & Datta, 2003). The generation of self-energy is conducted by utilizing the isolated Green's functions as shown in Equation 1.25 and Equation 1.26 below:

$$\sum_1 = \tau_1^\dagger g_1\tau_1 \qquad (1.25)$$

$$\sum_2 = \tau_2^\dagger g_2\tau_2 \qquad (1.26)$$

The self-energies are used to measure the contacts impact on the device (Zahid et al., 2003) which are used in evaluating the device analytical behavior. Using Equations 1.18 to 1.20, substitutions and calculation the sub-matrix of Green's function scattering region can be evaluated to produce Equation 1.27:

$$G_S(E) = (E - \hat{H}_S - \sum_1 - \sum_2)^{-1} \qquad (1.27)$$

Moreover, $G(E)$ is used to calculate the device density of state by evaluating the spectral function $A(E)$ using Equation 1.28 and Equation 1.29,

$$A(E) = i\Big(G(E) - G^\dagger(E)\Big), \qquad (1.28)$$

$$D(E) = Tr(A(E))/2\pi \qquad (1.29)$$

Moreover, Green's function enables the computation of the device density matrix $[\rho]$ as displayed in Equation 1.30:

$$\rho = \frac{1}{2\pi} \int_{-\infty}^{\infty} [f(E, \mu_1) G_S \Gamma_1 G_S^\dagger + f(E, \mu_2) G_S \Gamma_2 G_S^\dagger] dE \qquad (1.30)$$

This density matrix will be used back in the semi-empirical or first principle methods to regenerate the Hamiltonian matrix self-consistently where the procedure will be repeated till it reaches the required accuracy while taking into account the induced charges because of the non-equilibrium condition.

Chapter 2: Methods

This chapter presents the research design and implementation of the developed sensors based on software simulation and experimental fabrication works. It also introduces the required equipment, materials and the employed methods.

2.1 Simulation

The simulation work was conducted using ATK-VNL. This software was utilized through United Arab Emirates University High Performance Computing (HPC).

2.1.1 Simulation Research Design
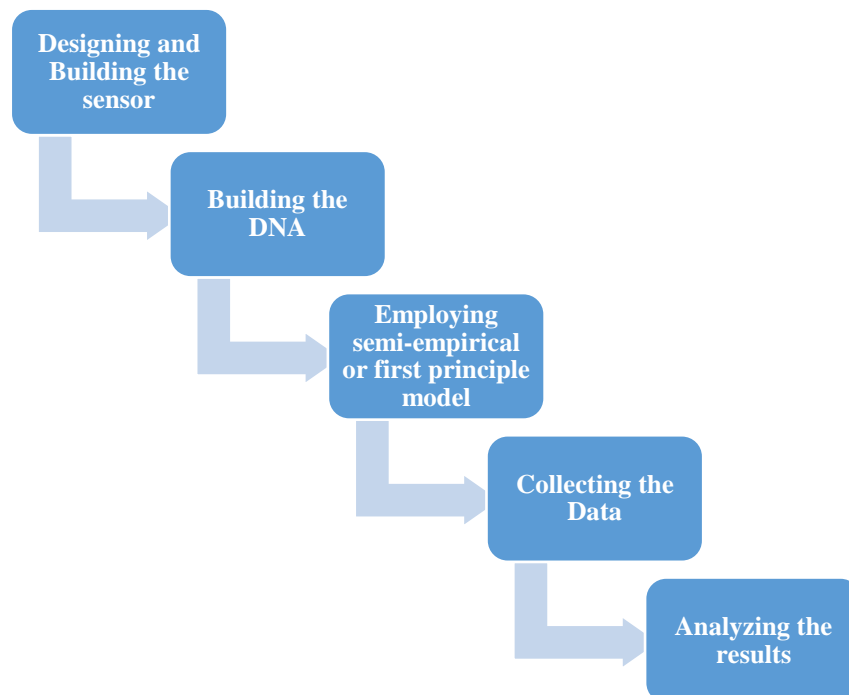
Figure 6: Simulation Research Design.

The simulation research work was conducted as depicted in Figure 6. It started by designing and building the sensor using ATK-VNL package. Then, the DNA strands and DNA nucleobases were built using the ATK-VNL package. After that, the sensor was tested and the data was collected to be analyzed. These steps are explained in details in Section 2.1.2 and Section 2.1.3.

2.1.2 Simulation of FET Sensors Based on Graphite Oxide Decorated with Trimetallic Nanoclusters

This part aims to demonstrate the detection of various concentrations of DNA by first-principles computations, and to confirm the experimental results. ATK-VNL was used to design and simulate the proposed sensor. Device current was generated and measured with the ATK simulator where the simulator has different methodologies to generate the electronic transport properties of the developed sensor. In order to speed up the simulation process, High Performance Computing (HPC) environment has been used with 7 nodes each with 36 processors. In total 252 processors were used to conduct the simulation.

The sensor configuration was done by python scripting and QuantumATK combination which are flexible, enabling the atomistic modeling in various ways. QuantumATK general workflow starts by creating the atomistic structure using the builder, then setting up the python scripts and the calculations, after that running the scripts on local machines or remote clusters, and finally visualizing and analyzing the results. The builder is used to design any required nanoscale atomistic structure where the stash includes the built configurations of the project and a list of plugins and tools to modify the structures. After the nanoscale device configuration has been built, the script generator is used to set up the required calculations. All QuantumATK data are

saved in .hdf5 file format where HDF5 is a data model for managing and storing data. It supports various data types and used for complex and high volume data. HDF5 enables viewing, managing, analyzing, and modifying the data in the file. The nanoscale device configuration consists of right electrode, central region, and left electrode. Current flows among the pair of electrodes through the scattering region. The central region ends are called electrode extensions which are accurate replicas of the electrodes.

Figure 7 displays the schematic of the simulated nanoscale electronic device. Figure 7 (a) displays a two-dimensional schematic view of the designed GO-FET sensor and Figure 7 (b) illustrates the cross-sectional view of the investigated sensor. The GO-FET sensor was made of three regions source, drain and an active channel with a gate terminal underneath. The source and drain were made of gold and the channel was made of GO (358 atoms). The gate was made of two layers: a 2.6 Å dielectric layer of SiO_2 with relative dielectric K=4 (given by quantumatk software website) (Pandey, 2018) and a metallic layer. The GO channel has an approximate width of 17 Å and length of 42 Å. These dimensions were selected due to the number of atoms, the size of the DNA sample and the size of nanoclusters. A pair of 17 Å gold electrodes was connected at the edges of the GO sheet. The software employed different approaches to generate the transport properties of quantum systems. Non-Equilibrium Green's Function formalism (NEGF) and Density Functional Theory (DFT) were used for the designed senor simulation in ATK-VNL.

(a)
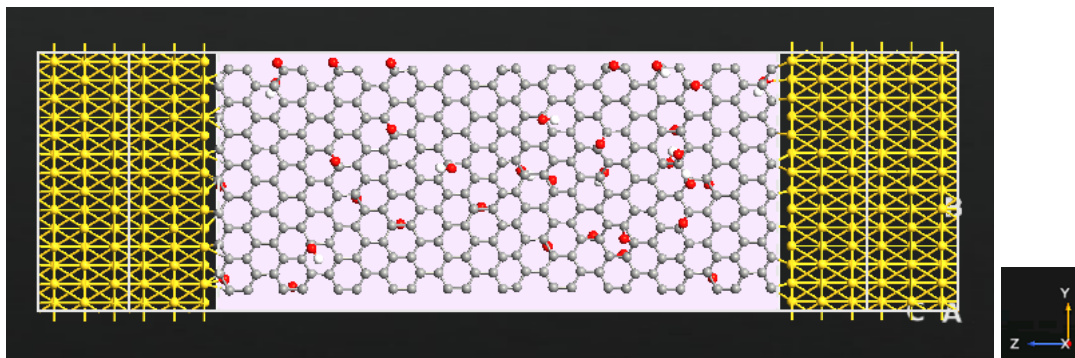
(b)
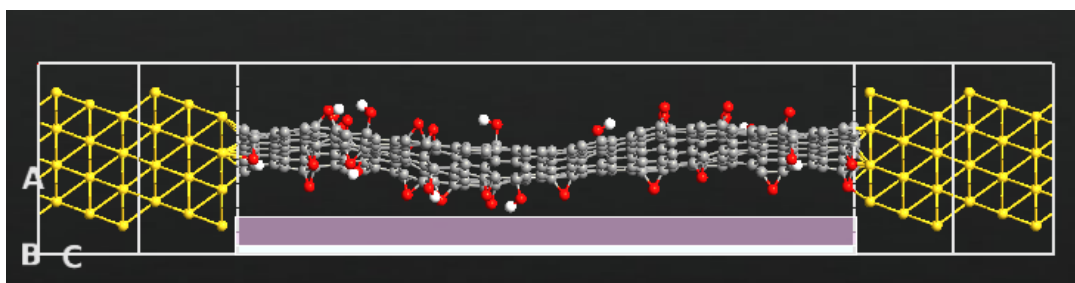
Figure 7: GO-FET sensor built by ATK. (a) Schematic diagram of the GO-FET sensor from ATK. (b) Cross-sectional view of the GO-FET sensor. The designed sensor is made of pair of gold electrodes (source and drain), a GO channel and a gate below the channel. Color code: carbon-gray, hydrogen-white, gold-yellow, and oxygen-red.

Decorating the GO channel with metal nanocluster affects the sensor behavior because the metallic nanoclusters change the electronic structure of the sensor. The sensor was decorated with monometallic nanoclusters of gold, silver, and platinum and trimetallic nanoclusters of gold, silver, and platinum depicted in Figure 8 (a). Monometallic and trimetallic nanocluster of gold, silver, and platinum were used in this work because of their high affinity to DNA strands. The GO-FET was decorated with 1 nm nanocluster as shown in Figure 8 (b). The effect of decorating the sensor with nanocluster on the sensor current and sensitivity was investigated. It was noticed that GO-FET sensor performance and sensitivity was enhanced after adding the

monometallic and trimetallic nanocluster. However, the sensor decorated with trimetallic nanoclusters showed the best sensitivity (variation in current).

(a)
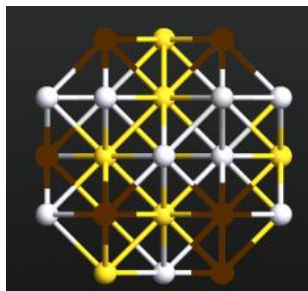
(b)
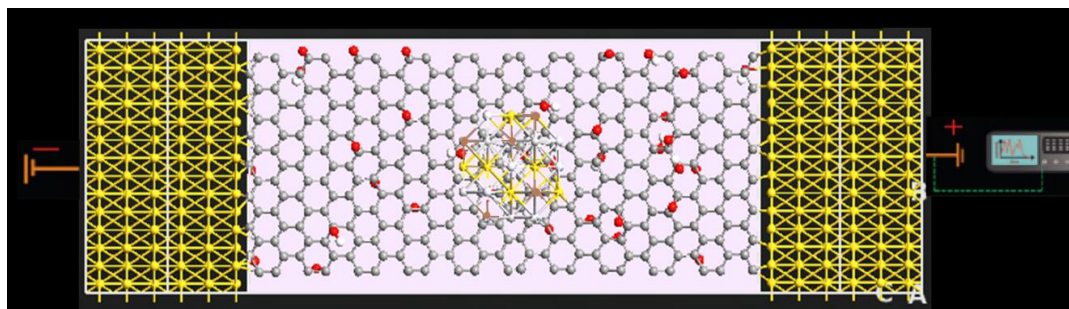
Figure 8: FET decorated with composite nanoclusters. (a) Composite nanocluster of silver, gold, and platinum of size 1 nm. (b) GO-FET decorated with 1 nm composite nanocluster of silver, gold, and platinum. The gate potential (0V) and bias voltage between the right and left electrodes (-0.1 and +0.1 V) are fixed. Color code: carbon-gray, hydrogen-white, gold-yellow, oxygen-red, silver-light gray, and platinum-brown.

The GO-FET sensor electronic transport properties were generated by the ATK-VNL package. Poisson equation with marginal conditions was utilized where Dirichlet boundary condition was selected for the electrostatic potential in the Z-direction and Neumann boundary condition was chosen for the X and Y directions. These are the appropriate conditions for a device with a metallic gate. For exchange correlation of quantum-ATK–DFT calculator, Perdew–Zunger (PZ) parameterization of the Local Density Approximation (LDA) and Troullier–Martins norm-conserving

pseudopotentials were selected. The 50 k-points were chosen in the Z direction transmission. Throughout the calculations the density mesh cut-off was 75 Hartree. The gate potential was set to 0 V, and the bias voltage between the source and drain electrodes was set to -0.1 V and 0.1 V. The transverse current was measured to detect various concentrations of DNA. The computational method and mathematical formalism used by the software were explained in previous work (Wasfi et al., 2020). All the required simulations have been generated through High Performance Computing environment (HPC).

2.1.3 Graphene-Based Sensors with a Nanopore or a Nanogap

DNA sequencing via graphene nanopore and nanogap methodology were applied in this work. This section presents the simulation of four sensors to identify the DNA bases. DNA backbones of sugar and phosphate groups were not considered in the simulation. The backbone contribution was ignored, as the background noise coming from the backbone may be determined and subtracted from the signal of individual nucleobases (Ahmed et al., 2014).

The device used in the following Sections 2.1.3.1, 2.1.3.2, 2.1.3.3, and 2.1.3.4 was built by utilizing nanoribbon plugin tool in the ATK software builder. The Armchair Graphene Nanoribbon (AGNR) width created by nanoribbon plugin tool is 13 atoms. Then, the AGNR was extended 14 times using repetition pattern along the C direction as shown in Figure 9. The plugin tool was also used to build the Zigzag Graphene Nanoribbon (ZGNR) where it consists of 16 atoms and the ZGNR structure was repeated 4 times along the C-axis as shown in Figure 10 and a copy of this

structure was created. The two ZGNR structures were connected to the AGNR region
to form the sensor.
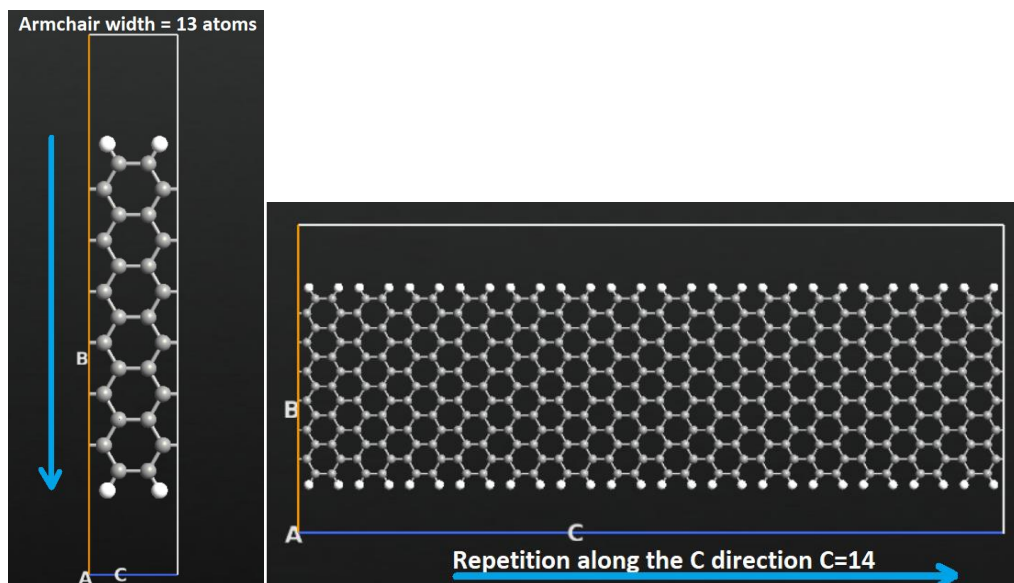
Figure 9: AGNR for the central region of the sensor.
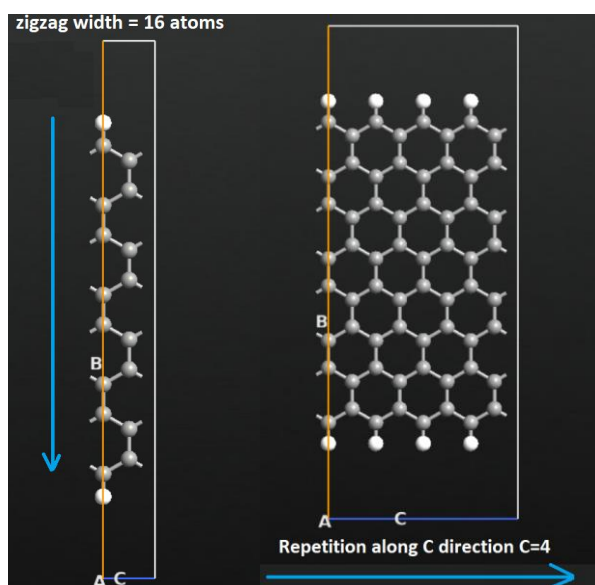
Figure 10: ZGNR for the sensor electrode.

The AGNR placed in the builder stash was rotated 30 degree around the x axis by using coordinate tools as displayed in Figure 11. Then the fit cell in the bulk tools was used to fix the cell along the B axis.
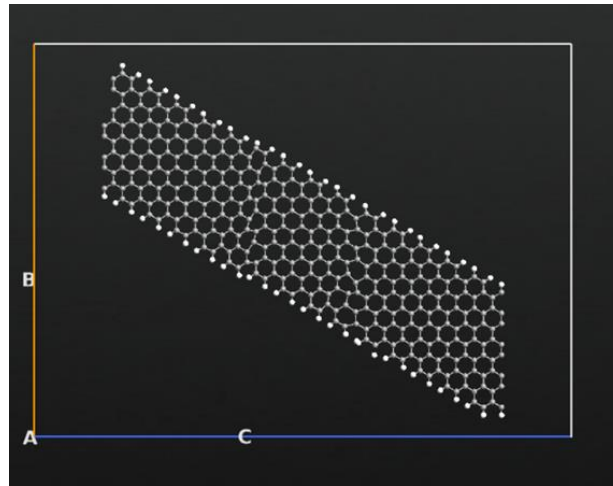
Figure 11: AGNR rotated 30 degree around the x-axis.

The merge option in bulk tools was used to merge the ZGNR with the AGNR as displayed in Figure 12 to form the z-shaped structure and convert it to a device as displayed in Figure 13.
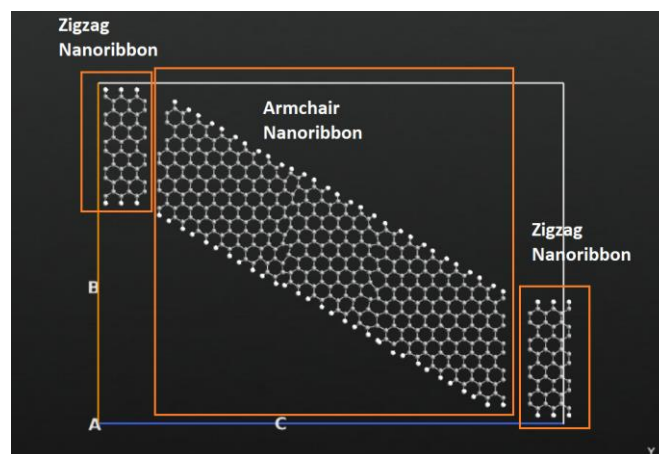
Figure 12: Merging the ZGNR electrodes with the central AGNR.
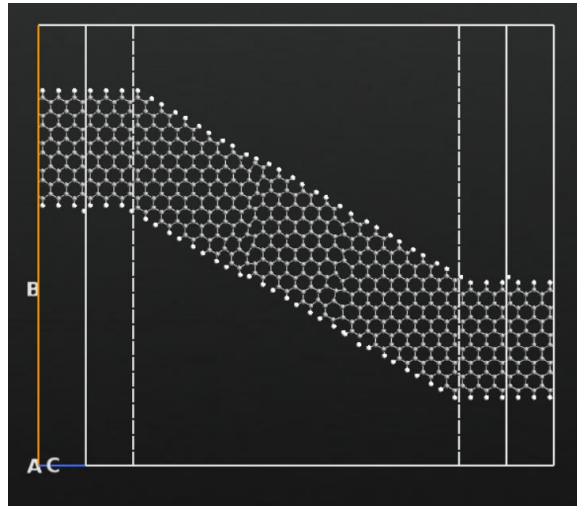
Figure 13: Z-shaped graphene nanoribbon device.

2.1.3.1 Z-shaped Graphene Nanoribbon with a Nanopore

This section presents the design of the first sensor through ATK-VNL. A novel two-terminal z-shaped graphene nanoribbon sensor was developed and studied to detect the DNA nucleobases. The z-shaped sensor name refers to the graphene nanoribbon structure. The z-shaped graphene nanoribbon sensor consists of two metallic Zigzag Graphene Nanoribbon (ZGNR), a semiconducting channel made of Armchair Graphene Nanoribbon (AGNR), and a nanopore in the middle of the channel through which DNA nucleobases are translocated. First-principle modeling and Non-Equilibrium Green's Function along with Density Functional Theory (NEGF + DFT), were utilized to investigate the developed device. Various electronic characteristics were investigated, including transmission spectrum, conductance, and electrical current of DNA nucleobases inside the graphene sensors' nanopore. In particular, these properties were studied with variation of nucleobase orientation. The developed sensor resulted in unique signatures for the individual four DNA nucleobases placed within the nanopore.

2.1.3.1.1 Sensor Configuration

Figure 14 shows the nanoscale device setup introduced in this work. The z-shaped metal-semiconductor-metal junction device consists of the following regions: the electrodes (right and left), and the main central region. The left and right electrodes consist of metallic zigzag graphene nanoribbons while the middle was made of armchair graphene nanoribbon with a width of 13 carbon chains which makes the AGNR semiconducting. A nanopore of size 10.1 Å was created in the central region. The nanopore carbon atoms of the edge and graphene nanoribbons were passivated with hydrogen. This work evaluates the performance of the graphene nanopore that is utilized for DNA bases detection, by employing first-principles calculations using Quantumwise (ATK-VNL) package.
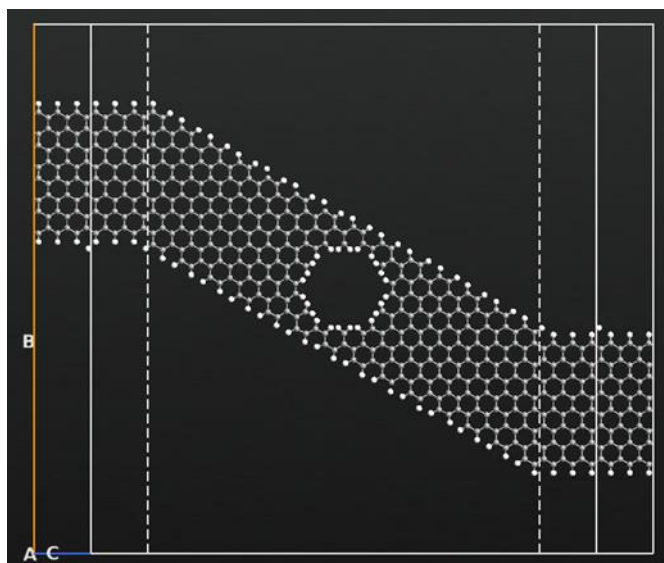
Figure 14: Schematic view of z-shaped graphene nanoribbon DNA sensor.

2.1.3.1.2 Z-shaped Graphene Nanoribbon Sensor Structure

Figure 15 shows the z-shaped graphene nanoribbon sensor hosting a nanopore of 10.1 Å diameter where DNA bases translocate. The current flow is perpendicular to the DNA bases. The width of the armchair graphene nanoribbon and the nanopore was fixed. Armchair width is 16.61 Å. Finite bias voltage was applied between left and right electrode which is fixed as +0.25 and -0.25 V.

Due to the different electronic and chemical structure of the four nucleobases, each one of them has a unique signature. The main objective of this sensor is to find the relative current for each nucleobase where a unique electronic signature is found for each base to create a DNA electronic map.
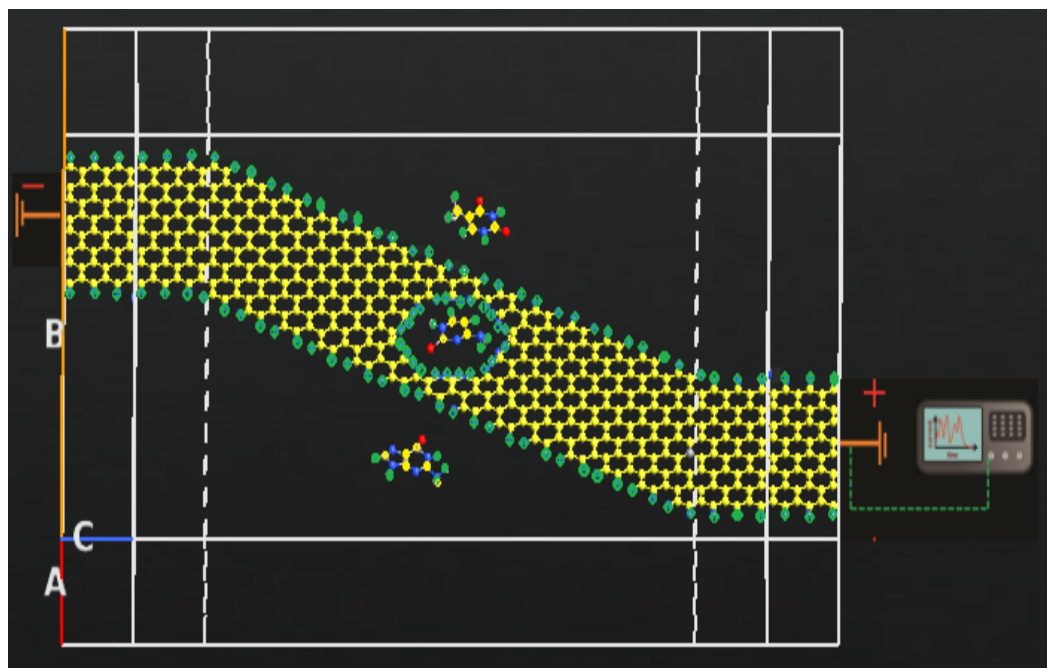
Figure 15: Schematic representation of z-shaped graphene nanoribbon with nanopore. The isolated DNA bases pass through the nanopores and transverse electronic current flow through the membrane. The edge carbon atoms of the nanopore and of the graphene nanoribbon are passivated by hydrogen. (Carbon-yellow, Hydrogen-green, Nitrogen-blue, Oxygen-red).

2.1.3.1.3 Computational Methods

Prior to ATK-VNL transport calculations, the density functional theory was utilized to optimize the device and nucleobases and to relax all atoms till the individual atomic force is below 0.05 eV/Å since molecules are most stable when their energy is low. All optimizations were completed by the density functional theory. The Perdew-Burke-Ernzerhof parametrization for the Generalized Gradient Approximation (GGA) was utilized for the exchange and correlation function (Perdew, Burke, & Ernzerhof, 1996). The employed density mesh cut-value of energies was 400 eV. A 1x1x1 k-point mesh was utilized for the Brillouin zone integration within Monkhorst-Pack scheme. Density functional theory was used to describe the developed device, where an extension of this method is the formalism of NEGF which is used to describe the quantum transport phenomena. The NEGF formalism sets the concept to study the electronic transport at quantum level which allows calculating the desired quantities such as conductance and current for the DNA sensor.

Density functional theory along with local density approximation (LDA) limits and Perdew-Zunger exchange correlation function (Perdew & Zunger, 1981) impeded in the ATK-VNL simulation package were employed. A mesh cut-off of 65 Hartree was fixed to display the charge density. A grid of 2x2x100 k-points was utilized to perform the sampling of the Brillouin Zone integration. The transmission spectrum as a function of bias, conductance, and current were determined by utilizing the NEGF as integrated in the ATK-VNL.

The zero bias transmission spectrum between the source and drain was calculated using Equation 2.1 (Chang, Liu, & Nikolic, 2014; Saha, Drndić, & Nikolić, 2012):

$$T(E) = Tr\{\Gamma_D(E)G(E)\Gamma_S(E)G^{\dagger}(E)\} \tag{2.1}$$

where, E is the energy, Tr is the trace, $\Gamma_{D,S}(E) = i[\Sigma_{L,R}(E) - \Sigma^{\dagger}_{S,D}(E)]$ describes the broadening level because of the coupling to the electrodes, and $\Sigma_{L,R}(E), \Sigma^{\dagger}_{S,D}(E)$ are the self-energies presented by the electrodes.

The linear response conductance at a certain Temperature (T) is determined from the transmission function by the standard Landauer formula for devices with two terminals as displayed in Equation 2.2 (Chang et al., 2014; Saha et al., 2012):

$$G(E_F) = \frac{2e^2}{h} \int_{-\infty}^{\infty} dE \, T \left(-\frac{\partial f}{\partial E}\right) \tag{2.2}$$

where, $G_0 = \frac{2e^2}{h}$ is the conductance quantum which is $\approx 7.7480917310 \times 10^{-5}$ S, $f(E) = \{1 + \exp[(E - \mu)/k_B T]\}^{-1}$ is defined as the Fermi function of some macroscopic reservoirs where semi-infinite ideal contact leads terminate, $\mu = E_F$ refers to the electrode chemical potential, and k_B is Boltzmann's constant.

The electron transmission spectrum as a function of bias is evaluated utilizing NEGF method, as integrated in ATK-VNL, using Equation 2.3 (Chang et al., 2014):

$$T(E, V_b) = Tr\{\Gamma_D(E, V_D)G(E)\Gamma_S(E, V_S)G^{\dagger}(E)\} \tag{2.3}$$

where, G and $G^{\dagger}$ are associated with advanced Green's function of the main scattering region, and $V_b = V_s - V_d$ where V_b is the bias voltage between source (V_s) and drain (V_d). S, D, L, and R refer to the source, drain, left, and right, respectively. The

transmission spectrum function T(E, V) illustrates the probability for quantum mechanical transmission of electrons. The right and left electrodes' semi-infinite effect is considered by creating the self-energies $\sum_{L,R}(E)$ and $\sum_{S,D}^{t}(E)$ in the effective Hamiltonian.

The integration of $T(E, V)$ over the energy window determined using the difference of the Fermi functions $f_{S,D}(E) = \{1 + \exp[(E - E_F - eV_{S,D})/k_B T]\}^{-1}$ gives the total current displayed in Equation 2.4 :

$$I = \frac{2e}{h} \int_{-\infty}^{\infty} dE\ T(E,V)[f_S(E) - f_D(E)] \tag{2.4}$$

2.1.3.2 Z-shaped Graphene Nanoribbon with a Nanogap

This section presents the second sensor which is a z-shaped graphene nanoribbon with a nanogap. The main difference between this sensor and the one demonstrated in Section 2.1.3.1 is placing a nanogap in the middle of the graphene nanoribbon instead of the nanopore. Moreover, the edge carbon atoms of the nanogap were passivated by either hydrogen or nitrogen. The z-shaped graphene nanoribbon sensor performance was also studied by Non-Equilibrium Green's Function combined with Density Functional Theory (NEGF+DFT). The transverse current and the transmission spectrum of the DNA bases within the nanogap were investigated with variation in the base orientation. Placing a DNA base into the nanogap impacts the charge density of the sensor leading to unique signature for each of the four DNA bases (Wasfi & Awwad, 2019a)© 2019 IEEE.

2.1.3.2.1 Two-Terminal Z-shaped graphene nanoribbon Setup

Figure 16 shows the z-shaped graphene nanoribbon sensor setup. The two-terminal sensor consists of: metallic right and left electrodes, the semi-conducting central region, and a nanogap in the middle of the central region. The edge carbon atoms of the sensor were passivated with hydrogen, while the 1.01 nm nanogap edge carbon atoms were passivated with either nitrogen as shown in Figure 17 (a) or hydrogen as shown in Figure 17 (b). The AGNR width is 1.6 nm and the electrodes length is 1.617 nm. The applied bias voltage was 2 V which is fixed between the left and right electrodes as 1 V and –1 V (Wasfi & Awwad, 2019a)© 2019 IEEE.
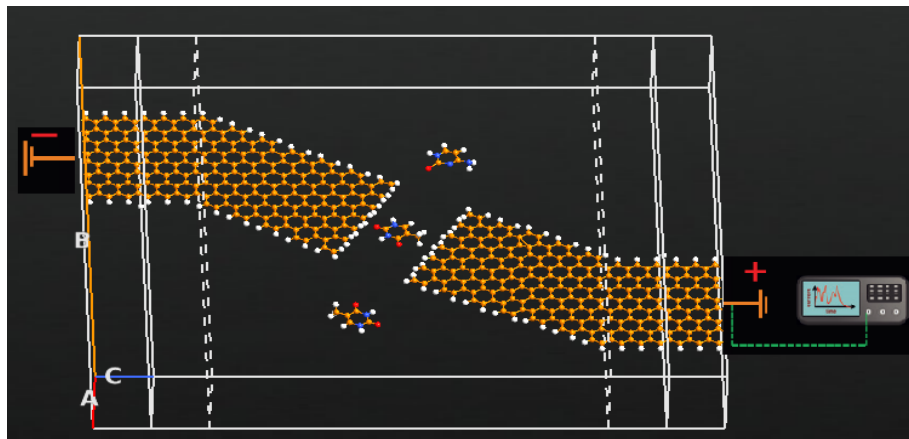
Figure 16: Schematic representation of the z-shaped graphene nanoribbon sensor configuration. The individual DNA bases go through the nanogap passivated with either hydrogen or nitrogen. (Carbon-orange, Nitrogen-blue, Hydrogen-white, Oxygen-red) (Wasfi & Awwad, 2019a)© 2019 IEEE.
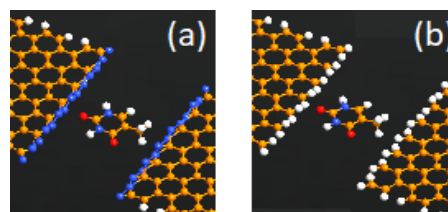
Figure 17: Graphene nanogap. (a) N-nanogap (edge carbon atoms are passivated with nitrogen-blue). (b) H-nanogap (edge carbon atoms are passivated with hydrogen-white). (Wasfi & Awwad, 2019a)© 2019 IEEE.

2.1.3.2.2 Computational Methodology

Before conducting electronic transport simulations for each base within the nanogap of the two-terminal z-shaped graphene nanoribbon sensor, geometry optimization is required. Structural optimization was conducted using first principle modeling based on density functional theory in ATK-DFT package (Brandbyge et al., 2002), as explained in Section 2.1.3.1.3. Density functional theory was utilized within the Local Density Approximation (LDA) limits with Perdew-Zunger functional exchange correlation (Kohn & Sham, 1965; Perdew & Zunger, 1981). The Brillouin zone integration sampling was conducted with a grid of $1 \times 1 \times 50$ k-points and the grid mesh cut off energy of 75 Hartree was used. The mathematical formalism used by the software has been explained in Section 2.1.3.1.3 (Wasfi & Awwad, 2019a)© 2019 IEEE.

2.1.3.3 Z-shaped graphene nanoribbon field effect transistor decorated with nanoparticles

The sensor illustrated in this section aims to improve DNA bases detection accuracy and the overall current signal. Herein, a novel z-shaped graphene nanoribbon field effect transistor with a nanopore for the aim of DNA detection is studied, where a gate terminal was added below the center of the z-shaped graphene nanoribbon illustrated in Section 2.1.3.1. First-principle transport calculations were used to identify the DNA bases and electronic signature. An efficient Density Functional Theory approach combined with Non-Equilibrium Green's Function formalism (DFT +NEGF) were utilized to detect the transmission spectrum and current for DNA nucleobases: Adenine, Thymine, Guanine, and Cytosine. Using transmission current, a distinctive electronic signature was generated for each DNA base to detect them. Various orientations and lateral position for each DNA base are considered. Moreover,

the effect of decorating the developed DNA sensor with gold and silver nanoparticles on the sensor's electrical current and transmission spectra is studied and analyzed.

2.1.3.3.1 Setup of the z-shaped graphene nanoribbon field effect transistor with a nanopore
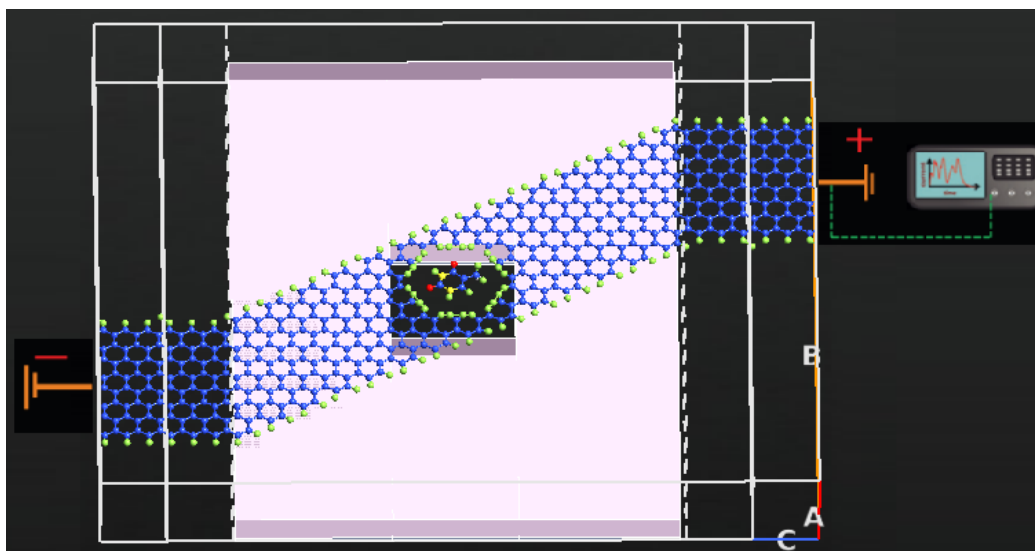
Figure 18: Schematic diagram of the z-shaped graphene nanoribbon field effect transistor with a pore. DNA nucleobases pass through the nanopore and transverse electronic current pass across the graphene membrane. The gate potential (2V) and bias voltage between the right and left electrodes (+0.25 and −0.25 eV) are fixed. The nanoribbon and nanopore edges are passivated by hydrogen. Color-code: Carbon-blue, Nitrogen-yellow, Oxygen-red, and Hydrogen-green (Wasfi et al., 2020) © 2020 IOP.

The structure of the nano-scale sensor was developed and investigated using Quantum-ATK simulator, as shown in Figure 18. The sensor field effect transistor was made of graphene channel. Graphene nanoribbon was made of source and drain and a semiconducting channel. The sensor is a three-terminal device with source, drain, and gate. A nanopore of size 10.1 Å was placed in the middle of the z-shaped nanoribbon. The field effect transistor was made of two metallic zigzag graphene nanoribbon electrodes connected through a semiconducting channel of armchair graphene nanoribbon. Each of the metallic zigzag nanoribbons has sixteen carbon chains in

width, and the semiconducting armchair has thirteen chains in width (length of the metallic ZGNR electrodes is 15 Å while the width of the armchair graphene nanoribbon is 16.61 Å). Two layers: dielectric (with a dielectric constant 4) and a metallic were added under the central armchair graphene nanoribbon. No doping for the source, drain, and gate is performed. The edge carbon atoms of the nanoribbon and nanopore saturated their dangling bonds by bonding with their neighbor atoms. The edge carbon atoms were passivated with hydrogen. This type of transistor is called a z-shaped graphene nanoribbon transistor (Gupta et al., 2015; Wasfi et al., 2020) © 2020 IOP.

2.1.3.3.2 Configuration of the sensor decorated with nanoparticles

Decorating graphene with metal nanoparticles influences graphene charge transport behavior since the nanoparticles change graphene local electronic structure. Metal nanoparticles such as gold (Figure 19 (a)) and silver (Figure 19 (b)) are selected in this work since they have high affinity to DNA nucleobases. The z-shaped graphene nanoribbon sensor was decorated with 10 Å gold (Figure 20 (a)) and silver (Figure 20 (b)) nanoparticles. The structure of nanoparticles were optimized using Quantum-ATK. The nanoparticles' influence on local electronic structure was studied using electronic properties such as transmission spectrum and current. Here, the electronic effect of attaching silver and gold nanoparticles to the z-shaped graphene nanoribbon sensor on the DNA base detection was investigated (Wasfi et al., 2020).
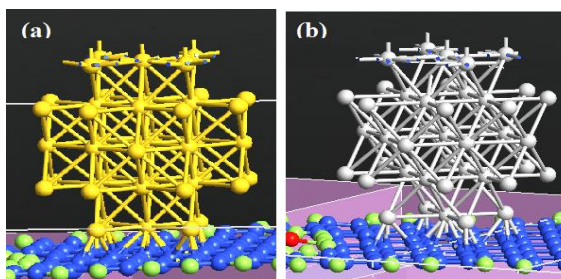
Figure 19: Optimized nanoparticles. (a) Optimized 10 Å gold (111) nanoparticle. (b) Optimized 10 Å silver (111) nanoparticle. (Wasfi et al., 2020) © 2020 IOP.
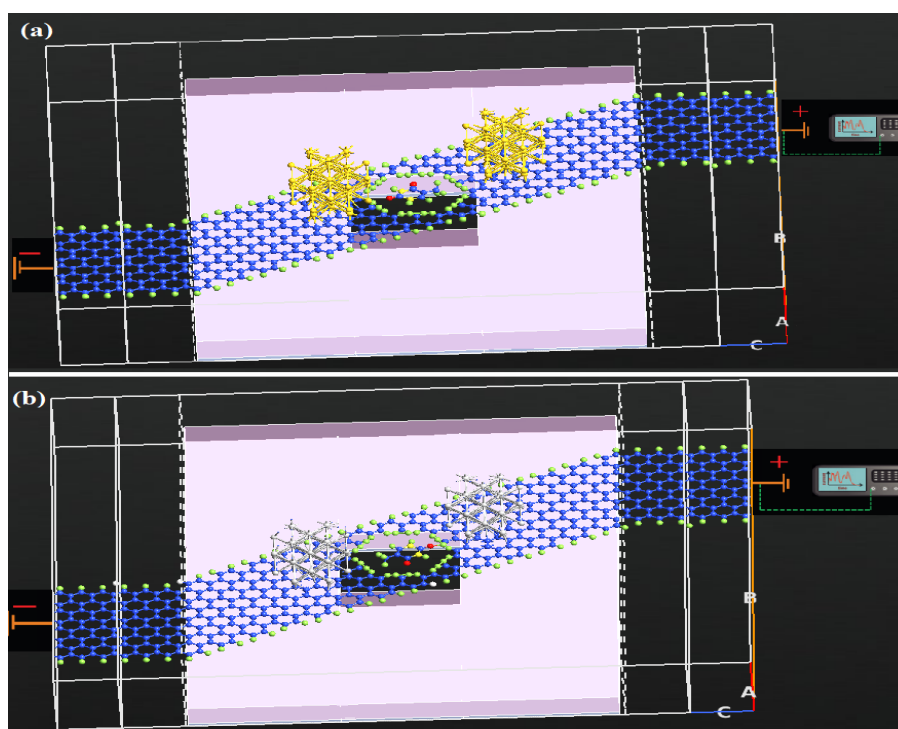
Figure 20: Z-shaped graphene field effect transistor. (a) Z-shaped graphene field effect transistor with a nanopore decorated with 10 Å gold nanoparticles. (b) Z-shaped graphene field effect transistor with a nanopore decorated with 10 Å silver nanoparticles. (Wasfi et al., 2020) © 2020 IOP.

2.1.3.3.3 Computational Methodology

A geometry optimization was performed as explained in Section 2.1.3.1.3. All optimizations were exceled by density functional theory as configured in Quantum-ATK -DFT package.

The electronic transport properties were calculated by NEGF+DFT simulations integrated in the Quantum-ATK package. Quantum-ATK-DFT was also used to calculate and simulate the transmission spectrum. Poisson equation with marginal conditions was utilized where Neumann boundary condition was applied to A and B directions which are perpendicular to the transport direction while Dirichlet boundary condition was applied to C direction. The Neumann boundary condition ensures that the electrostatic potential is constant and its derivative is zero (Wasfi et al., 2020) © 2020 IOP.

Perdew-Zunger (PZ) parametrization of the Local Density Approximation (LDA) and Troullier-Martins norm-conserving pseudopotentials were selected for exchange correlation of Quantum-ATK-DFT calculator (Perdew & Zunger, 1981). The pseudo-atomic local orbitals are single zeta polarized at hydrogen and carbon atoms and double zeta polarized at rest. 1 x 1 x 50 k-points were used for the Brillouin zone integration within Monkhorst-Pack scheme. A 75 Hartree mesh cut-off was used to calculate the charge density. A 200 sampling points were used within the range -2 to 2 eV, the gate voltage was set to 2 V, and the applied bias voltage among the right and left electrodes was set to 0.5 V (Wasfi et al., 2020) © 2020 IOP. The mathematical formalism used by the software has been explained in Section 2.1.3.1.3.

2.1.3.4 Dual Gate Field Effect Transistor of Graphene Nanoribbon with a Nanopore

For the fourth sensor, a semi-empirical technique was used to calculate the electron transport characteristics of the developed z-shaped graphene nanoribbon device to detect the DNA bases. Non-Equilibrium Green's Function (NEGF) integrated with semi-empirical methodologies were employed to analyze the different

electronic transport characteristics. The semi-empirical approach applied is an extension of the Extended Hückel (EH) method integrated with Self-Consistent (SC) Hartree potential. By employing the NEGF+SC-EH, it is proved that each one of the four DNA nucleobases positioned within the nanopore, with the hydrogen passivated edge carbon atoms, results in a unique electrical signature. Moreover, the sensor sensitivity was improved by using nitrogen instead of hydrogen to passivate the nanopore and by adding a dual gate to surround the central semiconducting channel of the z-shaped graphene nanoribbon.

2.1.3.4.1 Sensor Configuration

This sensor was investigated by using semi-empirical simulations. Figure 21(a) displays the nanoscale sensor configuration (without a gate), while Figure 21(b) shows a graphene nanoribbon field effect transistor. The sensor was built of three terminals: drain, source, and dual gate. The gate potential makes it possible to measure the sensor current and transmission spectrum where the gate is expected to enhance the sensor sensitivity. Two gates were added where each gate consists of dual layers: metallic and dielectric, where the constant of the dielectric layer is 4. One gate was placed under the central AGNR and the other gate is added above the channel. The carbon atoms edges were saturated by bonding along neighbor atoms. The nanoribbon carbon atoms edges were saturated by hydrogen or nitrogen. The cross section of the Dual Gate Z-shaped Graphene Nanoribbon FET (DG-ZGNR-FET) sensor is shown in Figure 22.

(a)

(b)
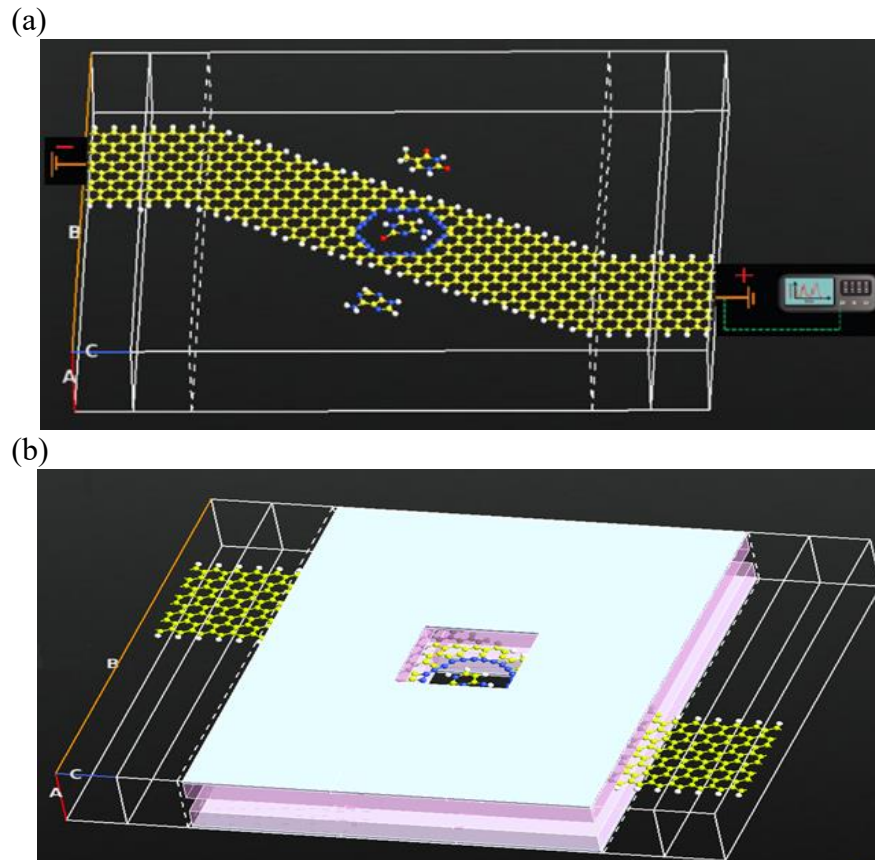
Figure 21: Schematic diagram of z-shaped sensor. (a) Schematic diagram of z-shaped GNR with a single DNA base passing within the pore. The edge carbon atoms of graphene nanopore are passivated with nitrogen while the edge carbon atoms of the GNR are passivated with hydrogen (Wasfi & Awwad, 2019b)© 2019 IEEE. (b) Schematic figure of the z-shaped FET with a pore. DNA bases go across the pore while the transverse electronic current is passing across the graphene sheet. The dual gate is biased at 1 V each side and the bias potential is fixed among the source and drain (+1.4 and −1.4 eV). Color code: hydrogen-white, carbon-yellow, oxygen-red, and nitrogen-blue.
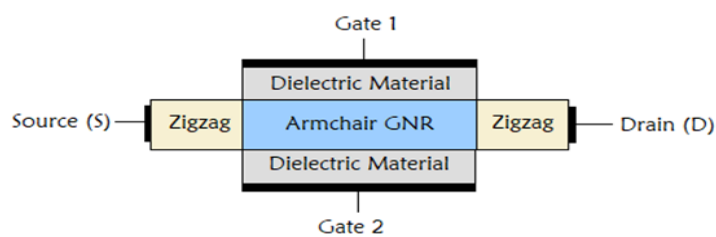
Figure 22: Cross-sectional view of the DG-ZGNR-FET sensor. The designed sensor is made of two electrodes and a semiconducting channel surrounded by two gates.

2.1.3.4.2 Computational Methodology

A geometry optimization was performed as explained in Section 2.1.3.1.3. In order to display the charge density, a mesh cut-off of 10 Hartree was fixed. The sampling k-points for the Brillouin Zone integration were 2x2x100 k-points. Poisson equation with marginal conditions was used where the electrostatic potential boundary condition of electrodes in the C direction was selected as a Dirichlet condition and the other two directions (A, B) were selected as a Neumann boundary condition. The Neumann boundary condition was employed to make sure that the electrostatic voltage was fixed and results in a zero derivative (Narendar, Gupta, & Saxena, 2018).

2.2 Experiment

The first aim of this work was to develop, design, and fabricate a Field Effect Transistor (FET) based sensor made of graphite oxide channel and decorate it with trimetallic nanoclusters of silver, gold, and platinum that are generated by an Ultra-High Vacuum Compatible (UHV) system. The sensor was utilized to detect various concentrations of DNA. Moreover, the sensor electrical characteristics and performance were verified by simulation as explained in Section 2.1.2 to confirm and explain the experimental results.

2.2.1 Experimental Research Design
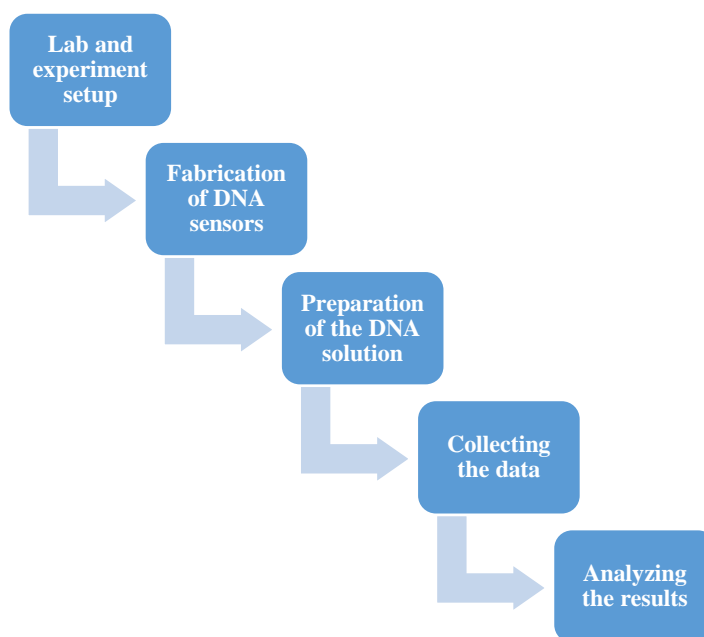
Figure 23: Experimental Research Design.

The experimental research was planned as displayed in Figure 23. It started by setting up the tools, machines and the required materials. Then, the required sensor was fabricated. After that, different concentrations of DNA were prepared. Finally, the sensor was tested and the data had been collected and analyzed. These steps are explained in details in Section 2.2.2.

2.2.2 FET Sensors based on Graphite Oxide Decorated with Trimetallic Nanoclusters

In this work, graphite oxide FET based sensor was designed, fabricated, and characterized for real-time detection of various concentrations of DNA with a detection limit of 5 ng/µL of DNA.

Step 1: Experiment setup

For this sensor, the following machines were used to develop, characterize, and test the required sensor: (i) Ultra-High Vacuum Compatible (UHV) system, (ii) thermal evaporation system (Torr machine), (iii) Energy-Dispersive X-Ray Spectroscopy (EDS), (iv) Scanning Electron Microscope (SEM), (v) Raman Spectroscopy, (vi) Ultraviolet (UV) Visible Spectrophotometer, (vii) Transmission Electron Microscopy (TEM) and (viii) a computer-controlled Keithley 236 source-measuring system. All of the above devices are available and accessible at UAEU.

Step 2: Design and fabrication of DNA detection sensors

DNA sensor was fabricated by utilizing a commercial sub-strate of p-type doped silicon (Si) wafer which has a top layer of silicon dioxide (SiO_2). The silicon wafer was divided into small parts of a size of 1.0cm ×0.5cm. Then, the silicon wafer was cleaned with acetone, ethanol, and deionized water. After that, the wafers were dried by nitrogen gas. Depositing the electrodes on the silicon wafer started by placing a 5 nm layer of Nickel-Chrome (NiCr) by thermal evaporation process, then 30 nm layer of gold (Au) was deposited through a stainless steel shadow mask displayed in Figure 24. The NiCr was deposited to enhance the adhesion between the gold electrodes and silicon wafer (Ayesh, Mahmoud, Ahmad, et al., 2014; Said et al., 2017). Commercial graphite oxide (GO) of 4 mg/mL was utilized in the fabrication process. A drop of the commercial GO was placed on top of the gap between the fabricated electrodes and left in room temperature for 24 hours. Figure 25 displays a schematic diagram of the sensor which has been developed and utilized to detect various concentrations of DNA.
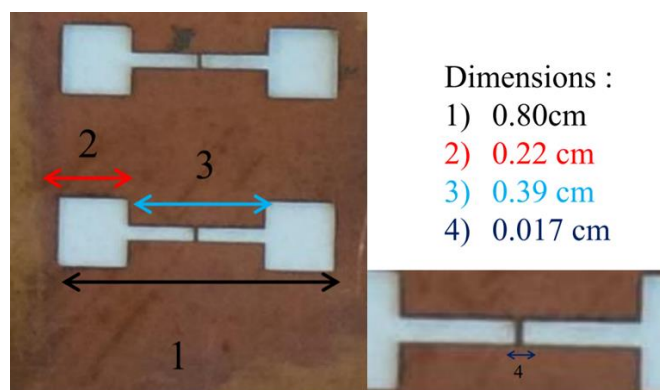
Figure 24: Stainless steel shadow mask.
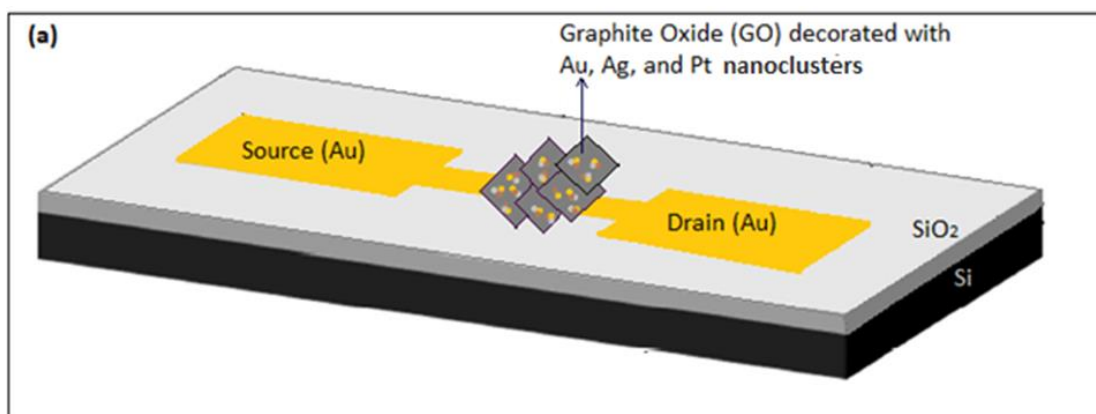
Figure 25: Schematic diagram of the transistor-based-sensor. The Au electrodes are connected through a channel of graphite oxide where the channel is decorated with composite trimetallic nanoclusters (Ag, Au, and Pt). Dimensions are not to scale, and the color-code are: gold-yellow, silver-light grey, and brown-platinum.

Step 3: Preparation of the DNA solution

Different concentrations of DNA samples were prepared. Plasmid DNA preparation was carried out using QIAGEN Midi Kit (QIAGEN) as per the manufacturer's instructions. Briefly, transformed bacterial were grown overnight in Lysogeny Broth (LB) media supplemented with ampicillin. Cells were pelleted and resuspended in P1 buffer where buffer P1 is a resuspension buffer used when purifying plasmid DNA and then lysed with P2 buffer where buffer P2 is a lysis buffer solution

produced by QIAGEN. Nucleic acid was precipitated by addition of solution P3 where precipitation is a procedure in which nucleic acid is precipitated by utilizing salt and alcohol and buffer P3 is a neutralization buffer used when purifying plasmid DNA followed by incubation on ice for 30 minutes. The DNA plasmid was then recovered by centrifugation, loaded onto Qiagen tip column, and eluted with QF buffer where buffer QF is the elution buffer used in QIAGEN Plasmid Kits for plasmid purification. Eluted Plasmid DNA was next precipitated using isopropanol, pelleted by centrifugation, washed with 70% ethanol, air dried before being resuspended in HyPure molecular biology water (Hyclone).

Step 4: Collecting the Data

While different concentrations of DNA bases were deposited on the sensor channel, the current-voltage (I-V) measurements were collected. Keithley 236 source measuring unit that is monitored by a computer was used to study the sensor performance by generating the current-voltage (I(V)) measurements (Ayesh, 2016). It was also utilized to detect the difference in electrical current due to DNA placement on the sensor to determine the sensor sensitivity.

Step 5: Analyze the results

The collected readings were analyzed in order to detect the different concentrations of DNA. To identify the ionic current under different concentrations of DNA, the experiment time was monitored.

Step 6: Evaluate the results

The results obtained from this sensor were analyzed and compared to previous relevant studies and simulation results. The test was repeated for different concentrations of DNA.

2.2.3 Fabrication of the FET Sensors Based on Graphite Oxide Decorated with Trimetallic Nanoclusters (Tools, Techniques and Procedures)

In this work, a FET sensor was fabricated to identify different concentrations of DNA. The FET device was fabricated through the following steps:

Step 1:

Thermal evaporation is the most common Physical Vapour Deposition (PVD) method. This technique is suitable for depositing various materials such as metals. Torr thermal evaporator system displayed in Figure 26 is made of a D-shaped stainless steel chamber, high voltage power supply, a turbo pump with a rotary pump to evacuate the system and reduce its pressure to 10^{-5} mbar, quartz crystal thickness sensor to measure the deposited metal thickness, and a two resistive thermal sources to generate the thermal current needed to evaporate the required material. This methods starts by heating the material needed to be deposited till evaporation starts. The material vapor settles in a thin film form on the cold substrate surface. The low pressure of 10^{-5} mbar is used to avoid the interaction between the material vapor and atmosphere which enables the vapor atoms to travel in straight lines. This thermal evaporation process was used to place the metallic electrodes on the surface of the Silicon Dioxide (SiO_2)/Silicon (Si) wafer. The electrodes were evaporated by using the torr machine shown in Figure 26. A stainless steel shadow mask was used to place the gold

electrodes. A drop of the graphite oxide solution was placed between the fabricated electrodes and it was left in room temperature for 24 hours.

Figure 26: Torr Machine.

Step 2:

Composite nanoclusters of gold, platinum and silver were deposited on the graphite oxide surface inside the Ultra High Vacuum compatible system (UHV) displayed in Figure 27 (Nanogen-50, Mantis Deposition Ltd. Oxfordshire, UK). Magnetron sputtering and inter gas condensation were deployed to generate nanoclusters from composite target of gold, platinum, and silver in ratio of 1:1:1 and 99.99% purity that was fixed on the magnetron sputter head. The UHV has two turbo pumps and a rotary pump to evacuate the system and reduce its pressure to 10^{-6} mbar (Al Dosari & Ayesh, 2013). Argon gas was used to produce plasma inside the chamber to sputter metal from the target by DC discharge power. Nanoclusters were then generated and traveled inside the UHV to be placed on the FET device. The

condensation of the sputtered nanoclusters was facilitated by Argon (Ar) gas (Al Dosari & Ayesh, 2013; Ayesh, Qamhieh, Mahmoud, & Alawadhi, 2012). The aggregation length (L), which is known as the interval between the exit nozzle and the target, was set at 70 mm. The argon-gas flow rate was fixed at 40 sccm, and the discharge DC power was set at 10.8 W. The nanocluster size can be modified by changing the Ar flow rate, aggregation length, and the DC discharge power (Ayesh, Mahmoud, Qamhieh, & Karam, 2014).
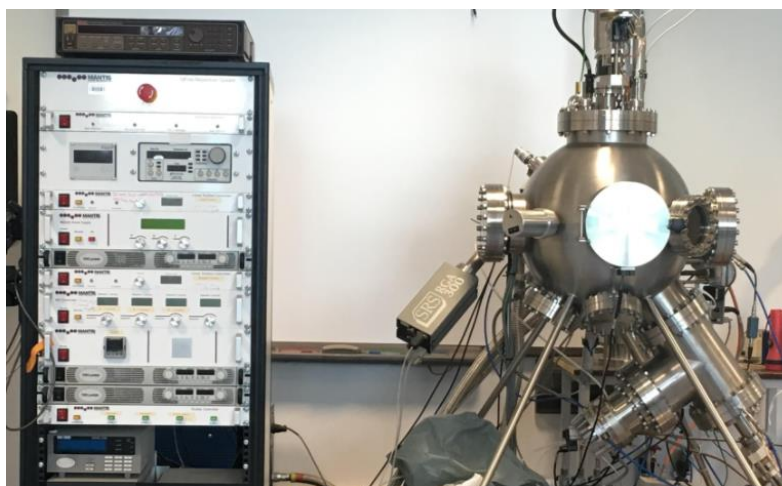
Figure 27: Vacuum compatible system.

Step 3

FET sensor characterization was performed by using: (i) Raman spectroscopy and UV-Vis spectroscopy to analyze the Graphite Oxide channel, (ii) a Quadrupole Mass Filter (QMF) was utilized to detect the nanoclusters size distribution. (iii) TEM was used to produce an image of the nanoclusters, and (iv) the nanoclusters composition was confirmed by employing Energy Dispersive x-ray Spectroscopy (EDS) technique.

Step 4

A Constant current was fixed across the membrane while the different concentrations of DNA bases were placed on the FET channel. The current-voltage (I-V) measurements were collected by utilizing a computer-controlled Keithley 236 source-measuring unit. After each measurement, the silicon wafer with the gold electrodes was cleaned with deionized water and the graphite oxide channel was placed to continue the other trials. The FET sensor electrical characteristics were checked before each trial.

Chapter 3: Results

This chapter presents the simulation and fabrication results of the developed sensors. It summarizes the collected data, observations, and measurements generated while conducting the procedures and methods illustrated in Chapter 2.

3.1 Simulation Results

This section summarizes the software simulation results, observations, and measurements.

3.1.1 Results of FET Sensors based on Graphite Oxide Decorated with Trimetallic Nanoclusters

The performance of the GO-FET bare sensor and the one decorated with monometallic and composite trimetallic nanoclusters was investigated. The DNA displayed in Figure 28 (a) is placed on top of the sensor as shown in Figure 28 (b) to study the sensors performance. The addition of composite metallic nanocluster results in higher drain current at the same voltage. The sensor bias voltage at 0.200 V and the current was 7.289 μA, while after adding the nanoclusters the sensor current was 7.795 μA. The sensor performance was examined for different concentrations of DNA. The current variation ΔI was used to evaluate the sensor sensitivity. Figure 29 shows the current variation (at V_{ds}= 0.200 V and V_g= 0 V) after placing different concentrations of DNA on each sensor channel. Figure 29 shows that ΔI is higher for the sensor after decoration with nanocluster which proves that the sensor with nanocluster has higher sensitivity than the bare sensor. Moreover, the figure depicts that the higher concentration of DNA results in an increment in the current variation.

(a)
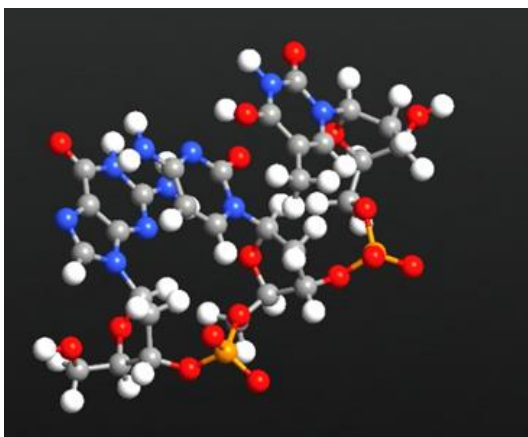
(b)
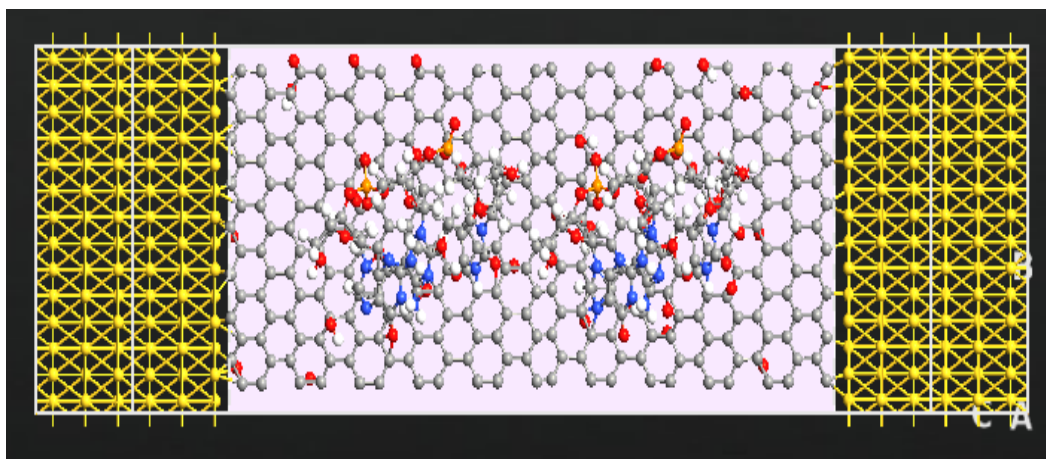
Figure 28: GO-FET with DNA. (a) DNA of Guanine, Cytosine, and Thymine. (b) GO-FET with DNA placed on the graphene oxide channel. Color code: carbon-gray, hydrogen-white, gold-yellow, phosphor-orange, and oxygen-red.
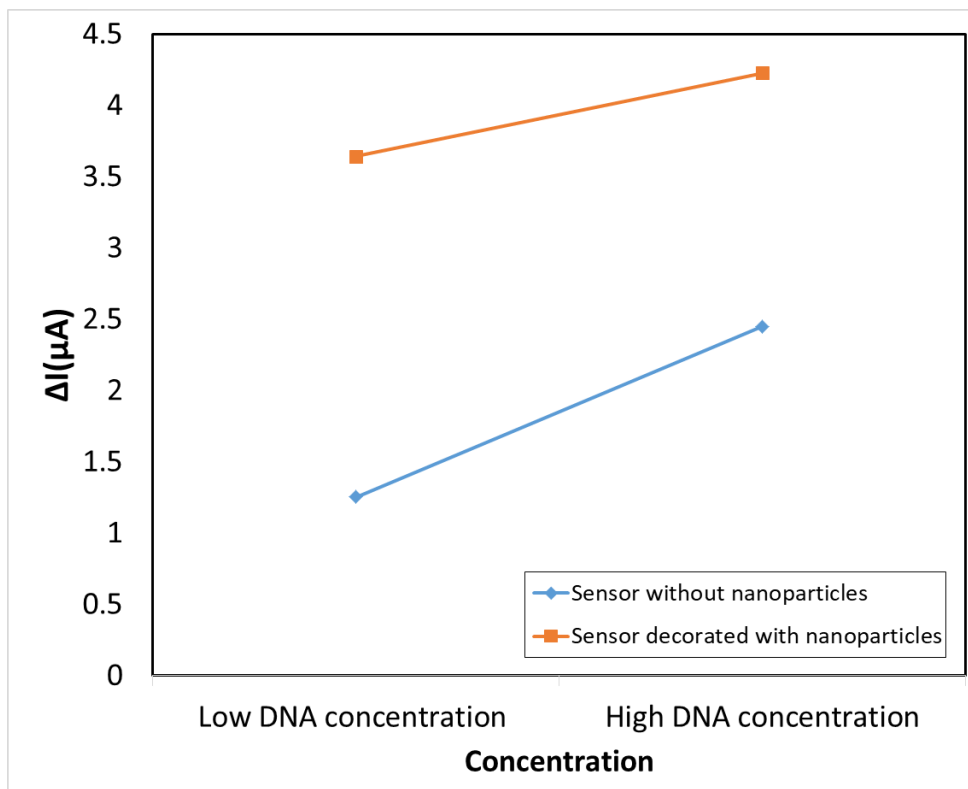
Figure 29: Variations in the electrical drain current due to different concentrations of DNA.

Figure 30 shows a comparison between sensors with monometallic nanoclusters of Au, Ag, and Pt and the sensor with trimetallic nanocluster (Ag, Au, and Pt) for different concentrations of DNA. The figure illustrates that the sensor decorated with trimetallic nanoclusters has higher drain current change than the other sensors. Thus, trimetallic nanoclusters of Au, Ag, and Pt were used in this experiment. Noble trimetallic nanoclusters are being used because of their promising features such as high sensitivity and selectivity and their multi-functional influence due to the existence of three metals within the nanocluster.
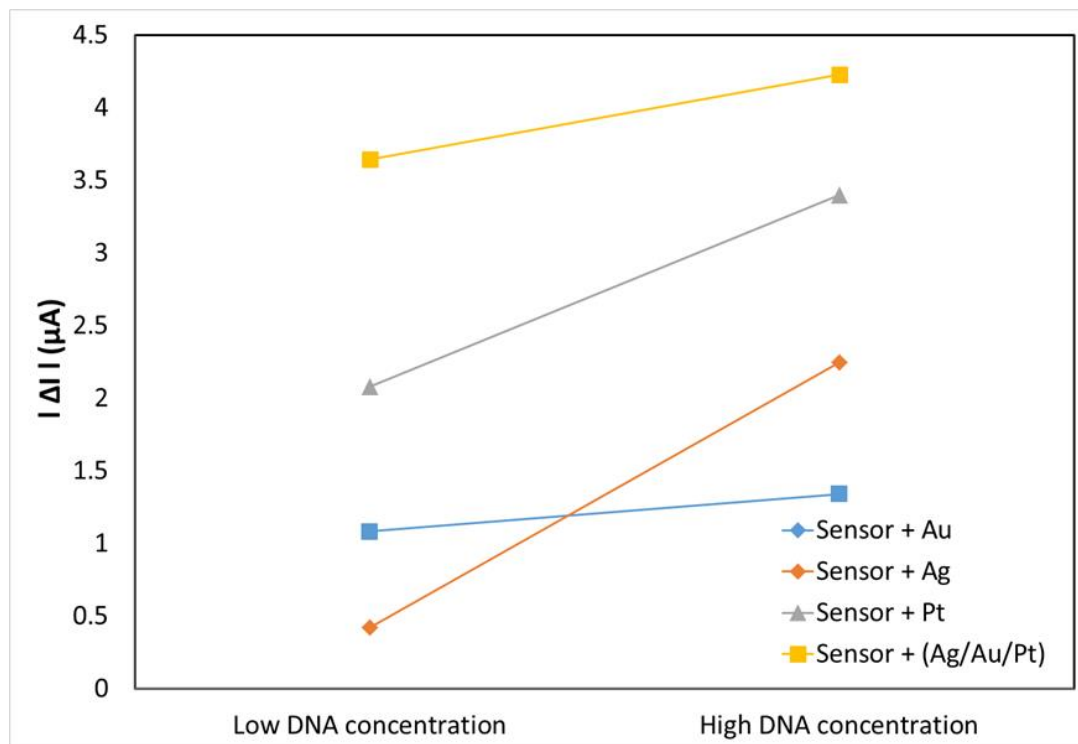
Figure 30: Variation in the electrical drain current of the sensor decorated with monometallic nanoclusters of Au, Ag, and Pt and trimetallic nanocluster (Ag, Au, and Pt) due to different concentrations of DNA.

3.1.2 Simulation of Graphene-based Sensor

This section introduces the simulation results of several sensors to identify the DNA bases.

3.1.2.1 Z-shaped graphene nanoribbon with a nanopore

This section demonstrates the transmission spectrum, conductance, and current for the z-shaped graphene nanoribbon with a nanopore (first sensor).

3.1.2.1.1 Transmission Spectrum

The first sensor transmission spectrum was calculated by ATK-DFT calculator. The transmission spectrum of the device with 10.1 Å nanopore, without applying any bias potential, is shown in Figure 31. The transmission spectrum reflects the central

semiconducting AGNR electronic structure. The transmission spectrum has a low value in the energy range [-1, 0.3] eV, corresponding to the energy window within the band gap of the central semi-conducting armchair-edge ribbon. Due to the absence of energy levels within this region, the electrons should tunnel to pass through the junction.
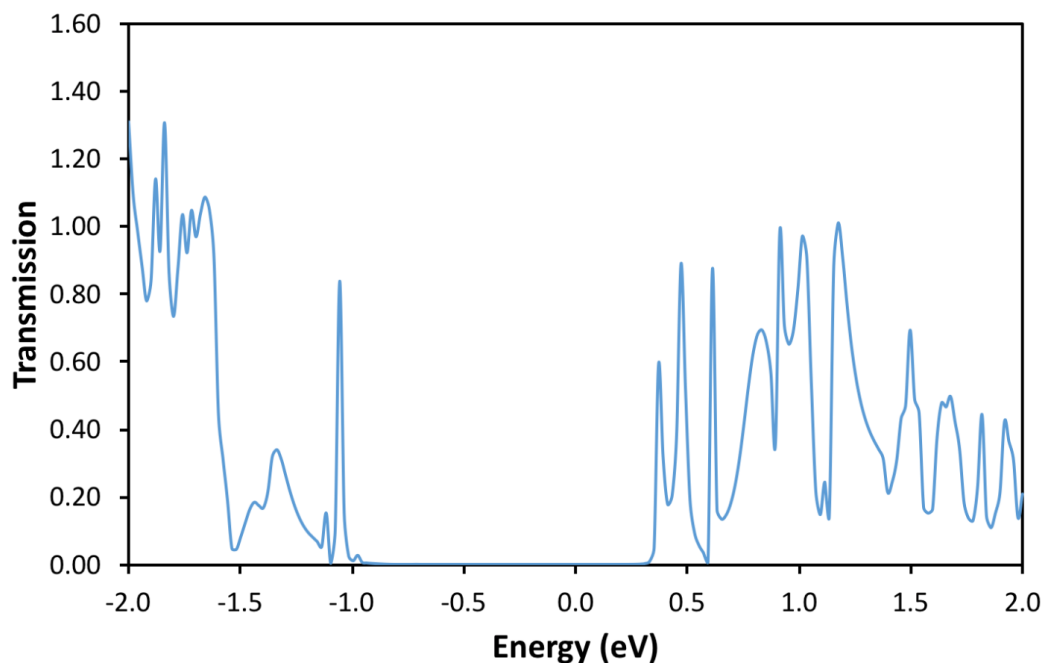
Figure 31: The zero bias transmission spectrum for z-shaped device with a nanopore in the middle.

Various orientations of the nucleobases occur through the graphene nanopore during the translocation of a DNA bases. Therefore, it is highly important to study the effect of nucleobase orientation on the transmission spectrum. The transmission spectrum at zero bias of the nanoscale sensor was computed for each nucleobase with various rotations. Each base was rotated 180° around x-axis, 180° around xy-plane, and 180° around xz-plane. The zero bias transmission spectrum was affected by the various types of base orientations.

The rotation effect of the nucleobases (Adenine, Guanine, Cytosine, and Thymine) on the transmission spectrum is shown in Figure 32. The figure shows how a transmission spectrum is influenced slightly by the various orientations. Each nucleobase was rotated from 0 to 180 around the x-axis, xy-plane, and xz-plane. For example, the four types of nucleobases orientations corresponding to 0° are shown in Figure 33.

3.1.2.1.2 Conductance

Figure 34 was produced using NEGF + DFT simulations. Figure 34 (a) shows the conductance resulted from various orientation of nucleobases presented in Figure 35. Figure 34 (b) shows the integration of the conductance with different orientations for each nucleobase inserted in the nanopore at room temperature (300 K). The conductance at room temperature was calculated from transmission spectra using Equation 2.2. Figure 34 reveals that purine base (Adenine and Guanine) have less conductance than pyrimidine bases (Cytosine and Thymine) due to the physical and chemical structures of these bases which make it possible to identify the two groups of DNA nucleobases at an applied bias voltage.

A critical issue is to study the signal modification when DNA bases orientation vary with respect to the nanopore. For selected orientation of DNA bases shown in Figure 35 (a-d), the conductance variations are displayed in Figure 34. The intervals in Figure 34 (b) should be considered as the limits on conductance variation since not all values within the interval will be sampled experimentally. Some of the bases orientations in Figure 35 were chosen to get maximum conductance variation and they require specific bending of DNA bases to place the base into such position.

This work illustrates that each DNA nucleobase will lead to a significant charge density modulation and to significant related electronic potential in the surrounding area.
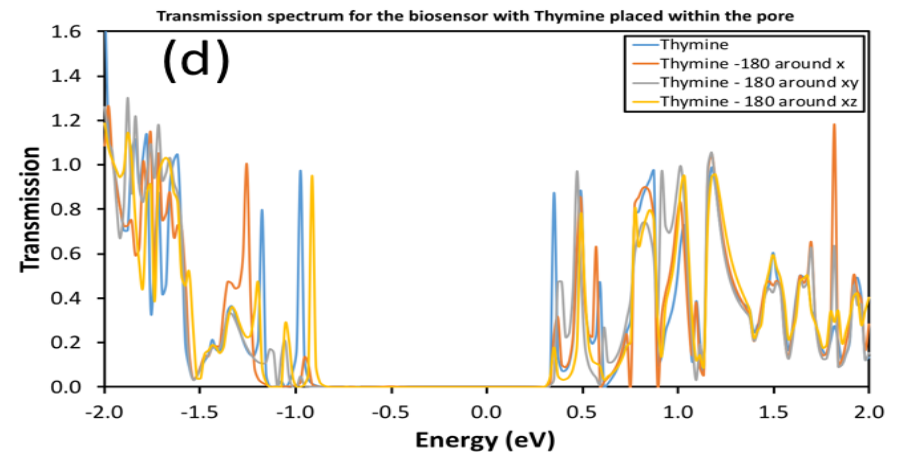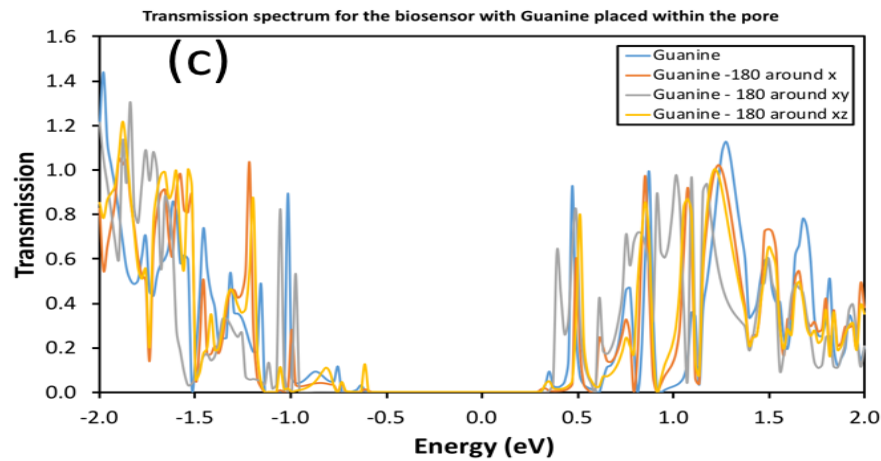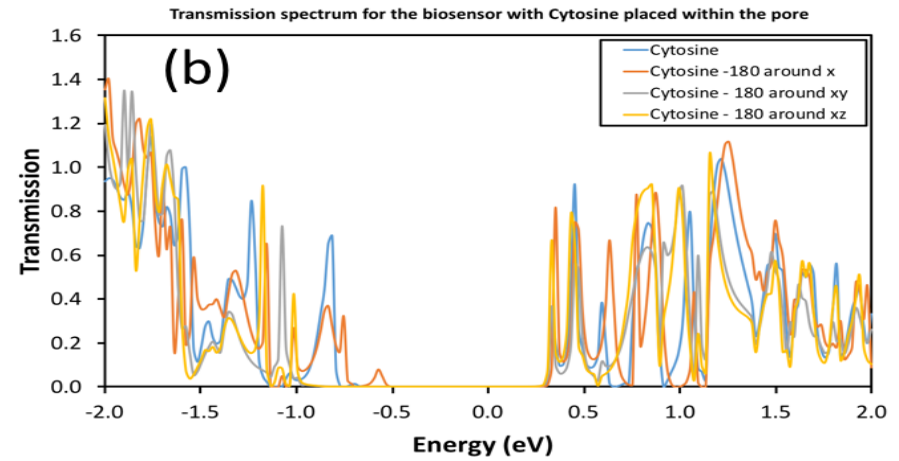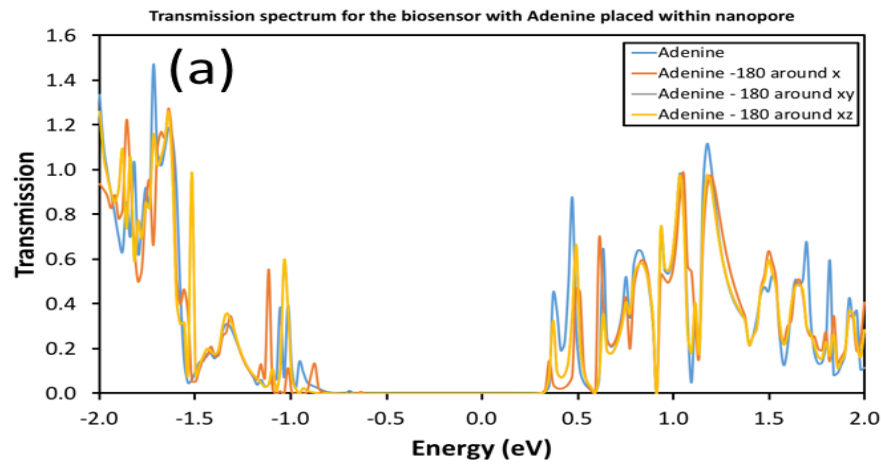
Figure 32: The zero bias transmission spectra for the four nucleobases: (a) Adenine, (b) Guanine, (c) Cytosine, and (d) Thymine. The transmission curves respective colors indicate the nucleobase orientation within the pore.
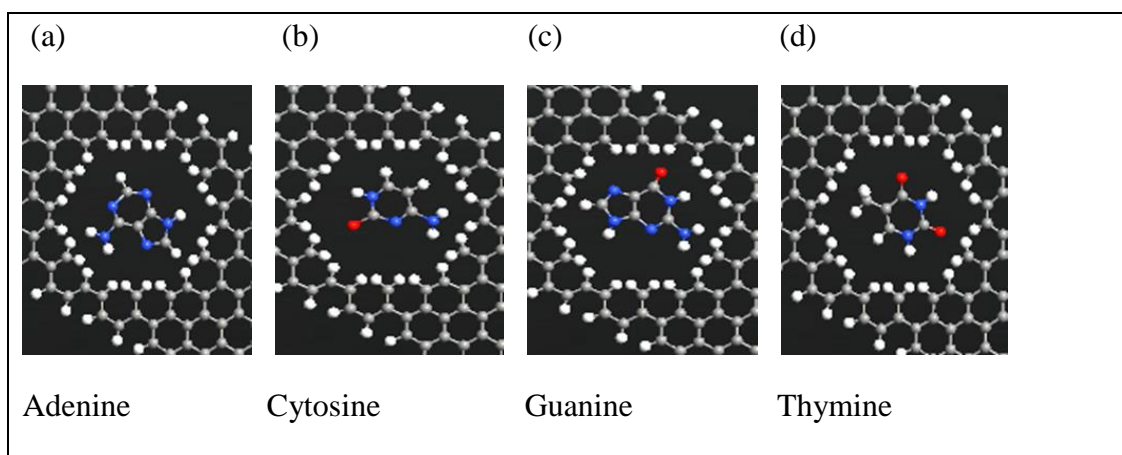
Figure 33: The four types of nucleobases orientations corresponding to 0°. (a) Adenine, (b) Guanine, (c) Cytosine, and (d) Thymine.
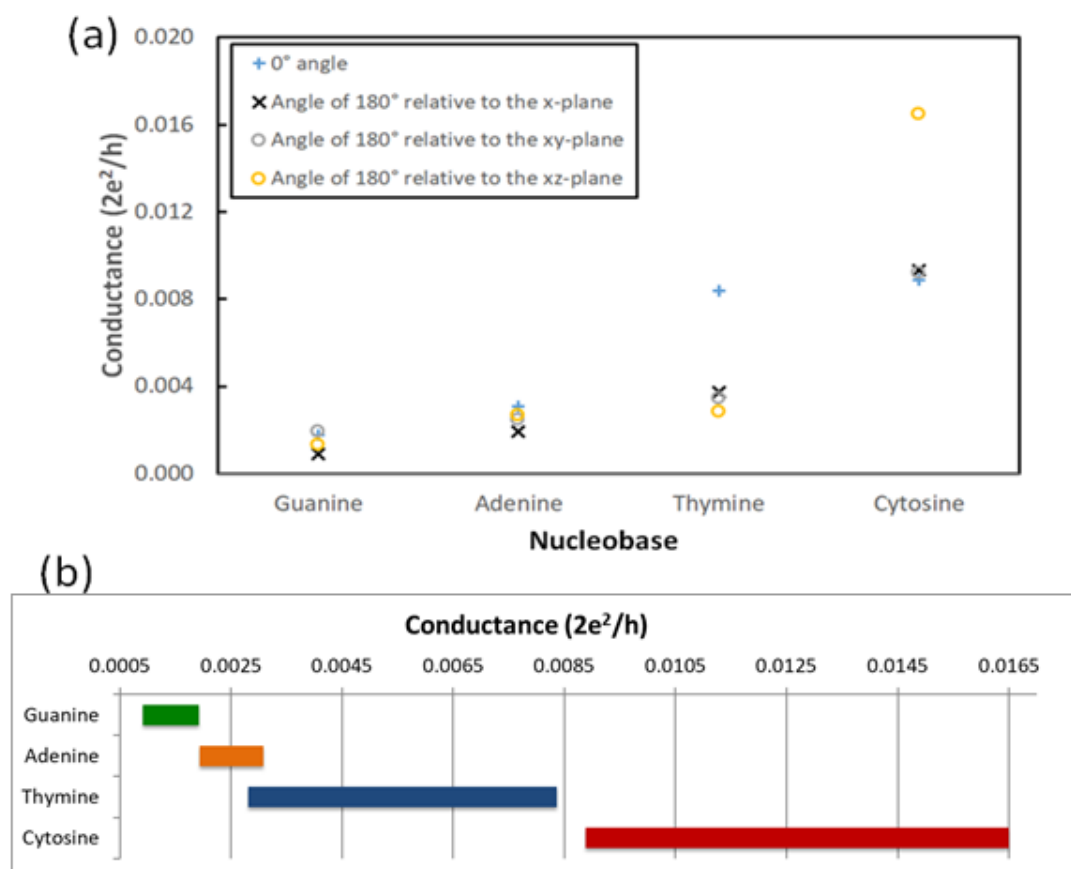
Figure 34: The room temperature conductance for the z-shaped sensor. (a) The room temperature conductance for the z-shaped sensor for each nucleobase inserted within the pore due to rotations. The conductance is calculated using quantum simulations by employing first principles model. (b) The room temperature conductance intervals due to rotations.
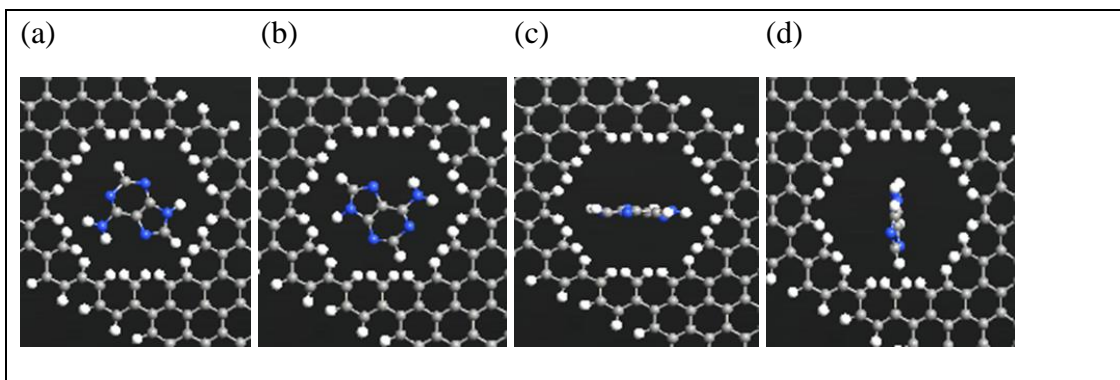
Figure 35: Adenine placed within the nanopore at various orientations. (a) Adenine placed within the nanopore at 0° angle. (b) Adenine at an angle of 180° relative to the x-plane. (c) Adenine at an angle of 180° relative to the xy-plane. (d) Adenine at an angle of 180° relative to the xz-plane.

3.1.2.1.3 Current

Figure 36 shows the electrical current variation because of nucleobase rotation. Thymine and Cytosine have higher current ranges than Adenine and Guanine which makes it easier to distinguish purine and pyrimidine bases. The current passing through each base, gives a unique signature as displayed in Figure 36. These electrical signatures differ for the various orientations of the bases.

The main idea is that when DNA bases go across the nanopore, the current passing through the graphene nanopore will be unique for each base A, C, G, and T. The current passing through the nanopore is affected by the electrostatic interaction among the pore and the bases which results in a difference in the local density of states in the graphene membrane around the pore. Placing a DNA base in graphene nanopore affects the charge density in the surrounding area. This leads to a distinctive current for each nucleobase. The current was measured from the integrated density of state. The DNA bases translocation through the nanopore lead to different orientation of the nucleobases which will affect the current.

Finite bias voltage was applied between the source and the drain $V_b = V_s - V_d$. The various spatial extension of the nucleobases affects their contribution to the density of states where the density of states was used to calculate current and conductance. These variations in the spatial extension are influenced by the nucleobase orientation and geometry.

DNA is made up of different bases attached to sugar phosphate backbone. The backbone contribution was ignored, as the background noise coming from the backbone may be determined and subtracted from the signal of individual nucleobases. The four bases are categorized into two groups: the pyrimidine bases Cytosine and Thymine and the purine bases Adenine and Guanine. The base size is the main distinctive feature between purine and pyrimidine bases. The pyrimidines bases consist of six membered ring while the purine bases consist of a six and a five membered ring. This classification is based on the chemical structure. Since purines are larger, they would interact more strongly in a confined space. This leads to smaller separation and stronger coupling of G and A with the nanopore.

Pyrimidine and purine will have differences in their electronic states and spatial extension which will result in a difference in the density of states of the nucleobases placed within the nanopore.
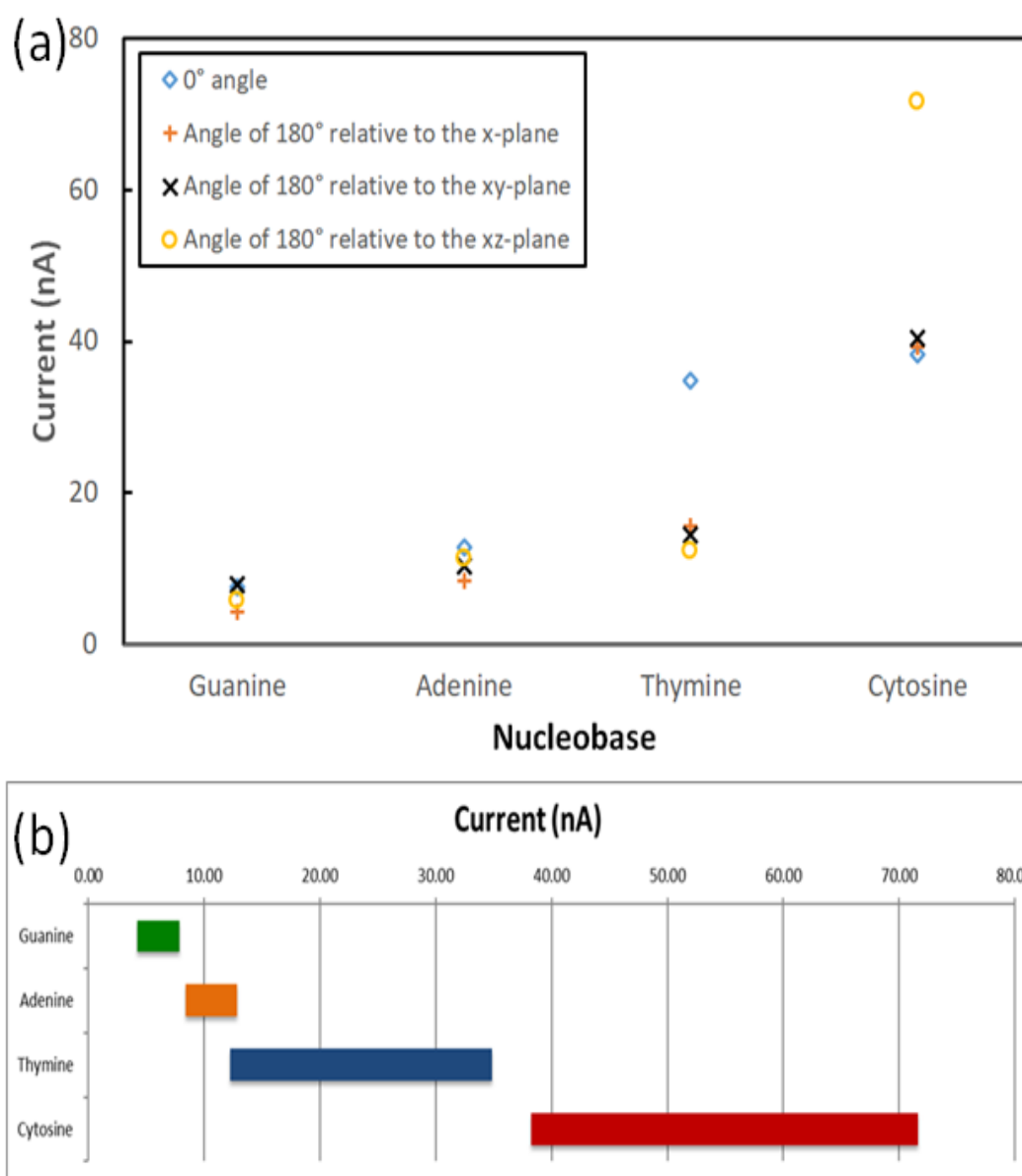
Figure 36: Current variations due to nucleotide orientations. (a) Current variation due to nucleotide rotation in the z-shaped graphene nanoribbon sensor pore at 0.5V bias; (b) Current intervals due to nucleotide rotation at 0.5V bias.

3.1.2.2 Z-shaped Graphene Nanoribbon with a Nanogap

This section demonstrates the transmission spectrum, and current results for

the z-shaped graphene nanoribbon with a nanogap (second sensor).

3.1.2.2.1 Transmission Spectrum
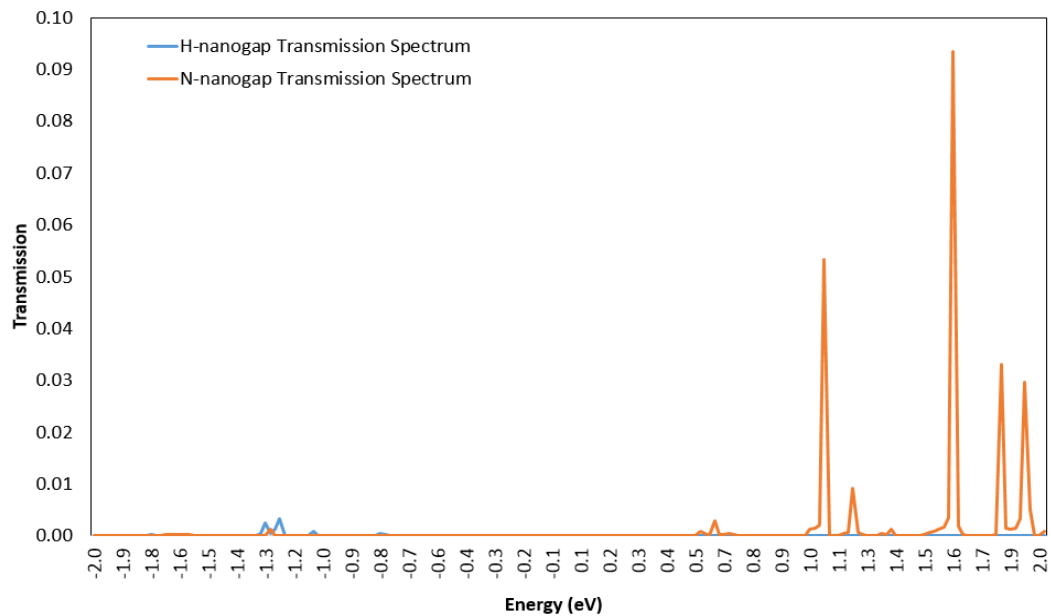
Figure 37: The transmission spectrum at 2 V bias voltage for Adenine within a nanogap whose edge carbon atoms are passivated by hydrogen (H-nanogap) or nitrogen (N-nanogap). (Wasfi & Awwad, 2019a)© 2019 IEEE.

Figure 37 displays the 2 V bias transmission spectrum for Adenine within 1.01 nm nanogap in the center of the z-shaped graphene nanoribbon sensor. The transmission spectrum for Adenine within H-nanogap and N-nanogap was calculated resulting in higher and more pronounced current for N-nanogap. The transmission spectrum displayed in Figure 37 reflects that the N-nanogap sensor current is higher than the H-nanogap sensor current (Wasfi & Awwad, 2019a)© 2019 IEEE.

3.1.2.2.2 The Transverse Current
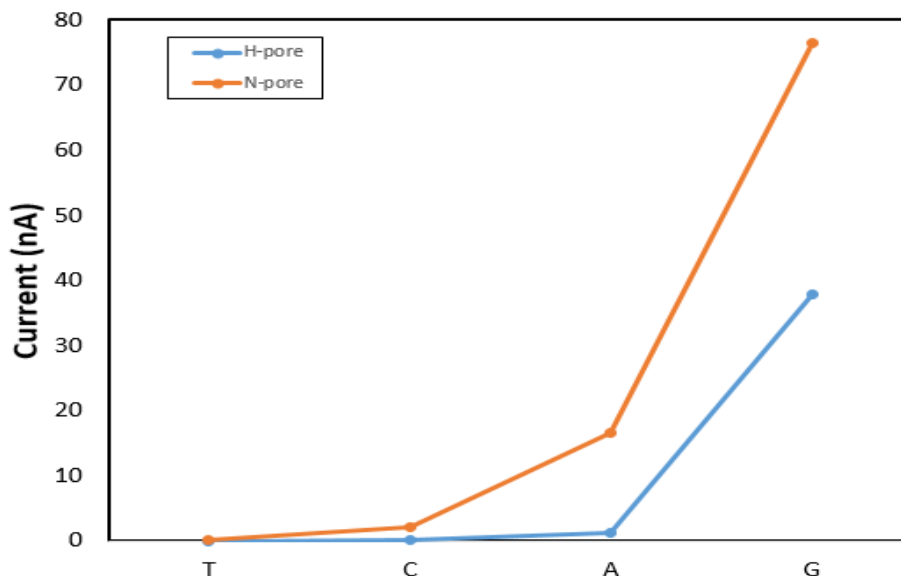
Figure 38: The room temperature current of the z-shaped sensor when one of the four DNA bases (A, C, G, T) is placed within the 1.01nm nanogap whose edge carbon atoms are passivated by either hydrogen (H-nanogap) or nitrogen (N-nanogap). (Wasfi & Awwad, 2019a)© 2019 IEEE.

Figure 38 was generated using NEGF+DFT simulations. This figure displays the current at room temperature for each of the four DNA bases (Adenine, Cytosine, Thymine, and Guanine), which are displayed in Figure 39, where each of the bases was placed within H-nanogap and N-nanogap and 2 V bias voltage was applied at room temperature (300 K). The transverse current was calculated using Equation 2.2. Figure 38 shows that N-nanogap enhances the current since N-bonds improve the coupling among the bases and the nanogap. Using N-nanogap enhances the sensor sensitivity and results in higher current that is easier to detect and measure (Wasfi & Awwad, 2019a)© 2019 IEEE.

The current for two orientations for each base within a N-nanogap and H-nanogap is generated using ATK-VNL. Each base was rotated 180 around x-axis

within N-nanogap and H-nanogap as displayed in Figure 40 (Wasfi & Awwad, 2019a)© 2019 IEEE.
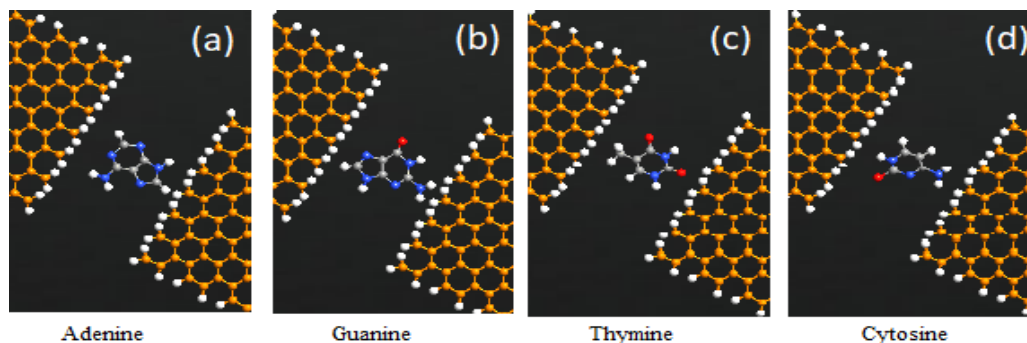
Figure 39: The four types of DNA bases (Adenine, Guanine, Thymine, and Cytosine with 0° orientation. (Wasfi & Awwad, 2019a)© 2019 IEEE.
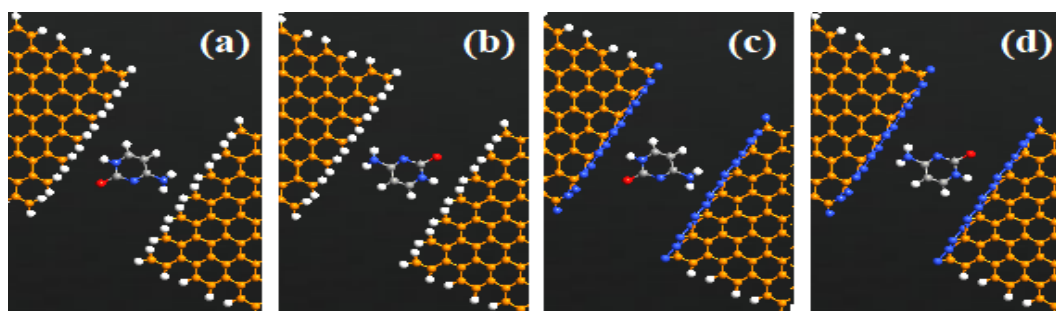
Figure 40: Cytosine placed within graphene nanogap. (a) Cytosine placed within H-nanogap at 0° angle. (b) Cytosine placed withing H-nanogap at an angle of 180° relative to x-axis. (c) Cytosine placed within N-nanogap at 0° angle. (d) Cytosine placed withing N-nanogap at an angle of 180° relative to x-axis. (Wasfi & Awwad, 2019a)© 2019 IEEE.

Figure 41 and Figure 42 were generated by NEGF + DFT simulations. For the selected orientations of DNA bases within H-nanogap shown in Figure 40 (a-b), the current variations are displayed in Figure 41. While, for the selected orientations of DNA bases within N-nanogap shown in Figure 40 (c-d), the current variations are displayed in Figure 42. Both figures show that purine bases have higher current rates than pyrimidine bases due to the different chemical and physical structures for each group.

Each of the four DNA bases has its own electronic signature and it is more pronounced

with N-nanogap (Wasfi & Awwad, 2019a)© 2019 IEEE.
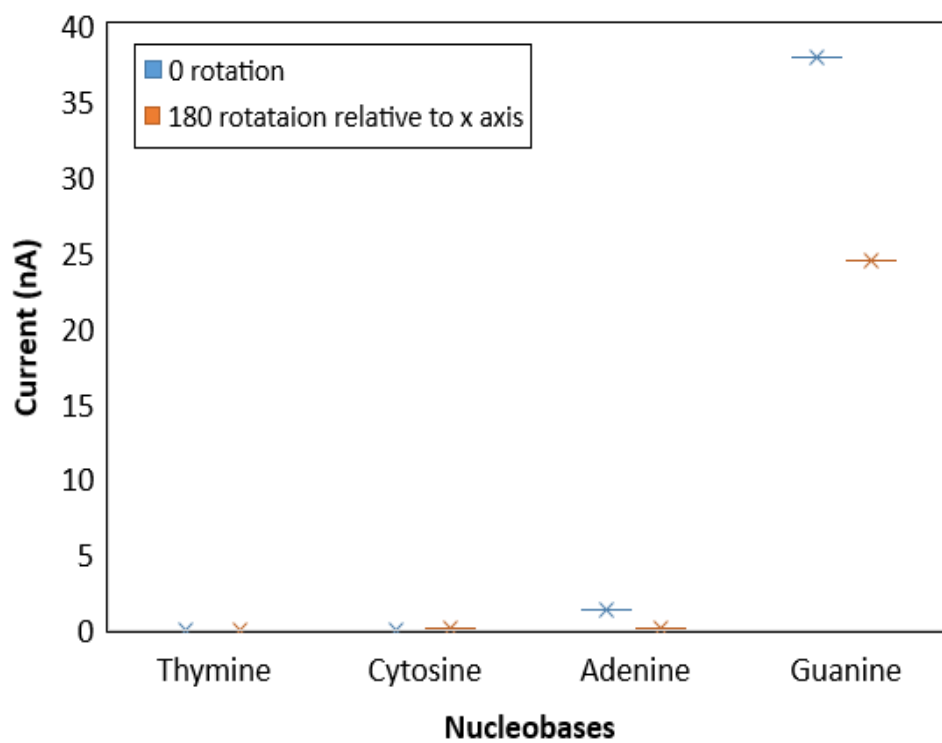
Figure 41: Current variation due to nucleotide (A, C, G, and T) rotation in the z-shaped graphene nanoribbon sensor H-nanoogap at 2 V bias. (Wasfi & Awwad, 2019a)© 2019 IEEE.
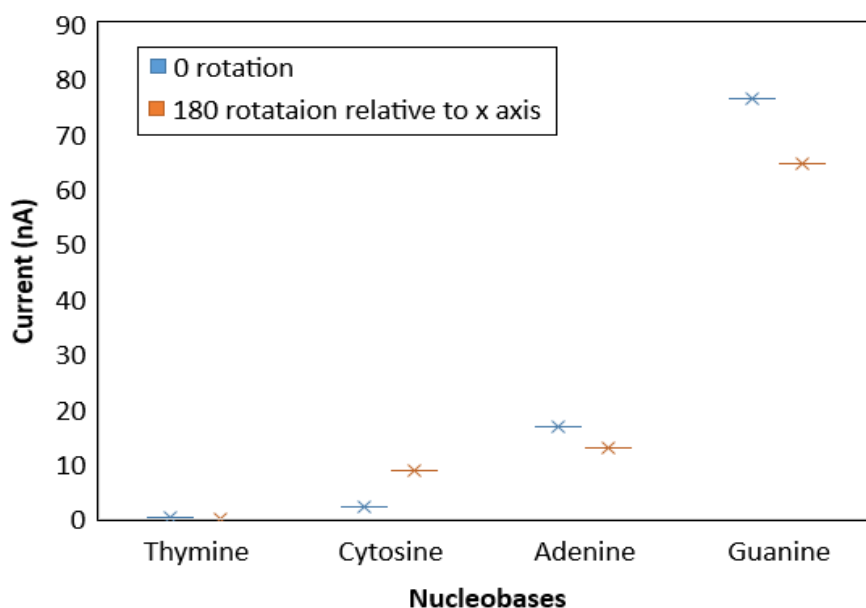
Figure 42: Current variation due to nucleotide (A, C, G, and T) rotation in the z-shaped graphene nanoribbon sensor N-nanoogap at 2 V bias. (Wasfi & Awwad, 2019a)© 2019 IEEE.

3.1.2.3 Z-shaped Graphene Nanoribbon Field Effect Transistor Decorated with Nanoparticles

This section demonstrates the transmission spectrum, and current results for the z-shaped graphene nanoribbon field effect transistor decorated with nanoparticles (third sensor).

3.1.2.3.1 Transmission Spectrum

Figure 43 displays the transmission spectra of the z-shaped graphene nanoribbon field-effect transistor sensor that contains a bare nanopore and with gold and silver nanoparticles at 0.5 bias voltage and 2 V gate potential. It was noticed that the low value of transmission spectra within the energy range -1.4 to -0.1 eV correspond to the energy window of the central semiconducting AGNR bandgap. The transmission spectra displayed in Figure 43 indicate that sensor transmission peaks

without gold or silver nanoparticles is more than that with gold and silver nanoparticles (Wasfi et al., 2020) © 2020 IOP.
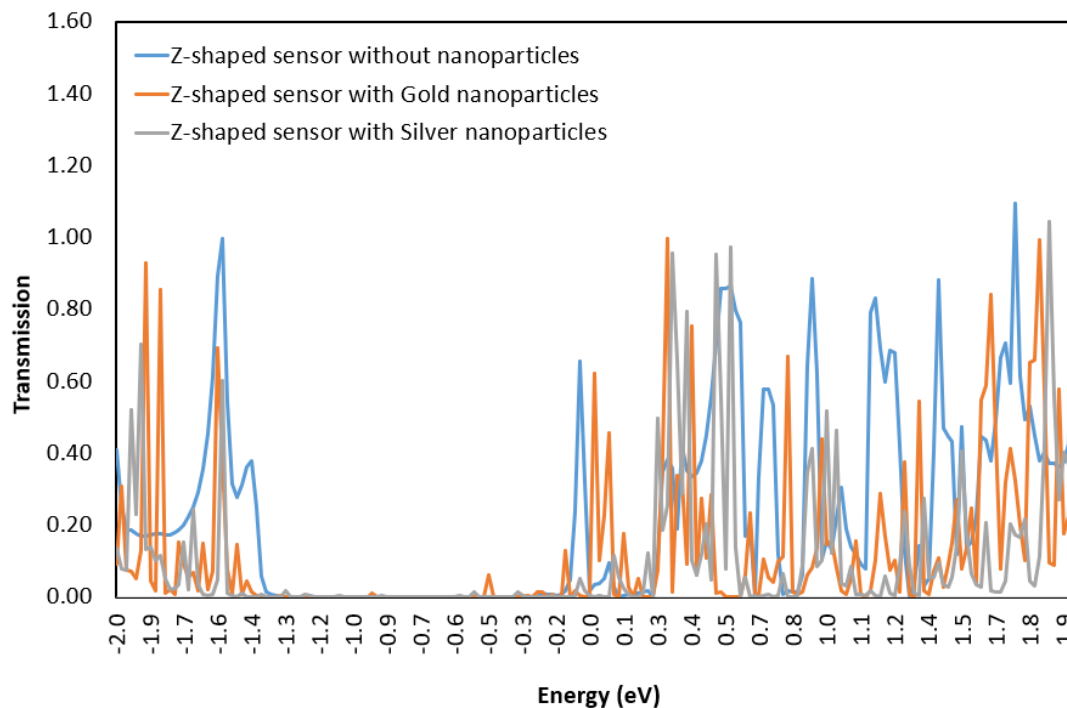
Figure 43: Transmission spectra of the z-shaped graphene field-effect transistor with a nanopore (0.5 V bias voltage and 2 V gate potential) for bare sensor as well as for sensors with silver and gold nanoparticles. (Wasfi et al., 2020) © 2020 IOP.

Figure 44 shows the four types of DNA bases corresponding to the orientation 0°, while Figure 45 shows the bases rotated from 0° to 180° around the x-axis, xy-plane, and xz-plane. The transmission spectra and current are not affected by how the right and left electrode voltages are applied and only relies on the difference between the electrodes' voltages. The effect of DNA bases translation on the transmission spectrum was studied where each DNA base was translated along the z-axis by ±1 Å. Each base was moved 1 Å to the left direction and 1 Å to the right direction as displayed in Figure 46. Figure 47 displays the transmission spectra as a function of energy for the sensor with a nanopore at room temperature (300K). The various panels

display the different bases within the nanopore (A, C, G, and T). Each panel shows the transmission spectra for each base due to the four orientations displayed in Figure 45. Each panel shows that the four orientations have similar transmission characteristics resulting in a unique current interval for each base. Moreover, the transmission spectra for the different panels vary in their transmission characteristics and number of transmission peaks (Wasfi et al., 2020) © 2020 IOP. Figure 47 reveals that purine bases resulted in lower current than pyrimidine bases due to their different size and structure.

The transmission spectra change due to the lateral transition for each base is displayed in Figure 48. The figure shows how a transmission spectrum is influenced slightly by the radial translation. This slight change in transmission spectrum resulted in currents within a unique current interval for each base.

Figure 49 displays the transmission spectra for Cytosine within the nanopore of the z-shaped graphene nanoribbon sensor: bare as well as with silver and gold nanoparticles.
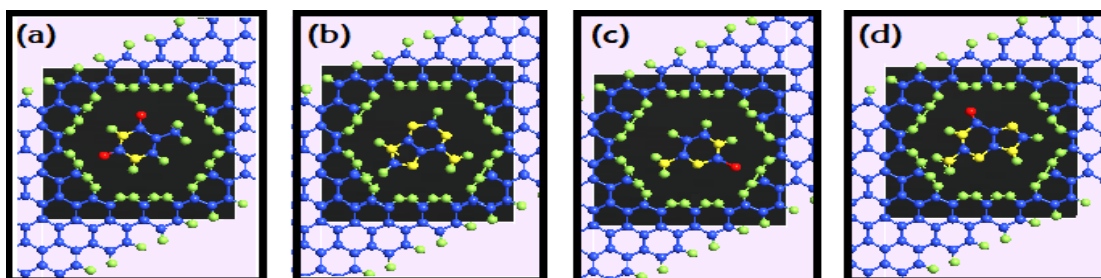
Figure 44: The four DNA bases with a 0° angel: (a) Thymine, (b) Adenine, (c) Cytosine, and (d) Guanine. (Wasfi et al., 2020) © 2020 IOP.
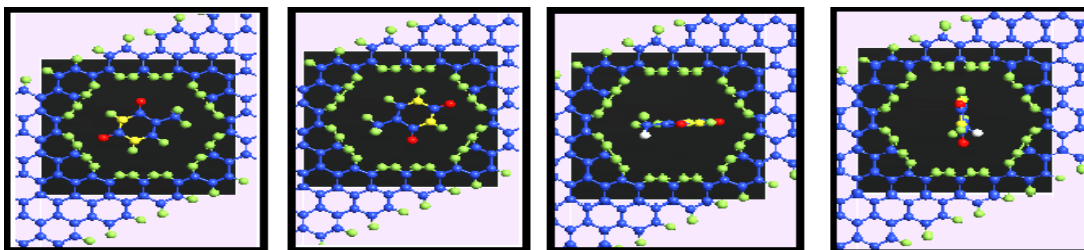
Figure 45: Thymine within graphene pore. (a) Thymine within the pore at 0° angle. (b) Thymine at 180° angel corresponding to the x-plane. (c) Thymine at 180° angel corresponding to the xy-plane. (d) Thymine at 180° angel corresponding to the xz-plane. (Wasfi et al., 2020) © 2020 IOP.
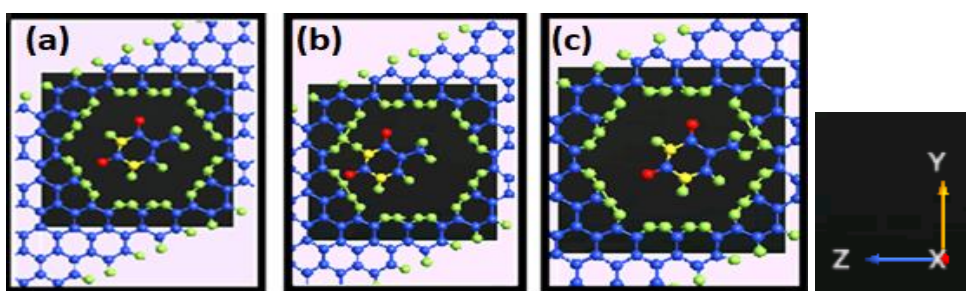
Figure 46: Thymine within the pore at various translations. a) Thymine within the pore at 0° angle. (b) Thymine due to -1 Å translation along the z-axis. (c)Thymine due to 1 Å translation along the z-axis. (Wasfi et al., 2020) © 2020 IOP.
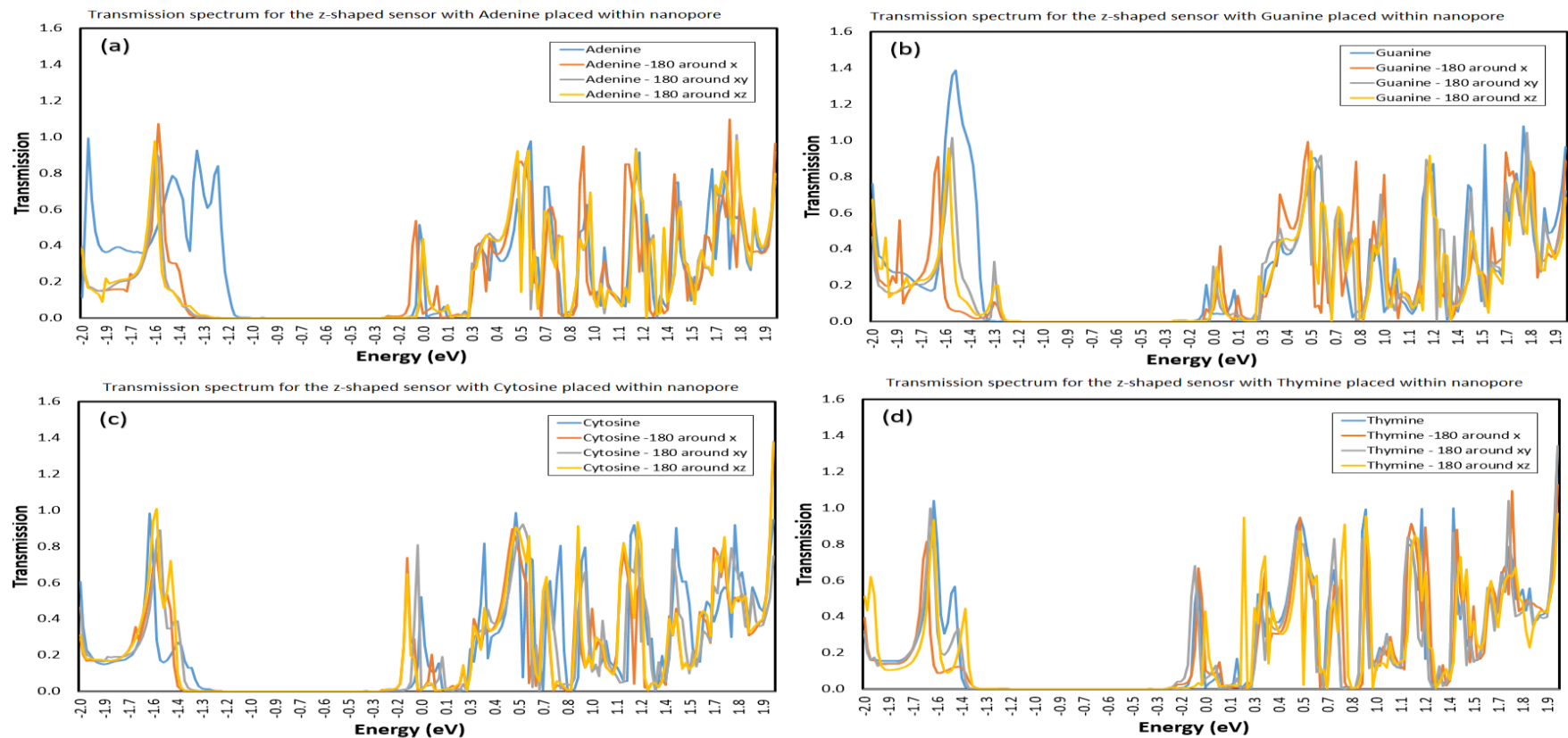
Figure 47: Transmission spectra of the z-shaped graphene field-effect transistor with a nanopore at 0.5 V bias voltage and 2 V gate potential for the four types DNA bases: (a) Adenine, (b) Guanine, (c) Cytosine, and (d) Thymine. The transmission spectra colors refer to the base orientation within the sensor nanopore (Wasfi et al., 2020) © 2020 IOP
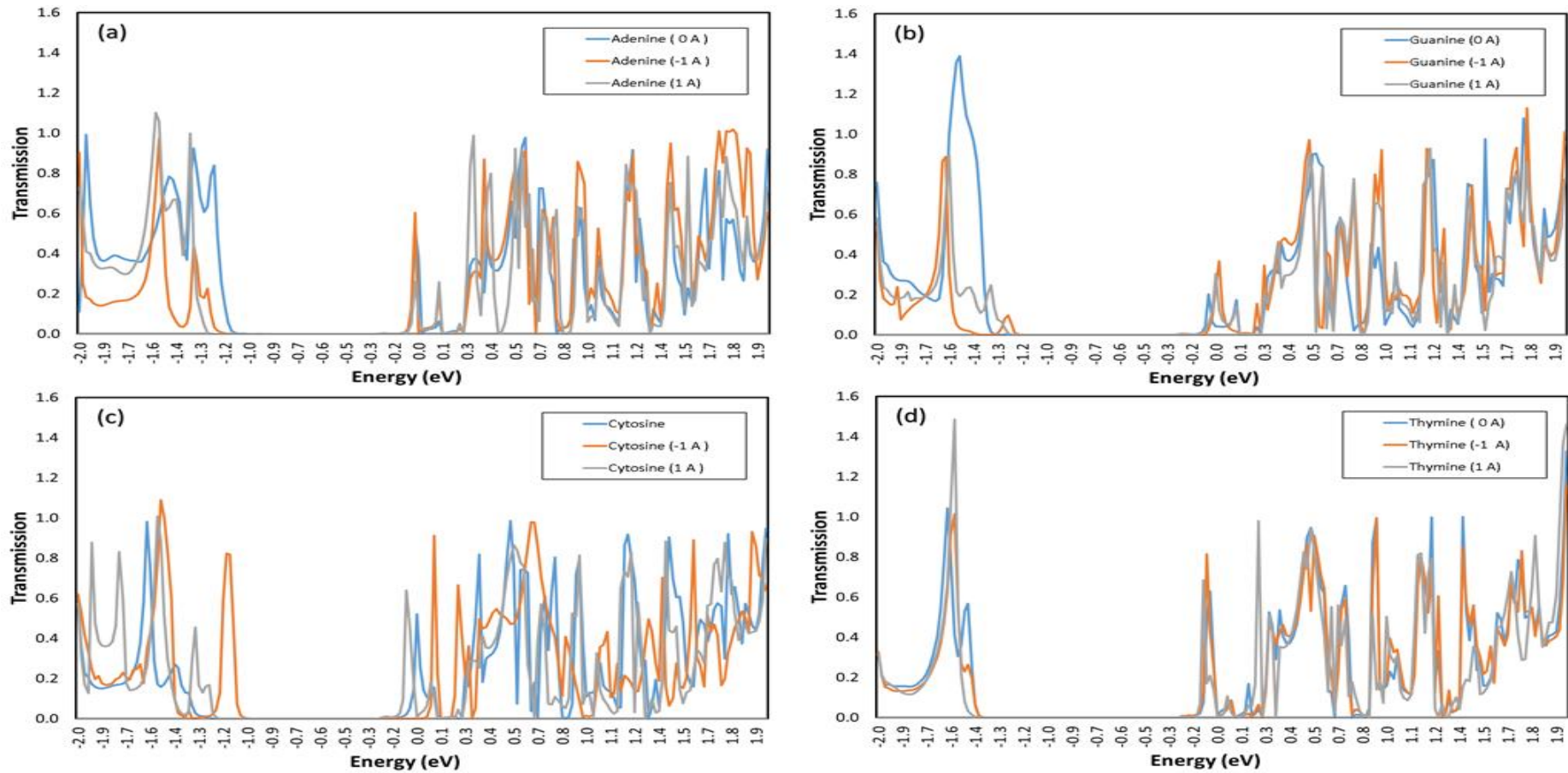
Figure 48: The transmission spectra change due to ±1.0 Å translation along the z-axis for: (a) Adenine, (b) Guanine, (c) Cytosine, and (d) Thymine. The transmission spectra colors refer to the base orientation within the sensor nanopore (Wasfi et al., 2020) © 2020 IOP.
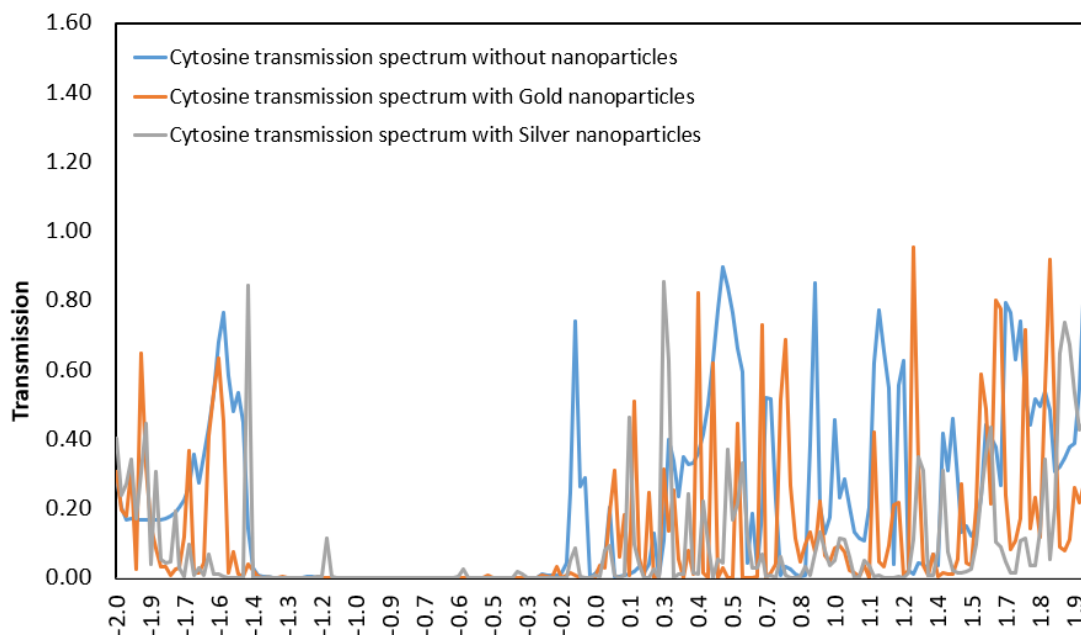
Figure 49: Transmission spectra of the z-shaped graphene field-effect transistor with a nanopore for Cytosine at 0.5 V bias voltage and 2 V gate potential for bare sensor as well as with silver and gold nanoparticles. (Wasfi et al., 2020) © 2020 IOP.

3.1.2.3.2 Current

Figure 51 reveals the current for the four angular orientations and the translation for each DNA base within the z-shaped graphene nanoribbon sensor nanopore. To generate an electrical transmission spectrum, a gate potential of 2V was fixed and the voltage among the right and left electrodes was fixed as +0.25 and −0.25 V. For DNA detection via nanopore, the current is the measured value rather than the transmission spectrum. Thus, the transverse current was calculated by integrating the transmission spectra as shown in Equation 2.3. For a specific DNA base orientation displayed in Figure 45 (a-d) and translation displayed in Figure 46 (a-c), the current variations are displayed in Figure 51 (a).

Figure 51 displays how each DNA base placed within the sensor nanopore modifies the sensor room temperature current. When bases orientations with respect

to the nanopore change as in Figure 45, and when bases were translated along the z-axis, the current changes within the ranges displayed in Figure 51 (b). The DNA current detection was achieved at bias voltage = 0.5V where the current is of the order of microampere. This current is predicted to be higher than the noise resulting from DNA structure fluctuations while translocating through the nanopore. Underneath the channel, a gate made of metal was added in order to have a three-terminal device which is eventually a FET device. The gate was supplied with 2V. Figure 51 reveals that the resulting currents are at the microamperes level which indicates much better sensitivity compared to the previous sensor in Section 3.1.2.1.

The phosphate and sugar backbone is adjacent to the nucleobases which affects the current modulation. However, it is expected that these factors will result in small noise on the resulting current which is systematic and can be deducted. Since this kind of noise is systematic, it can be possibly detected and eliminated as well as the fluid fluctuations while passing through the nanopore (Ahmed et al., 2014; McFarland, Ahmed, Zhu, Balatsky, & Haraldsen, 2015). The resulting transverse current for each base is anticipated to be higher than the DNA fluctuations and the effect on the electronic structure of DNA nucleotides within salt solution (Postma, 2010; Prasongkit et al., 2011; Saha et al., 2012). Previous studies show that the noise resulting from sugar-phosphate backbone can be detected and deducted from the general spectra (Ahmed et al., 2014; McFarland et al., 2015). This kind of simplification refers to the possibility of isolating the signal from the individual bases by subtracting the noise resulting from the sugar-phosphate backbone. The nucleotides current change is expected to be small and within the intervals shown in Figure 51 (b).

The nanopore diameter of 1 nm allows one single nucleotide to translocate at a time as displayed in Figure 50. The nanopore size of 1 nm is suitable for single stranded DNA sequencing which agrees with other studies (He et al., 2011; Zwolak & Di Ventra, 2005). The ideal nanopore diameter is 1 to 1.5 nm (Postma, 2010; Saha et al., 2012) which allows the single stranded DNA to go through it in unfolded state with a large and readable transverse current.

The real sensor application will include a substrate below the nanoribbon such as SiO_2 or Si_3N_4 underneath. The substrate and solvent effects were not considered in the conducted proof-of-concept simulations and were left for a future work. It should be noted that other studies conducted DNA base detection without considering the substrate and solvent effects (Prasongkit et al., 2011; Saha et al., 2012).

Since the DNA bases are very similar, they can be distinguished by their electronic state, size, and interaction with the nanopore. Each base density of states contribution at the Fermi level is unique due to the different spatial extension of each base. This contribution is highly affected by the bases orientation and geometry. The transverse current is highly sensitive to atomic scale variations, orientation, and distance. That is why specific configurations are preferred for DNA passage through a nanopore (Wasfi et al., 2020). The current is multiple orders of magnitude greater than the transverse current utilized in previous sensors (Prasongkit et al., 2011; Wasfi, Awwad, & Ayesh, 2019).
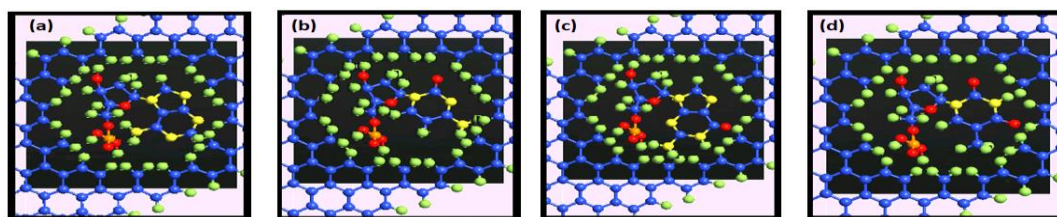
Figure 50: (a) 2'-Deoxyadenosine-5'-monophosphate. (b) 2'-Deoxycytidine-5'-monophosphate. (c) 2'-Deoxyguanosine 5'-monophosphate. (d) 2'-Deoxythymidine-5'-monophosphate. (Wasfi et al., 2020) © 2020 IOP.
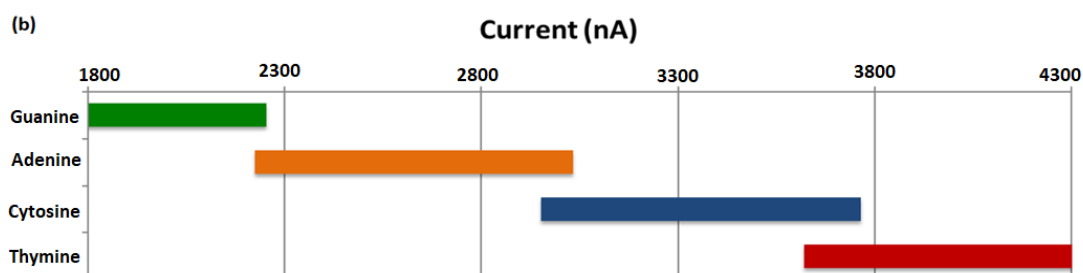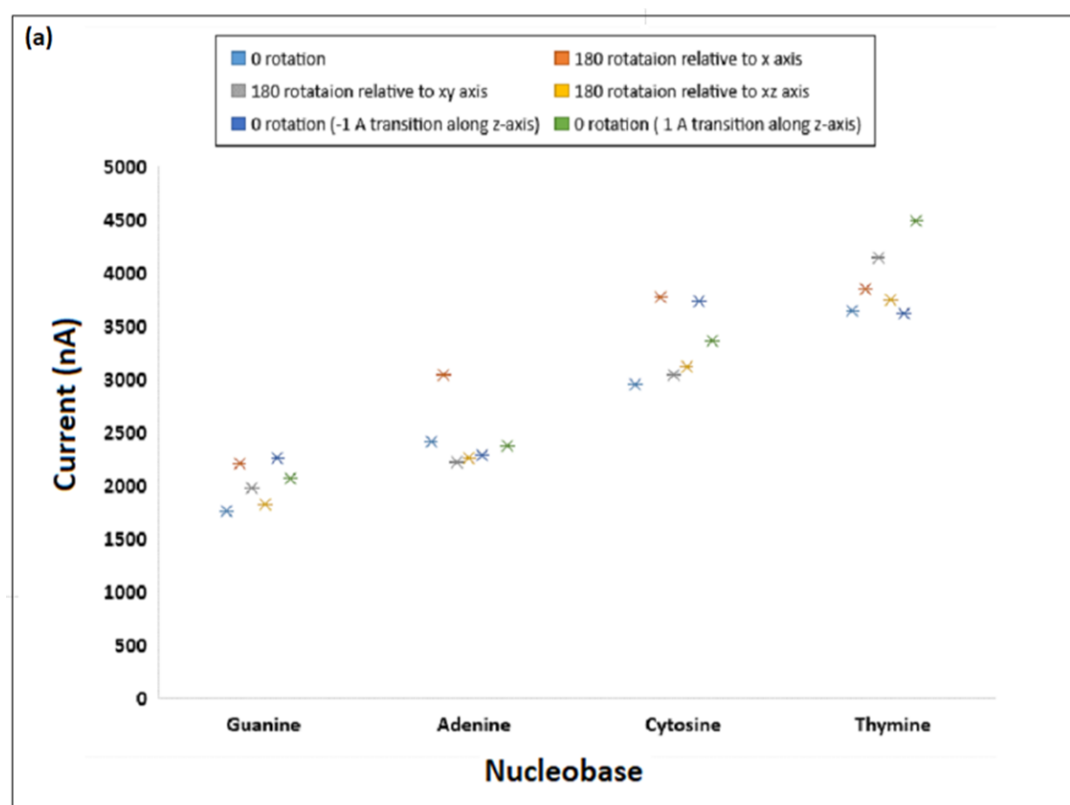
Figure 51: Current variations due to nucleobase various orientations and lateral translation. (a) Current difference due to nucleobase various orientations and lateral translation in the z-shaped field-effect transistor sensor nanopore. (b) Current ranges due to nucleobase various orientations and translation. Both figures are produced using 0.5V bias and 2V gate potential (Wasfi et al., 2020) © 2020 IOP.

Figure 52 displays the current signature for each DNA base for bare sensor and sensors with gold or silver nanoparticles. The low current in nanoparticle decorated z-shaped graphene nanoribbon sensor is predicted due to various reasons. Firstly, the silver and gold nanoparticles presence can work as charge scattering sites which reduce the device mobility. Secondly, the nanoparticles placement may lead to poor sp^2 carbon structure recovery. A critical point is that placing metal nanoparticles may result in degradation in charge transport properties of graphene sensors (Tjoa, Wei, Dravid, Mhaisalkar, & Mathews, 2011). Moreover, it is noticed that DNA bases detection current for the sensor with silver nanoparticles is less than the detection current with gold nanoparticles. The sensor with silver nanoparticles exhibits higher contact resistance than with gold nanoparticles on the applied voltage. The higher resistance of silver nanoparticles is probably due to the space charge field established by the trapped carriers. It is noticed that the sensor mobility with nanoparticles is less than the bare sensor mobility (Wasfi et al., 2020) © 2020 IOP.
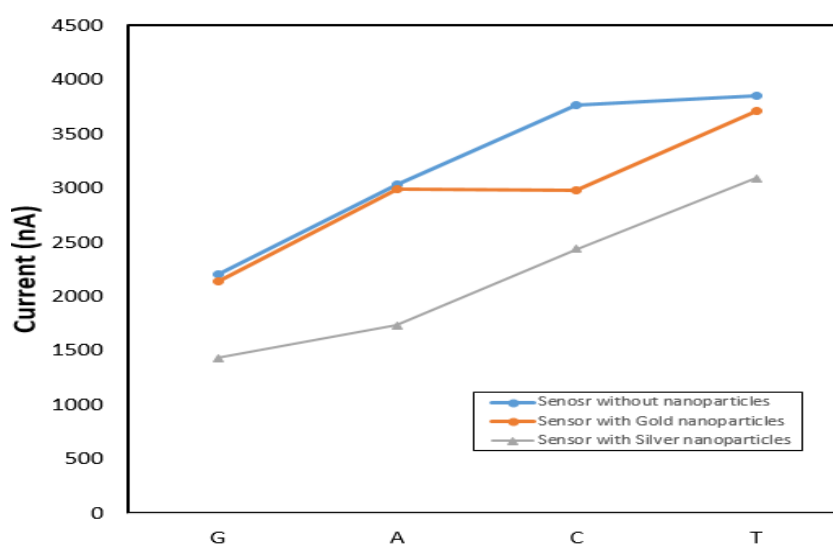
Figure 52: The room-temperature current of the z-shaped graphene nanoribbon sensor when each of the four DNA bases (A, C, G, T) is placed within the nanopore center bare and with gold and silver nanoparticles. (Wasfi et al., 2020) © 2020 IOP.

3.1.2.4 Dual Gate Field-Effect Transistor of Graphene Nanoribbon with a Nanopore

Each of the different types of DNA nucleobases inside the nanopore leads to a sole variation in the device current and transmission spectrum. The results of the dual-gate field-effect transistor of graphene nanoribbon with a nanopore (fourth sensor) translocation of DNA bases are as below.

3.1.2.4.1 Transmission Spectrum

The z-shaped graphene nanoribbon device transmission spectrum was calculated with 2, 2, 100 sampling point. The energy domain -2 to $2\,eV$ has 200 sampling points. For the Hückel basis set, the empirical potentials called Cerda. Carbon (graphite) (Cerdá & Soria, 2000) basis set is chosen for carbon, while Hoffman is chosen for the rest of the atoms (Narendar et al., 2018).

Figure 53 shows the zero bias transmission spectrum for the developed sensor of 1.01 nm pore with two types of pores based on the passivation of the edge carbon atoms: Hydrogen (H-pore) or Nitrogen (N-pore). The figure reveals low values of transmission spectrum within the energy range [-0.7, 1.1] eV, which is due to the band gap energy window within the AGNR channel. The number of transmission peaks produced by N-pore is more than those produced by H-pore. The N-pore transmission spectrum indicates higher sensor current than the H-pore sensor.
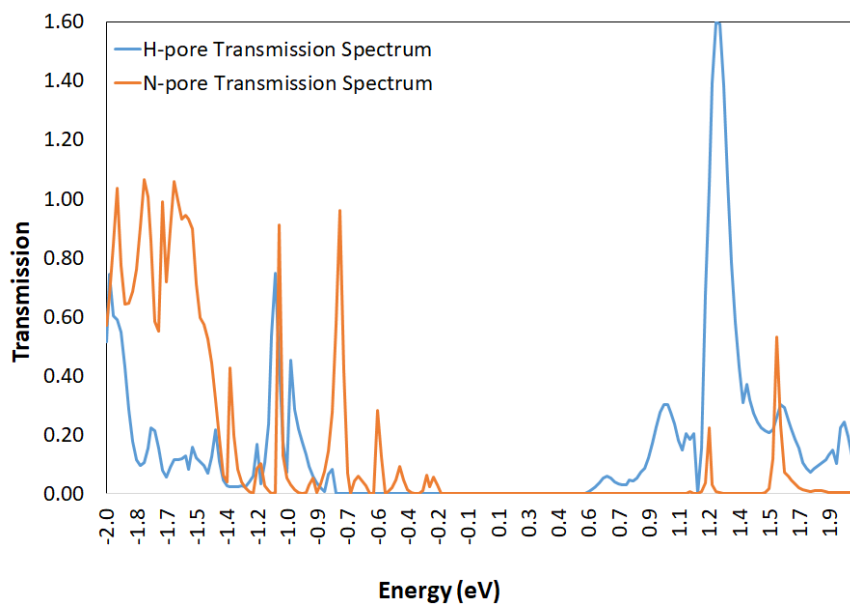
Figure 53: The bias transmission spectra at zero for z-shaped graphene nanoribbon device with an empty (H-pore) or (N-pore).
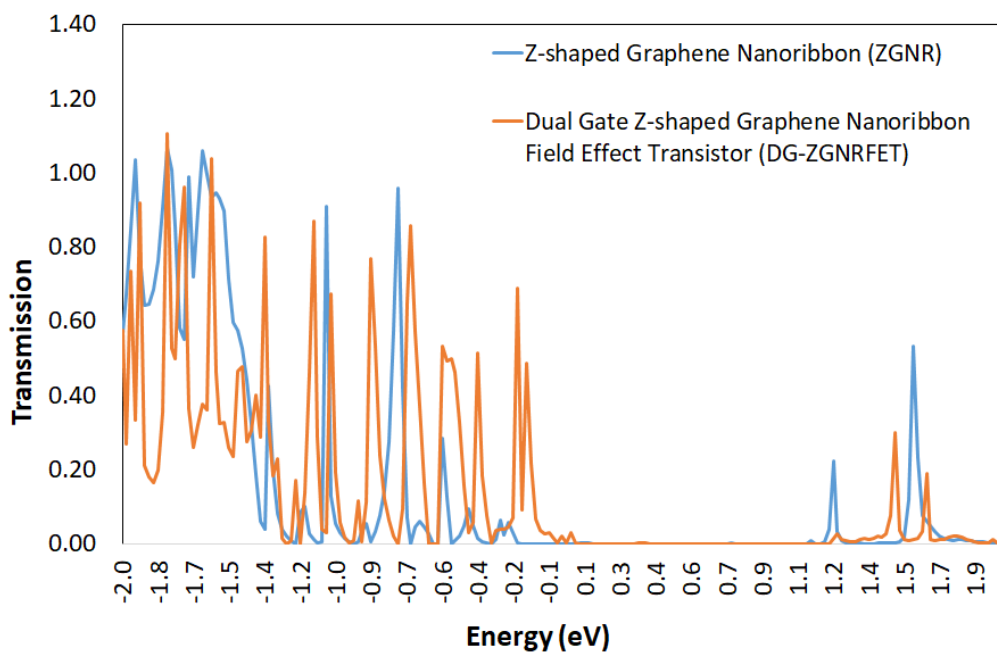
Figure 54: The bias transmission spectra at zero for both z-shaped graphene nanoribbon and dual gate z-shaped transistor with N-pore.

Figure 54 displays the zero bias transmission spectra for comparison between the z-shaped graphene nanoribbon and the DG-ZGNR-FET. The DG-ZGNR-FET has more transmission peaks with higher intensity than the z-shaped graphene nanoribbon which indicates higher sensitivity and higher current readings as compared with the zero bias transmission.

Figure 55 (a-d) displays the transmission spectra for A, G, T and C bases under a fixed bias voltage of 2.8 V (±1.4V on each source and drain). Figure 56 shows the structure of the four different types of DNA bases at 0° rotation. The structure of the rotated bases: A, T, G, and C is shown in Figure 57. Each DNA base is rotated at an angle of 180° with respect to the x-axis, xz-plane, and xy-plane.
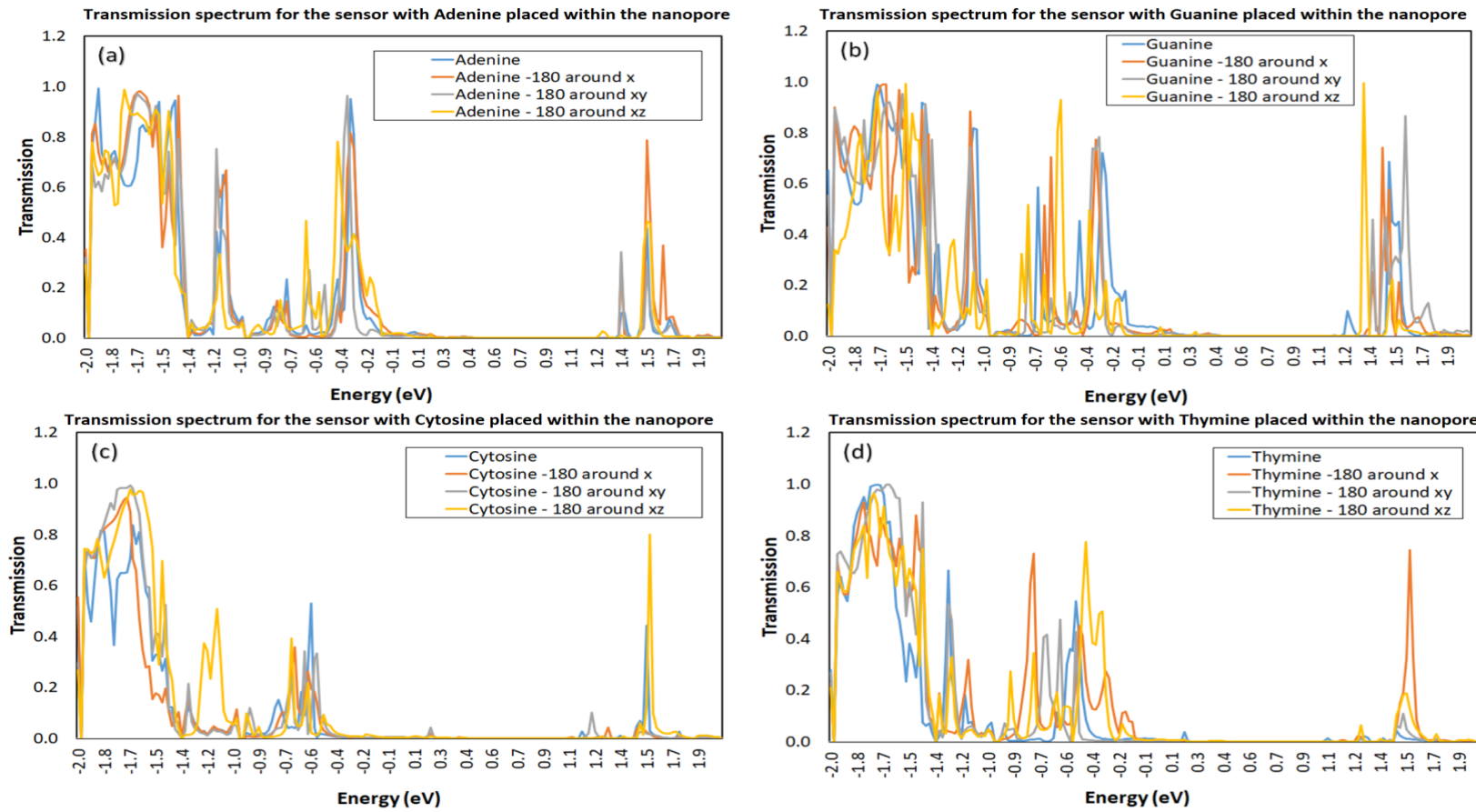
Figure 55: The transmission spectra for the different types of DNA nucleobases at a bias voltage of 2.8 V. The different colors represent the different orientations for each DNA base (Wasfi & Awwad, 2019b)© 2019 IEEE.
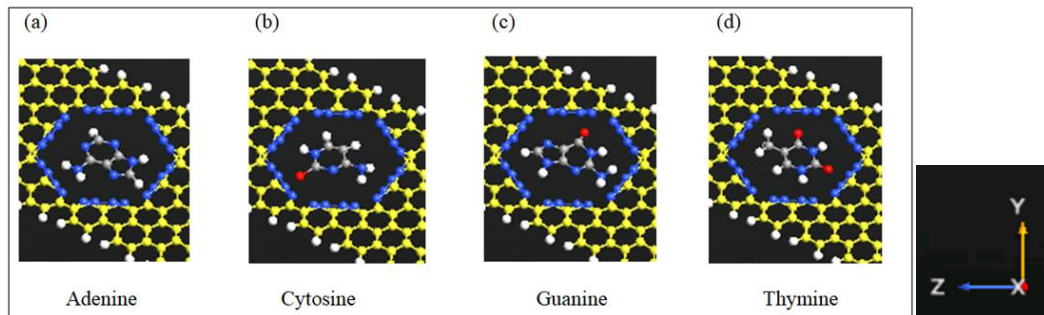
Figure 56: The structure of the nanopores with different types of DNA bases (A, G, C, and T) at 0° orientation. (Wasfi & Awwad, 2019b)© 2019 IEEE.
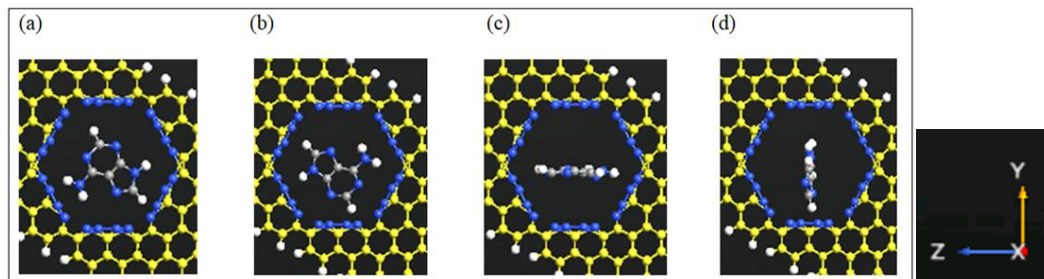
Figure 57: The structure of the nanopores with DNA bases. (a) Adenine is positioned at 0° angle within the pore. (b) Adenine is inclined at 180° angle with respect to the x-axis. (c) Adenine is inclined at 180° angle with respect to the xy-plane. (d) Adenine is inclined at 180° angle with respect to the xz-plane. (Wasfi & Awwad, 2019b)© 2019 IEEE.

3.1.2.4.2 Transverse Current

Figure 58 shows the z-shaped sensor transverse current for each base when placed inside the center of the H-pore or N-pore. Utilization of N-bond can improve the transverse current rate compared with H-bond. Therefore, N-pore can be utilized as an alternative to H-pore in order to improve the sensor sensitivity and to identify the DNA bases. Herein, N-bonds improve DNA bases and the device coupling which increases the transverse current magnitude. As a result, the current measurability and

detection are clearer and highly enhanced. Moreover, the read speed of DNA sequence is increased due to the high current, thus speed up the detection process.

Figure 59 displays the transverse current for the various types of DNA nucelobases in the nanopore of the two-terminal and four-terminal sensors. A 1 V gate potential was applied for each gate of the DG-ZGNR-FET sensor across the central region, and the voltage between the source and drain was fixed as +1.4 and −1.4 V, where the device functions as a field-effect transistor. The sensor with a gate voltage exhibits higher transverse current rates and thus higher sensitivity as compared with the case without gate.
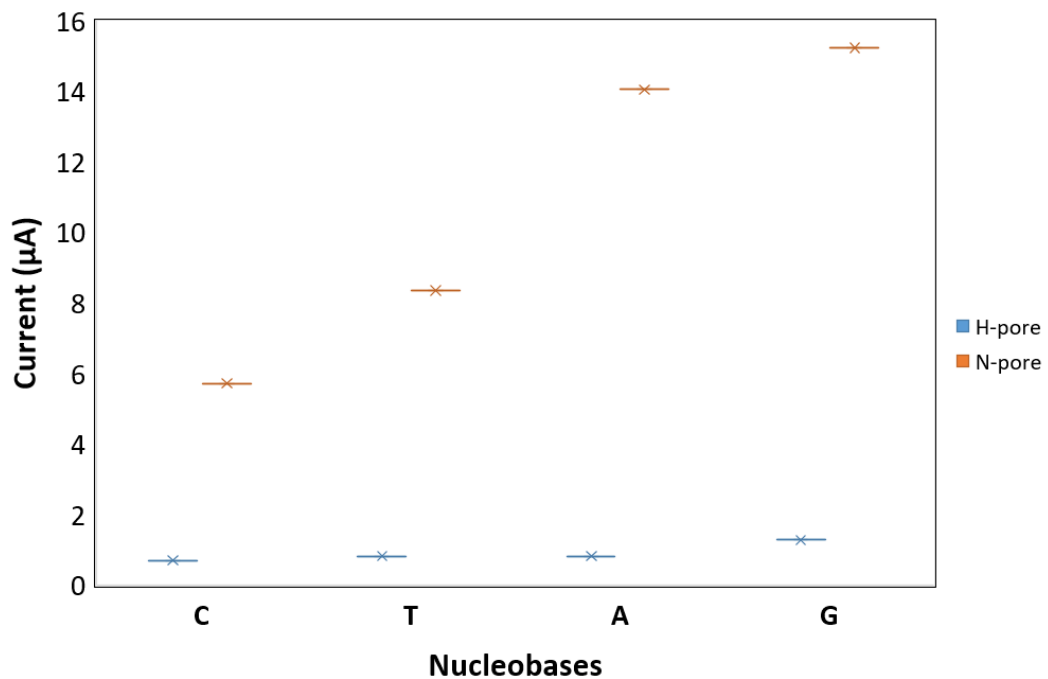
Figure 58: Current of the z-shaped device when each of the DNA nucleobases is placed into the middle of the N-pore or H-pore with ~1.01 nm diameter. (Wasfi & Awwad, 2019b)© 2019 IEEE.
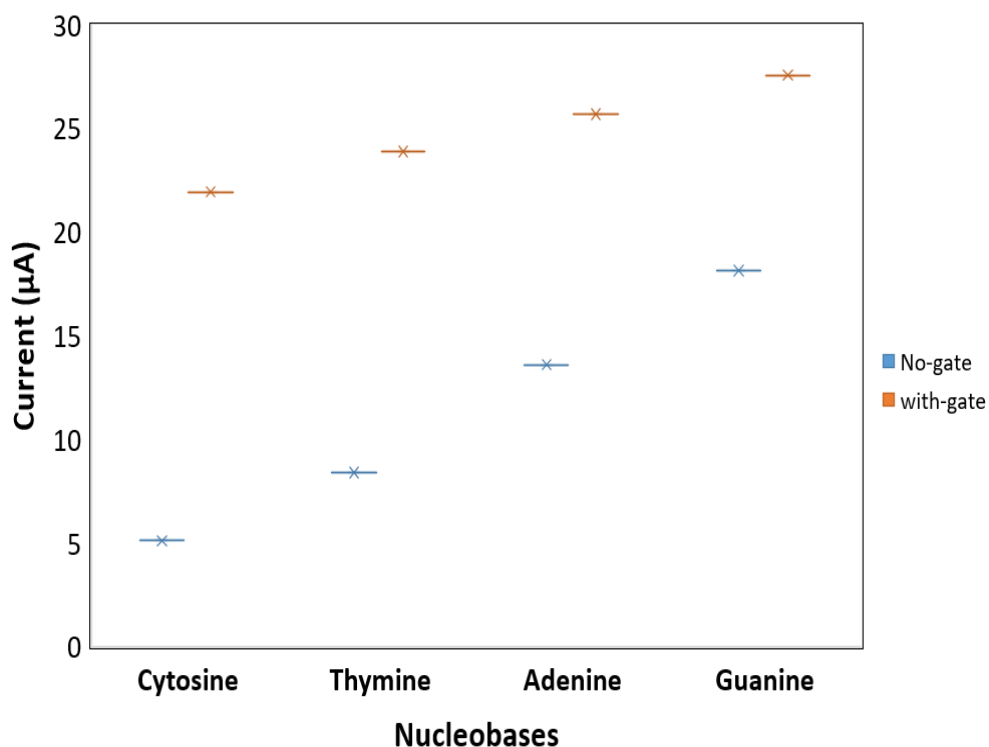
Figure 59: Current of the z-shaped device with and without gate voltage when each of the DNA nucleobases is positioned into the middle of the N-pore with ~1.01 nm diameter.

Figure 60 displays the possible current ranges when the nucleobases are rotated at 180° angle with respect to the x-axis, xy-plane, and xz-plane (shown in Figure 57 (a-d). The current fluctuations are because of the alterations of bases' geometry and orientations. Figure 61displays the current ranges because of each base rotation at 2.8 V bias within the N-pore sensor. The figure shows unique current signature for the different DNA bases positioned within the N-pore. It shows the intervals that have to be set as the current variations limits.

Graphene nanopore edge functionalization by either hydrogen or nitrogen modifies the sensor behavior. This work agrees with (Amorim, Rocha, & Scheicher, 2016; Leão de Souza, Amorim, Scopel, & Scheicher, 2019) where the nitrogen passivation of the nanopore and nanogap improves the sensitivity when compared to

hydrogen passivation. Moreover, the lowest to highest order of the DNA bases transmission and current is the same due to both types of passivation, but the transmission and current are higher with N-pore (Amorim et al., 2016; Leão de Souza et al., 2019). Moreover, it was noticed that the tunneling pore or gap is bridged in a better way with purine bases resulting in a higher current for purine bases in comparison to pyrimidine bases (Amorim et al., 2016). The overall transmittance is highly increased in nitrogen termination. In particular, the electrical current is larger and easier to detect due to N-functionalization. The sensor with N-pore has stronger interaction and better coupling between the DNA base and the sensor and this fact is because of the hybridization between the DNA bases and the states from the edge leading to higher charge transfer.

Theoretical work proved that N-terminated pores enhance the single biomolecule detection and makes the sensor highly sensitive (Al-Dirini, Hossain, Nirmalathas, & Skafidas, 2014; Al-Dirini et al., 2016; Wang et al., 2009).
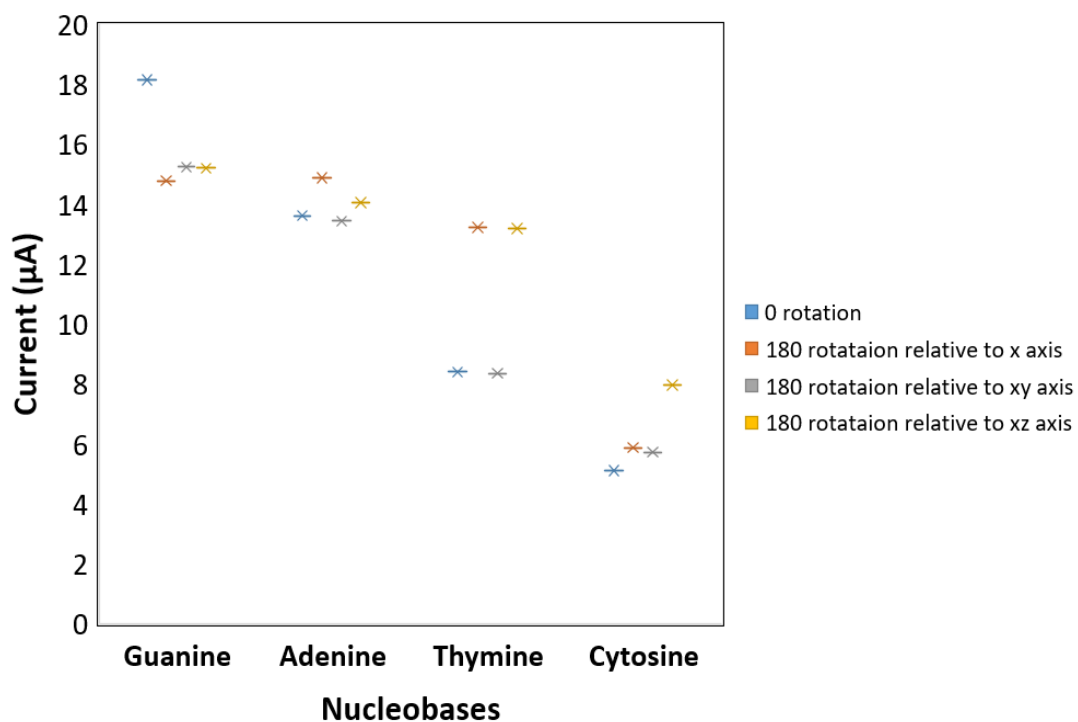
Figure 60: Current difference resulting from nucleobase rotation in the z-shaped device pore at 2.8 V bias. (Wasfi & Awwad, 2019b)© 2019 IEEE.
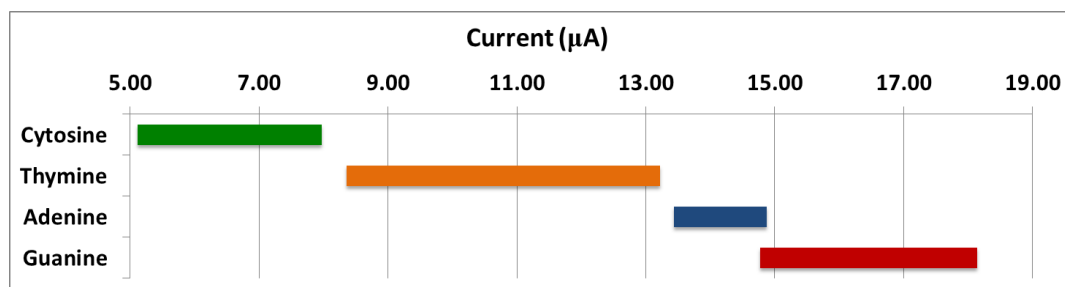
Figure 61: Current ranges resulting from base rotation at 2.8 V bias in the N-pore. (Wasfi & Awwad, 2019b)© 2019 IEEE.

3.2 Experimental Results

This section summarizes the experimental results, observations, and measurements.

3.2.1 Results of FET Sensors Based on Graphite Oxide Decorated with Trimetallic Nanoclusters

The FET sensor based on Graphite Oxide was utilized to detect various concentrations of DNA. This sensor identifies various elements by measuring the variation in the electrical signals.

3.2.1.1 Raman Spectrum

Raman spectroscopy is used to investigate electronic and structural features of materials. The D-band provides information about defects while the G-band provides information about saturated carbon structure. Figure 63 was generated by applying 532 nm laser radiation and 20 % of the ND Filter. Figure 63 shows that the D-band was observed around 1300 - 1400 cm^{-1} which shows the structural defects, while the G-band was observed around 1550 - 1630 cm^{-1} which indicates the stacked structures.

Figure 63 shows the Raman spectra of Graphite Oxide sample displayed in Figure 62 (a) and the Raman spectra of Graphite Oxide decorated with composite nanoclusters of gold, silver, and platinum displayed in Figure 62 (b). Metallic nanoclusters enhance Raman spectrum (Irene Ling, Si Fan, & Jian Pang, 2015; Moskovits, 1985). Thus, Figure 63 shows that the Raman spectra of GO with composite nanoclusters has higher counts than the Raman spectra of GO sample. This difference is due to the intrinsic characteristics of metallic nanoclusters leading to different ionization energies (Irene Ling et al., 2015).
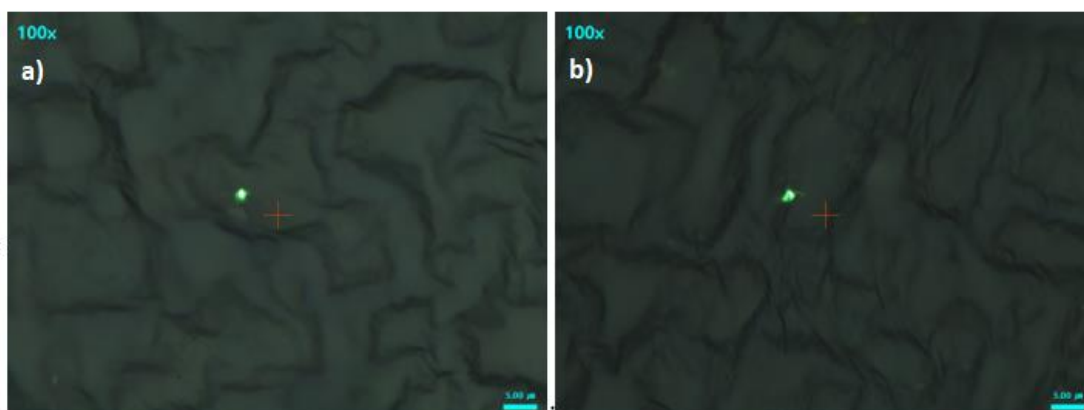
Figure 62: Samples for Raman Spectra. (a) Sample of Graphite Oxide. (b) Sample of Graphite Oxide with composite metallic nanoclusters of gold, silver, and platinum.
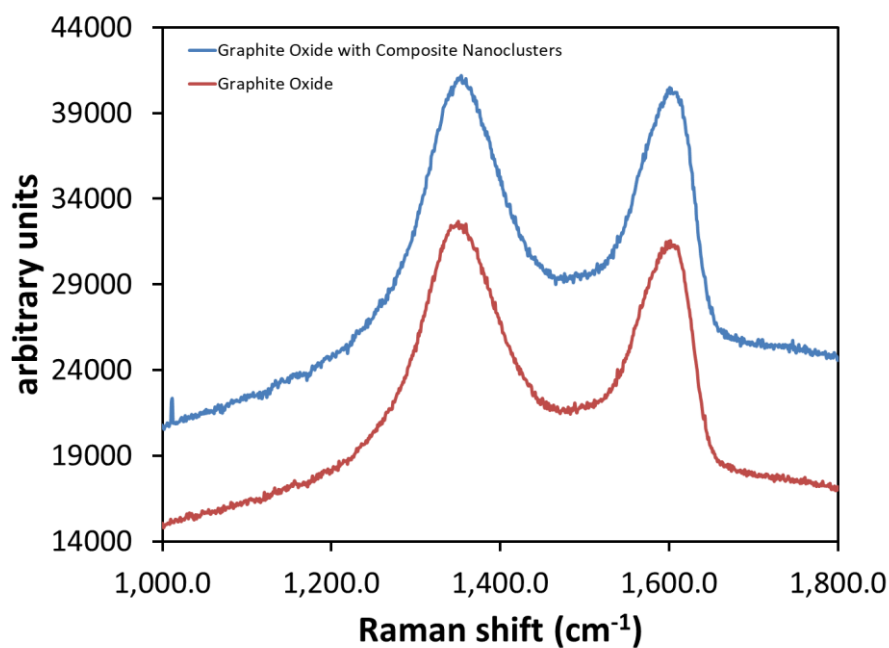
Figure 63: Raman spectra of Graphite Oxide and Graphite Oxide with composites metallic nanocluster of gold, silver, and platinum under the radiation of 532 nm laser line.

3.2.1.2 Ultraviolet–Visible Spectroscopy

Ultraviolet–Visible Spectroscopy was used to identify the graphite oxide peak. Figure 64 displays the ultraviolet-visible spectra of graphite oxide. The graphite oxide has an absorption peak at 230 nm which is attributed to the $\pi - \pi^*$ plasmon peak.
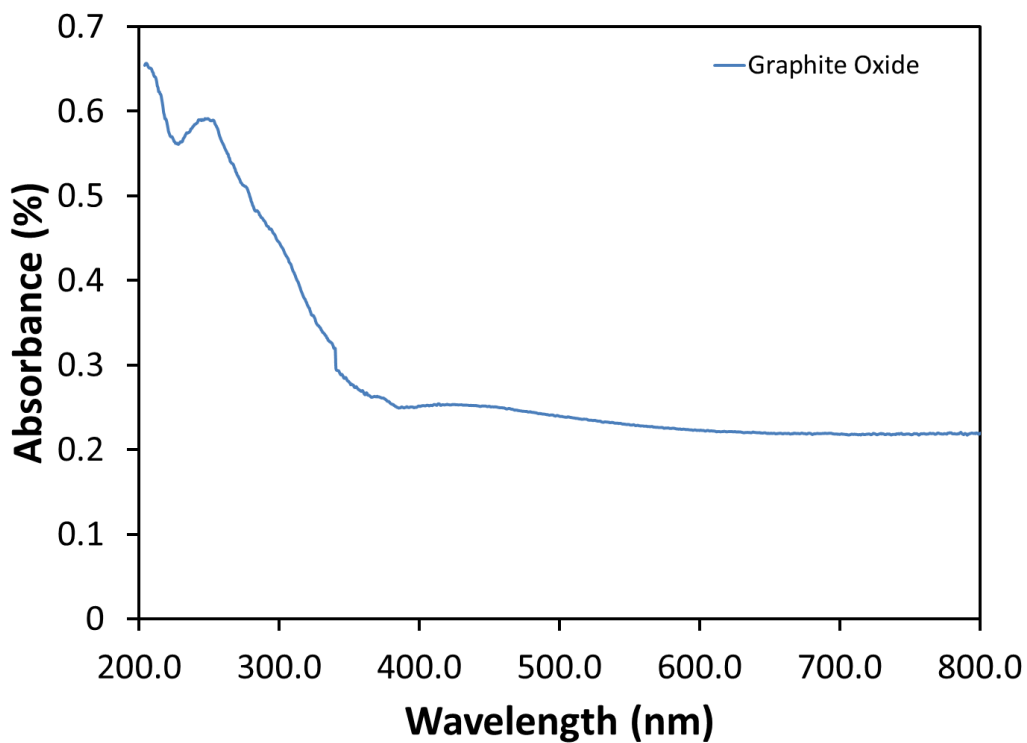
Figure 64: UV-vis spectra of Graphite Oxide.

3.2.1.3 Size Distribution of Nanoclusters

The nanocluster size distribution is displayed in Figure 65 for a sputtering discharge power of 10.8 W, inert gas flow rate of 40 sccm, and aggregation length of 70 mm. Figure 65 shows the size distribution for the trimetallic nanocluster of silver, gold, and platinum as measured using the QMF where the average diameter size is 36-37 Å.
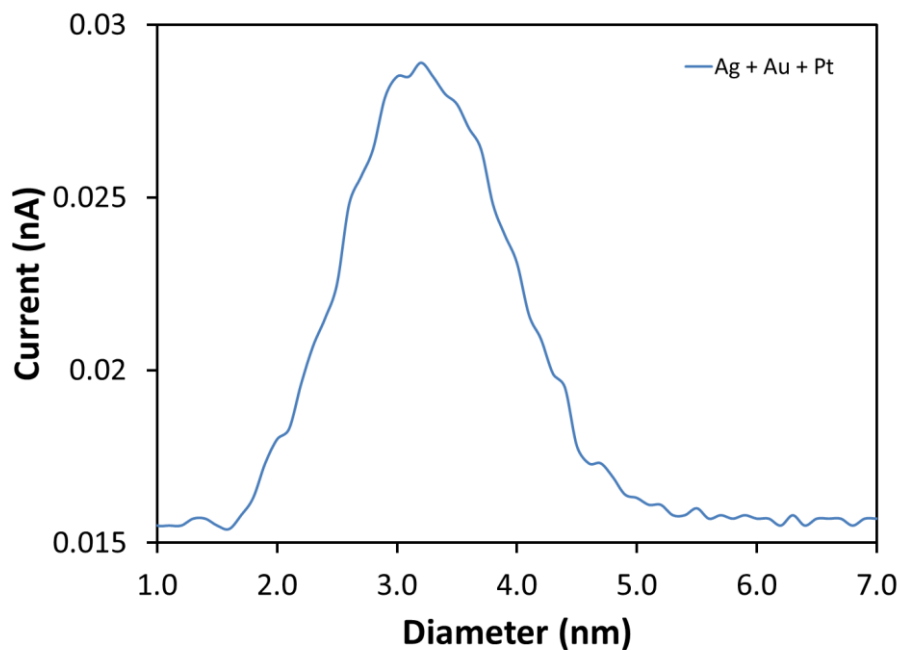
Figure 65: Size distribution of composite trimetallic (Au, Ag, and Pt) nanoclusters measured using QMF where the average diameter size is 3.64 ± 0.18 nm.

3.2.1.4 Nanoclusters Characterization

Figure 66 shows TEM image of trimetallic nanoclusters of gold, silver, and platinum which were fabricated at aggregation length L = 70 mm with argon flow rate Ar= 40 sccm. The nanoclusters are singular or agglomerations of nanoclusters. The dark spheres refer to the agglomerations of nanoclusters.

Figure 66: TEM image of trimetallic nanoclusters of gold, silver, and platinum.

Commercial glass slides were placed on the sample holder with the sensor while the nanoclusters were being deposited to confirm the existence and composition of the nanoclusters. Figure 67 shows the EDS spectrum which confirms the existence of the composite nanoclusters of gold, silver, and platinum. The figure displays the amount of mass percentage for each of the different nanoclusters where the mass percentage for silver was 0.54%, while the mass percentage for gold was 1.02%, and the mass percentage for platinum was 0.21%. The difference in atomic percentage between the nanoclusters and the target can be assigned to the variation in sputtering yield of the various elements. The existence of other elements such as carbon, silicon, and oxygen is because the composite nanoclusters were sputtered on glass substrates for the EDS analysis. The various atoms with the nanoclusters (Ag, Au, and Pt) have high affinity to DNA which enhances the sensor performance (Song, Lu, Yang, & Zheng, 2005).

Formula	mass%	Atom%	Sigma	Net	K ratio	Line
O	47.70	61.23	0.66	2267	0.0032097	K
Na	9.76	8.72	0.52	703	0.0008968	K
Si	40.78	29.82	1.25	2761	0.0045426	K
Ag*	0.54	0.10	0.69	12	0.0000423	L
Pt*	0.21	0.02	1.14	5	0.0000122	M
Au*	1.02	0.11	1.16	21	0.0000594	M
Total	100.00	100.00				
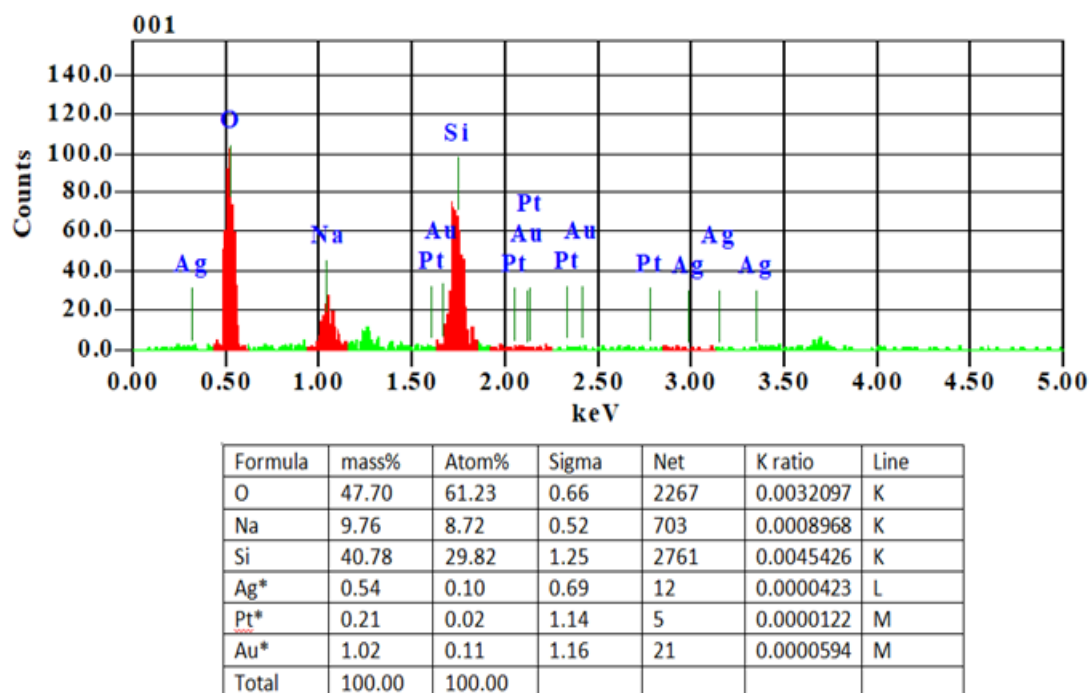
Figure 67: EDS spectrum of composite nanoclusters. The composite nanoclusters consist of silver, gold, and platinum with mass percentage of 0.54% for silver, 1.02% for gold, and 0.21% for platinum. The existence of other elements such as calcium (Ca), sodium (Na), silicon (Si), and Oxygen (O) is due to the glass substrate.

3.2.1.5 FET Characteristics

The sensor electrical characteristics were measured at room temperature. Figure 68 shows the drain current (I_d) versus drain–source voltage (V_{ds}) characteristics for the sensor without nanoclusters and with nanoclusters. The V_{ds} varies from -0.6 V to 0.6 V at room temperature. The figure displays a linear dependence between I_d and V_{ds} where I_d increases with increasing V_{ds}. The fabricated sensor has n-type transistor behavior where applying a positive gate voltage leads to an increment of the conducting electrons within the transistor channel which improves the channel conductivity and increases the drain current. On the other hand, a non-linear curve is observed for the sensor based on graphite oxide only, due to the graphite oxide channel that is considered semiconducting material (Kang, Kulkarni, Stankovich, Ruoff, &

Baik, 2009). The addition of metallic nanoclusters resulted in higher drain current at the same applied voltage because trimetallic nanoclusters of gold, silver and platinum exhibit higher conductivity as compared with graphite oxide.
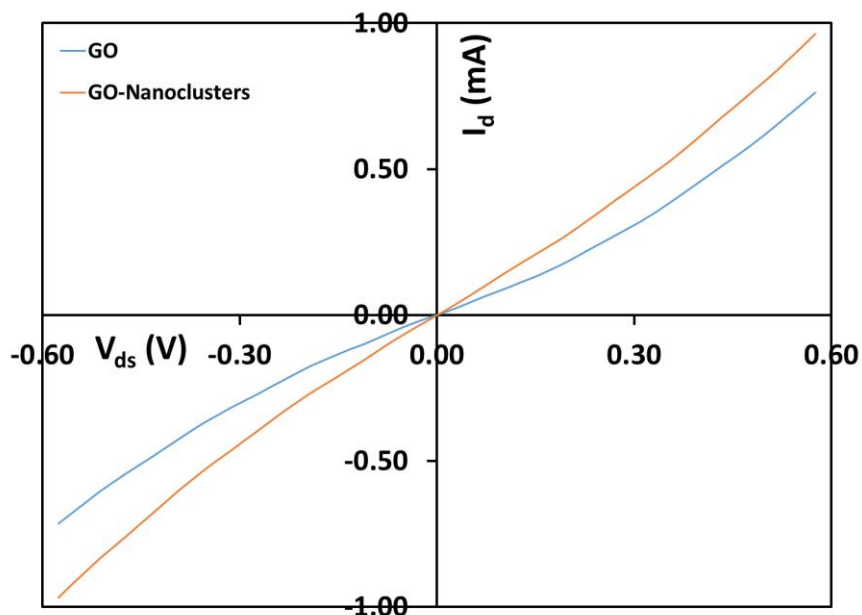
Figure 68: Id-Vds characteristics profile for both GO sensors: with and without trimetallic nanoclusters.

3.2.1.6 Sensor Testing

The sensor was tested for different concentrations of DNA. Figure 69 (a) shows the variation in the current (at V_{ds}= 0.2 V and V_g= 0 V) when the graphite oxide channel sensor was exposed to 2 µL of DNA of 50 ng/µL concentration. The sensor current started at I_{max} = 3.76 x 10^{-4} A and when the DNA solution was dropped on the sensor channel at time t= 34 s, the current I_d drop was observed and reached I_{min} = 3.55 x 10^{-4} A. The variation in the current I_d was used to evaluate the sensor sensitivity since the values of I_{max} and I_{min} are device dependent. The change in the current was calculated as $\Delta I = I_{max} - I_{min}$. Figure 69 (b) shows the current variation for the sensor decorated with the trimetallic nanoclusters. The sensor current started at I_{max} = 4.07 x 10^{-4} A and

when the DNA solution was dropped on the sensor channel at time t= 34 s, the current I_d drop was observed and reached $I_{min} = 3.76$ x 10^{-4} A. It was noticed that the sensor starting current with nanoclusters is higher than the sensor starting current without nanoclusters and ΔI for the sensor with nanoclusters was 31 µA while ΔI for the sensor without nanoclusters was 21 µA. This indicates that sensor sensitivity is improved after adding the nanoclusters.

(a)
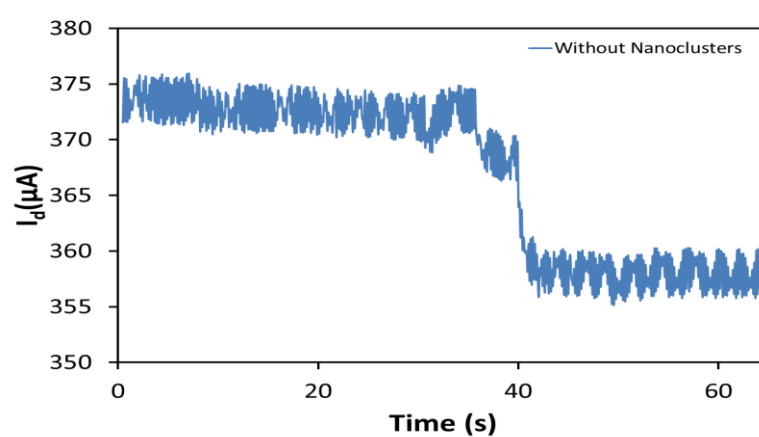
(b)
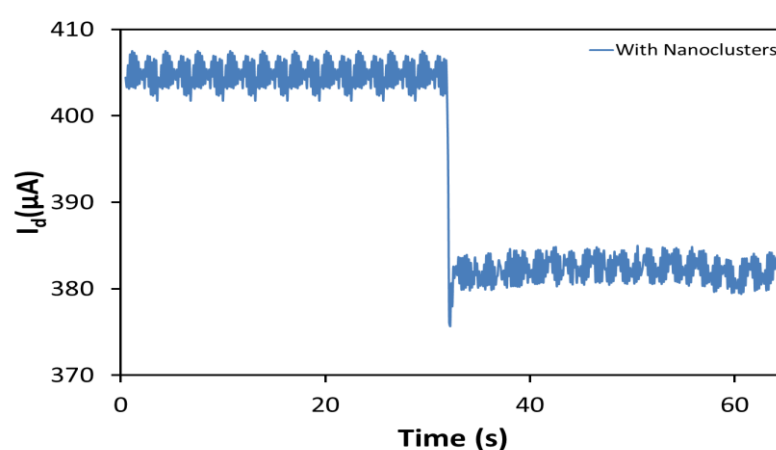
Figure 69: Variation in the drain current due to a 2 µL drop of 50 ng/µL of DNA for (a) sensor without nanoclusters, and (b) sensor with alloy nanoclusters.

The drop in the drain current of graphite oxide sensor after placing DNA droplet is due to the DNA negatively charged triphosphate group which induces excess hole carriers (Ohno, Okamoto, Maehashi, & Matsumoto, 2013; Tian et al., 2018; Xu, Zhan, et al., 2017). Several studies reported that graphite oxide or graphene adsorbs the DNA molecules through π-π interaction (Dong, Shi, Huang, Chen, & Li, 2010; Mohanty & Berry, 2008; Wang et al., 2011; Wen et al., 2010; Yin et al., 2011). The adsorption of the DNA ions (negative charge) by the channel of graphite oxide or graphite oxide with nanoclusters reduces the current. The more significant reduction of drain current for the sensor decorated with nanoclusters confirms the more adsorption of DNA (Yin et al., 2011). The holes concentration increases compared to the electrons where the holes trap the electrons leading to an increment of the sensor electrical resistance which results in decreasing the I_d current. These results are in good agreement with other people work (Ohno et al., 2013; Tang et al., 2006; Tian et al., 2018; Xu, Zhan, et al., 2017). The difference in I_d was more when the sensor was decorated with the trimetallic nanoclusters since these metals has high affinity to DNA (Song et al., 2005; Yin et al., 2011).

The variation of the electrical current was measured for both sensors due to placing various concentration of DNA solution. Figure 70 shows the variation in the current due to different concentrations of DNA which ranges from 5 ng/µL to 100 ng/µL. The figure depicts that the ΔI increases due to higher concentrations of DNA in both sensors. Also, the figure indicates that GO-nanoclusters sensor results in higher sensitivity for the various concentrations of DNA. This is due to the existence of composite trimetallic nanoclusters which have high affinity to DNA, which causes more adsorption and interaction for the DNA with the sensor. Moreover, all three

metals gold, silver, and platinum are good conductors which increase the current signal. The physical and chemical properties of the trimetallic composite nanoclusters enhance the absorption and the interaction of the materials on the surface of the sensor such as DNA. These observations are in good agreement with the simulation results illustrated in Section 3.1.1.
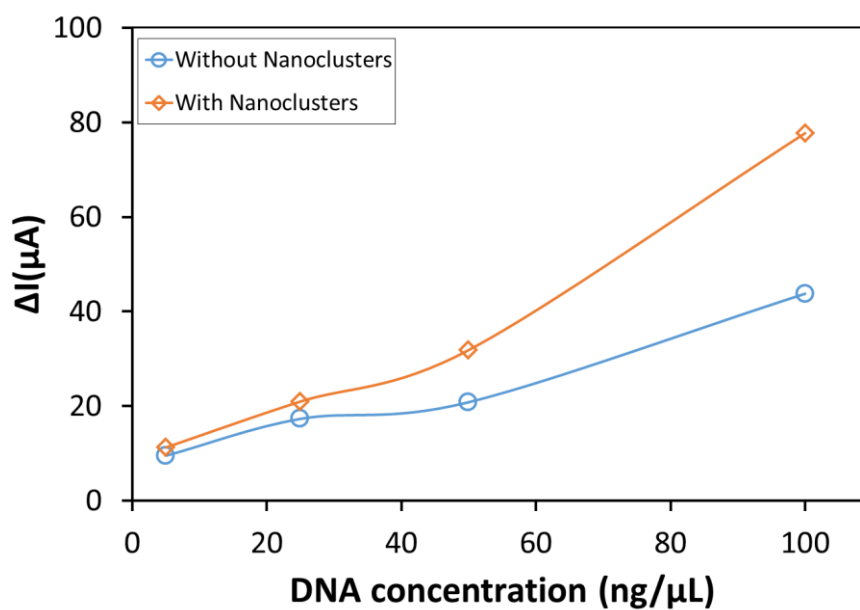
Figure 70: variations in the electrical drain current due to different concentrations of DNA.

Chapter 4: Discussion

This chapter describes and interprets the findings and the significance of this research work. Each one of the developed sensors' findings is discussed, interpreted and compared to previous work.

4.1 FET Sensors Based on Graphite Oxide Decorated with Trimetallic Nanoclusters

This section discusses the FET sensor based on graphite oxide and decorated with trimetallic nanoclusters. For this sensor, the findings are illustrated in Section 3.1.1 and Section 3.2.1 where the experimental performance is confirmed by simulation. Both simulation and experimental results reveal a promising sensor for real time DNA detection. The results generated from simulation and experiment indicates that exposing the sensor channel to various concentrations of DNA decreases the current which is explained due to adsorption difference of DNA molecules by the bare graphite oxide channel and the graphite oxide channel with trimetallic nanoclusters. The addition of DNA to the channel increases the holes concentration which traps the electrons and increases the resistance leading to current decrement (Tian et al., 2018). The current decrease due to DNA adsorption results are in good agreement with previous research work that confirmed increasing the holes concentration upon adsorption of DNA (Dong et al., 2010; Tang et al., 2006; Yin et al., 2011). Also, the current variation increases due to higher concentrations of DNA which indicates the higher adsorption due to higher concentration. This work results agree with previous work where the current decreases due to the increment of the DNA concentration (Dong et al., 2010; Yin et al., 2011). Moreover, both simulation and experiment indicate higher sensitivity due to the presence of trimetallic nanoclusters on the sensor

channel as compared with the bare channel. The higher sensitivity was due to the high affinity to DNA of the trimetallic nanoclusters as explained by pervious research work (Dong et al., 2010; Song et al., 2005; Yadav et al., 2018). The various metal ions show diverse DNA binding affinities. Platinum ions have high affinity to DNA (Song et al., 2005). The adsorption intensity of DNA increases due to the addition of gold or silver ions. The increment in the absorptivity of DNA is due to the binding of gold or silver ion to the DNA phosphate group and leaving the pyrimidine and purine bases of DNA exposed (Song et al., 2005). The DNA binding constant to gold is higher than that to platinum and silver (Song et al., 2005).

4.2 Z-shaped Graphene Nanoribbon with a Nanopore

The z-shaped graphene nanoribbon with a nanopore sensor findings are discussed here. Intensive studies have been performed on transverse current of various electrode-nucleotide coupling (Krems, Zwolak, Pershin, & Di Ventra, 2009; Lagerqvist, Zwolak, & Di Ventra, 2007; Meunier & Krstic, 2008). However, most of these studies faced the issue of interference between adjacent nucleobases since DNA bases length is $\approx$ 0.32 nm which is much less than the thickness of most used electrodes' material such as gold. This makes it difficult to differentiate the neighboring bases (He et al., 2010; Lagerqvist, Zwolak, & Di Ventra, 2006). An alternative technique is the transverse electronic based sensors with a nanogap (Postma, 2010). This sensor is based on graphene, which is one atom thick, where the nanopore thickness is similar to the DNA nucleobases dimensions. Moreover, single and multilayer graphene experiments based on measuring the vertical ionic current of passing DNA, didn't provide adequate resolution to identify the different nucleobases (Branton et al., 2008; Healy, Schiedt, & Morrison, 2008) Various experimental (Huang

et al., 2010; Tsutsui, Taniguchi, Yokota, & Kawai, 2010) and theoretical (Chen, Rungger, Pemmaraju, Schwingenschlögl, & Sanvito, 2012; Zwolak & Di Ventra, 2007) studies on nanogaps were conducted, but resulted in very small current of picoampere (Prasongkit et al., 2011). First-principle studies based on two metallic graphene nanoribbon hosting a nanogap resulted in current variations for the different nucleobases inside the gap, a major drawback was the low conductance (He et al., 2011). Moreover, a nanogap may permit several DNA bases to translocate through the gap simultaneously that results in signal interference problem. As nanopore has low dimension size in contrast with a nanogap, thus, this sensor did avoid the simultaneous DNA sequence issue. Moreover, the results in (McFarland et al., 2015) showed that at 0.5 V purine bases (Adenin and Guanine) have less current than pyrimidine bases (Cytosine and Thymine) which is consistent with the results of this sensor. On the other hand, at 1 V purine bases have more current than pyrimidine bases (Lagerqvist et al., 2006; Prasongkit et al., 2011).

Due to the different electronic and chemical structure of the four nucleobases, each one of them has a unique signature. The main objective of this sensor was to find the relative current for each nucleobase where a unique electronic signature was found for each base to create a DNA electronic map. The electronic and chemical structure effect of the DNA bases in charge transport was studied. Also, it was found that nucleotides' orientations affect the electronic signature. This sensor was able to discriminate the four bases by providing a unique current and conductance range for each base. This sensor suggests that graphene-based sensor promise successful and fast method for DNA sequencing. It provides strong motivation for the development of a new class of nanopore sequencing devices.

4.3 Z-shaped Graphene Nanoribbon with a Nanogap

The second sensor is interpreted here. NEGF+DFT were used to generate the transmission spectrum and transverse current as a function of voltage bias for Adenine (A), Cytosine (C), Guanine (G), and Thymine (T) translocating through the sensor nanogap. Through the analysis of the bases current, it was found that DNA bases can be identified at 2 V bias voltage. The N-nanogap enhanced the current and sensitivity due to the improved coupling between the nanogap and the DNA bases which is consistent with previous work (Saha et al., 2012).

Graphene nanogap techniques have the potential to detect DNA base sequence, where a single stranded DNA (ssDNA) passes through a nanogap in a conductive material and the variations in the electronic properties such as conductance can be utilized to detect the DNA bases (Prasongkit et al., 2011). The main idea is that the DNA bases passing through a nanogap in a solid state membrane will modify the tunneling current passing through the nanogap resulting in unique signature for the four DNA bases (Lagerqvist et al., 2006). But, this technique faces the problem of interference of adjacent bases if they are in the nanogap simultaneously. Moreover, a main drawback of this method is the low current which makes it difficult to read and detect the signal (Prasongkit et al., 2011). (Wasfi & Awwad, 2019a)© 2019 IEEE.

4.4 Z-shaped Graphene Nanoribbon Field-Effect Transistor Decorated with Nanoparticles

Theoretical studies to enhance the current across nanogaps (Postma, 2010; Tsutsui et al., 2010) or nanopores (Nelson et al., 2010; Qiu et al., 2014; Wasfi et al., 2019) offer moderate improvement. Moreover, applying high bias to obtain high current signal may lead to DNA backbone attraction, or breakdown the sensor at high

electric field. Unlike other recent sensors based on transverse electronic properties which use small current across a nanopore or a nanogap resulting in low signal, the third sensor enhances electrical current results from nanoampere to microampere (Wasfi et al., 2019) thus makes it easier to detect, measure, and read. Placing a DNA base within the pore affects the charge density resulting in a unique current for each base. This sensor provides high readable currents when small bias voltage is applied. This may remove the need to reduce the DNA translocation speed since the speed to measure the current may be high which reduces the Brownian fluctuations in blurring the signal. The present sensors, bare and decorated with nanoparticles, exhibit higher sensitivity in comparison with the previous work (Wasfi et al., 2019). It was found that the bare sensor has the highest sensitivity for DNA bases detection and outperforms the ones decorated with gold and silver nanoparticles. Moreover, the sensor decorated with gold nanoparticles has higher sensitivity than the one decorated with silver nanoparticles. The current difference was due to the variation in the sensors mobility where the bare sensor has the highest mobility, then the sensor with gold nanoparticles, and the least mobility was for the sensor with silver nanoparticles.

Previous studies (Avdoshenko et al., 2013) showed that although the signal of undoped ZGNRs can be influenced by the DNA existence within the pore, it is still hard to differentiate between the different DNA bases. Adding a gate terminal can improve the results by shifting the Fermi energy from the charge neutrality point. Both nanogap and nanopore based sensors lose their efficiency in distinguishing the DNA bases if their sizes increase (Chen et al., 2012). The current z-shaped FET nanopore diameter is 10.1 Å which is effective to identify the different DNA bases. The utilized nanopore diameter is comparable to the nanogap diameter (11 Å) used by Scheicher et

al (He et al., 2011). Moreover, the sensor nanopore edge carbon atoms were passivated with hydrogen which reduces the DNA translocation speed and enhance the measurement accuracy for DNA sequencing (He et al., 2011). Hydrogen prevents the DNA bases from bonding with the graphene membrane and the nanopore. The present observations are in a good agreement with McFarland et al. (McFarland et al., 2015) and the previous work (Wasfi et al., 2019) where the results indicate that the pyrimidine bases within the pore result in higher current than purine bases at 0.5 V bias voltage. Each DNA base has its unique chemical and electronic structure that result in its unique current signature (Wasfi et al., 2020) © 2020 IOP.

4.5 Dual Gate Z-shaped Graphene Nanoribbon Field-Effect Transistor

Moderate improvements were offered by various theoretical studies to enhance the electrical current of DNA in nanogaps (He et al., 2011; Postma, 2010; Tsutsui et al., 2010) and nanopores (Nelson et al., 2010; Qiu et al., 2014; Wasfi et al., 2019). The fourth sensor is enhanced by using nitrogen instead of hydrogen to passivate the edge carbon atoms. The edge termination of graphene nanoribbons by nitrogen is noticed to be rich of electrons leading to n-type transistor behavior (Kienle, Bevan, et al., 2006; Kienle, Cerda, & Ghosh, 2006). The edge structure and chemical termination is critical to get the desired device characteristics. It is noticed that nitrogen passivated graphene pore sensors are very sensitive to intramolecular electrostatics (Al-Dirini et al., 2016). Previous work (Al-Dirini et al., 2014) confirms the improved sensitivity of nitrogen passivation in comparison to hydrogen passivation. The transverse current magnitude of the sensor was enhanced since the nitrogen bonds enhance the coupling between the sensor and the DNA bases. De Souza et al. designed a novel sensor using a hybrid sheet of graphene and hexagonal boron nitride with a nanopore to distinguish among

the different DNA bases where each DNA base with distinct dipole modifies that charge uniquely and results in a unique current (de Souza, Amorim, Scopel, & Scheicher, 2017). His work showed significant mechanism to sense DNA that relies on shifting the chemical potential of the sensor by applying a specific gate potential (de Souza et al., 2017). The sensor sensitivity is associated with the gate potential value and the applied bias voltage (de Souza et al., 2017; Leão de Souza et al., 2019; Pandey, 2018). Gate potential controls the local current path within the sensor (Leão de Souza et al., 2019). The results of the fourth sensor indicate that the designed sensor is required to be set to specific gate potential and bias voltage to get unique signature for the four DNA bases with high sensitivity. In the designed z-shaped sensor, the optimal results were generated when the dual gate is biased at 1 V each side and the bias potential is fixed among the two electrodes (+1.4 and −1.4 eV). Optimal results were generated based on the gate voltage and biased voltage that results in unique signature for the DNA bases without interference among there signals.

Moreover, adding a gate and applying a gate voltage to the z-shaped nanoribbon improves the sensor sensitivity and gives higher transverse current by shifting the Fermi energy towards the conduction band from the charge neutrality point. The gate electrode was placed very close to the semiconducting channel so that the applied electric charge affects the channel. The gate can control the carriers flow (holes or electrons) passing between source and drain. Applying a gate voltage increases the number of carriers within the semiconducting channel, which leads to higher current between source and drain. The utilization of N-pore and adding a gate terminal makes it feasible to measure, detect, and read the electrical properties of DNA

bases. Each DNA base affects the charge density in a unique way resulting in a significant electronic signature.

To steer a string of DNA through the nanopore or nanogap to acquire the experimental measurements, a nanotube microfluidic channel can be used. Moreover, intrinsic stepwise translocation for single stranded DNA (ssDNA) through a graphene pore can be used to improve the signal readings to identify the DNA nucleotides (Luan et al., 2010; Luan et al., 2012; Qiu, Sarathy, Leburton, & Schulten, 2015; Qiu, Sarathy, Leburton, & Schulten, 2016). The stepwise translocation can be accomplished by stretching the ssDNA mechanically while passing through the graphene pore (Qiu et al., 2015; Qiu et al., 2016). Qiu et al. found that ssDNA stepwise motion can be accomplished and helps to accurately identify the DNA nucleotides' passing through graphene pore. A harmonic spring was moved at a fixed velocity while the other end was attached to all phosphorus atoms which helps in preventing the tension between neighboring nucleotides (Qiu et al., 2015). The force applied to the spring varies due to the adhesive interaction among the DNA bases and graphene membrane. Moreover, mechanical stretching of DNA can prevent backward movement of DNA.

Chapter 5: Conclusion

In this work, various graphene-based sensors were designed, developed, studied, and tested by simulation for the purpose of nucleic acids detection.

The first aim of this research was to detect various concentrations of DNA using graphene-based sensors which were fabricated based on a Field-Effect Transistor (FET) structure on Si/SiO$_2$ wafer. The channel material was either bare graphite oxide or graphite oxide decorated with trimetallic nanoclusters. The two source and drain electrodes were made by thermal evaporation of gold metal (Au). Trimetallic composite nanoclusters of silver, gold, and platinum were deposited on the graphite oxide to serve as a channel. The nanoclusters were fabricated by sputtering and inert gas condensation technique inside an ultra-high compatible system. The sensor was also simulated to confirm the experimental results using Density Functional Theory (DFT) along with Non-equilibrium Green's Function formalism (NEGF) calculations. The results indicate that the sensors decorated with nanoclusters exhibit better performance than the bare sensors due to the high affinity of the trimetallic nanoclusters to DNA. The simulation results were in agreement with the experimental results. The sensor fabrication method was simple, effective, and showed great possibility for mass-production of transistor based sensors for the purpose of DNA detection at a low cost.

Graphene Oxide Field Effect Transistor (GO-FET) DNA sensor decorated with trimetallic nanoclusters of Au, Ag, and Pt was fabricated. Although monometallic gold and platinum nanoclusters have been previously presented and discussed in the GFET

sensor literature, trimetallic nanoclusters in this work are novel and resulted in higher sensitivity than the monometallic nanoclusters.

The second aim of this work was to detect the four types of DNA bases. Thus, four novel graphene-based sensors with a nanopore or a nanogap were built to detect the DNA nucleobases using Quantumwise Atomistix Toolkit (ATK) and its graphical user interface Virtual Nanolab (VNL). Simulation of structural characteristics and charge transport properties such as transmission spectrum and current were conducted for the developed sensors by Non-Equilibrium Green's function (NEGF) coupled to either semi-empirical approaches or first-principle approaches. This software was utilized through United Arab Emirates University High Performance Computing (HPC).

The first sensor was a two-terminal z-shaped nanostructured sensor consisting of two metallic electrodes connected through a semiconducting channel with a nanopore in the middle. Four DNA nucleobases were inserted in a hydrogen passivated nanopore, leading to unique differences in device transmission spectrum, current, and conductance. First-principle transport simulations were conducted for a novel nanopore graphene-based sensor to achieve an accurate DNA sequencing. The results showed that each base generates a unique signature of conductance and current at 0.5 bias voltage. The interaction of the main nucleobases: Adenine, Thymine, Cytosine, and Guanine with the graphene nanopore indicates that the sensor conductance and current are sufficiently sensitive to distinguish different nucleobases. Moreover, it is found that the nucleobase orientation within the nanopore affect current and conductance.

This work suggests that nanopore-based graphene sensor provides a robust technology for DNA sequencing and gives a strong motivation for new nanopore sequencing device development. It reveals a unique electronic signature for each of the four nucleobases which provides us with DNA electronic map. The presented sensor expounds potential to develop accurate, fast, and affordable technique for next generation DNA sequencing and detection.

The second sensor was a z-shaped graphene nanoribbon with a nanogap. Transport simulation is used to study the transmission spectrum and current for the different DNA bases within the nanogap of the z-shaped sensor where the nanogap is passivated with either hydrogen or nitrogen. Non-Equilibrium Green's Function combined with Density Functional Theory (NEGF+DFT) was used to detect the bases' effect within the nanogap. It is found that each of the DNA bases results in a unique current signature due to its unique electronic and chemical structure. Moreover, it was noticed that purine bases have higher current than pyrimidine bases. Using N-nanogap results in higher currents compared to H-nanogap which makes it easier to detect and measure. This work demonstrate significant distinction among the four DNA bases (Wasfi & Awwad, 2019a)© 2019 IEEE.

The third sensor is a novel z-shaped field-effect transistor with a nanopore. Transport simulations based on density functional theory combined with Non-Equilibrium Green's Function formalism (DFT+NEGF) were utilized to investigate the sensor performance. The study illustrated that each DNA nucleobase results in a distinctive modulation of transmission spectrum and current. The sensor has the advantage of large signal microampere at low bias voltage which allows for the detection of DNA sequence. Moreover, this work explored the effect of decorating the

sensor with gold and silver nanoparticles, which are known to have high affinity to DNA bases. It is observed that the bare sensor produced higher electronic current than the sensor decorated with gold and silver nanoparticles. Moreover, the sensor decorated with gold nanoparticles had higher electronic current than the sensor with silver nanoparticles. The mobility of bare sensor was the highest, then the sensor decorated with gold nanoparticles, and finally the one decorated with silver nanoparticles (Wasfi et al., 2020) © 2020 IOP.

The fourth sensor was also based on nanopore. Electronic transport simulations were generated using SC-EH+NEGF formalism to study the bases' signal within a pore hosted by the developed z-shaped graphene nanoribbon device. Each DNA base generated a specific signature because of its unique electronic and chemical structure. Pyrimidine nucleobases resulted in lower current than purine nucleobases. The current modifications due to the bases' orientation were studied at fixed bias voltage. Despite the current changes because of the base orientations, a unique signal for each DNA base was possible. These signals or signatures change slightly because of the bases' orientations within a pore.

The sensor sensitivity was enhanced by using nitrogen instead of hydrogen to passivate the pore edge carbon atoms. Passivation can be accomplished by nitrogen or hydrogen, where the nitrogen passivation resulted in a sensor with excess free electrons working as an n-type device. Moreover, adding a dual gate terminal to z-shaped nanoribbon and applying a gate potential improved the sensor reading and signal.

It is noticed that nanopore-based sensors results in higher current than nanogap-based sensors which makes it easier to read. Moreover, adding a gate terminal enhances the sensor performance significantly. Also, the nitrogen passivation and decorating the sensors with nanoclusters improved their performance and sensitivity.

Future work may include electronic transport calculations for nucleotides in a salt solution. Moreover, Future work will utilize the simulated sensors design to fabricate a graphene- based sensor with a nanopore that will identify the signatures of each DNA and RNA base (Adenine, Cytosine, Guanine, Uracil and Thymine) experimentally and then test the combination of bases for a known biological sample for verification purposes.

References

Adekoya, J. A., Dare, E. O., & Mesubi, M. A. (2014). Tunable morphological properties of silver enriched platinum allied nanoparticles and their catalysed reduction of p-nitrophenol. *Advances in Natural Sciences: Nanoscience and Nanotechnology, 5*(3), 035007. doi: 10.1088/2043-6262/5/3/035007

Ahmed, T., Haraldsen, J. T., Rehr, J. J., Di Ventra, M., Schuller, I., & Balatsky, A. V. (2014). Correlation dynamics and enhanced signals for the identification of serial biomolecules and DNA bases. *Nanotechnology, 25*(12), 125705. doi: 10.1088/0957-4484/25/12/125705

Akbarzadeh, H., Abbaspour, M., Mehrjouei, E., & Kamrani, M. (2018). AgPd@Pt nanoparticles with different morphologies of cuboctahedron, icosahedron, decahedron, octahedron, and Marks-decahedron: insights from atomistic simulations. *Inorganic Chemistry Frontiers, 5*(4), 870-878. doi: 10.1039/c7qi00748e

Akhavan, O., Ghaderi, E., & Rahighi, R. (2012). Toward Single-DNA Electrochemical Biosensing by Graphene Nanowalls. *ACS Nano, 6*(4), 2904-2916. doi: 10.1021/nn300261t

Akhtar, M. S., Panwar, J., & Yun, Y.-S. (2013). Biogenic Synthesis of Metallic Nanoparticles by Plant Extracts. *ACS Sustainable Chemistry & Engineering, 1*(6), 591-602. doi: 10.1021/sc300118u

Al-Dirini, F., Hossain, F. M., Nirmalathas, A., & Skafidas, E. (2014). All-Graphene Planar Self-Switching MISFEDs, Metal-Insulator-Semiconductor Field-Effect Diodes. *Scientific Reports, 4*(1), 3983. doi: 10.1038/srep03983

Al-Dirini, F., Mohammed, M., Hossain, S., Hossain, F., Nirmalathas, A., & Skafidas, E. (2016). Tuneable graphene nanopores for single biomolecule detection. *Nanoscale, 8*(19), 10066-10077. doi: 10.1039/c5nr05274b

Al Dosari, H., & Ayesh, A. (2013). Nanocluster production for solar cell applications. *Journal of Applied Physics, 114*(5), 054305. doi: 10.1063/1.4817421

Allen, B. L., Kichambare, P. D., & Star, A. (2007). Carbon Nanotube Field-Effect-Transistor-Based Biosensors. *Advanced Materials, 19*(11), 1439-1451. doi: 10.1002/adma.200602043

Amorim, R. G., Rocha, A. R., & Scheicher, R. H. (2016). Boosting DNA Recognition Sensitivity of Graphene Nanogaps through Nitrogen Edge Functionalization. *The Journal of Physical Chemistry C, 120*(34), 19384-19388. doi: 10.1021/acs.jpcc.6b04683

Andrews, D., Solomon, G., Duyne, R., & Ratner, M. (2008). Single Molecule Electronics: Increasing Dynamic Range and Switching Speed Using Cross-Conjugated Species. *Journal of the American Chemical Society, 130*, 17309-17319. doi: 10.1021/ja804399q

Antony, J., & Grimme, S. (2008). Structures and interaction energies of stacked graphene-nucleobase complexes. . *Phys Chem Chem Phys, 10*, 2722-2729. doi: 10.1039/b718788b

Arjmandi-Tash, H., Belyaeva, L., & Schneider, G. (2015). Single molecule detection with graphene and other two-dimensional materials: Nanopores and beyond. *Chem Soc Rev, 45*. doi: 10.1039/c5cs00512d

Avdoshenko, S., Nozaki, D., Gomes da Rocha, C., González, J., Lee, M., Gutierrez, R., & Cuniberti, G. (2013). Dynamic and Electronic Transport Properties of DNA Translocation through Graphene Nanopores. *Nano Letters, 13*(5), 1969-1976. doi: 10.1021/nl304735k

Ayesh, A. (2016). Linear hydrogen gas sensors based on bimetallic nanoclusters. *Journal of Alloys and Compounds, 689*, 1-5. doi: https://doi.org/10.1016/j.jallcom.2016.07.320

Ayesh, A., Ahmed, H., Awwad, F., Abu-Eishah, S., & Mahmood, S. (2013). Mechanisms of Ti nanocluster formation by inert gas condensation. *Journal of Materials Research, 28*(18), 2622-2628. doi: 10.1557/jmr.2013.246

Ayesh, A., Karam, Z., Awwad, F., & Meetani, M. (2015). Conductometric graphene sensors decorated with nanoclusters for selective detection of Hg2+ traces in water. *Sensors and Actuators B: Chemical, 221*, 201-206. doi: https://doi.org/10.1016/j.snb.2015.06.075

Ayesh, A., Mahmoud, S., Ahmad, S., & Haik, Y. (2014). Novel hydrogen gas sensor based on Pd and SnO2 nanoclusters. *Materials Letters, 128*, 354-357. doi: https://doi.org/10.1016/j.matlet.2014.04.173

Ayesh, A., Mahmoud, S., Qamhieh, N., & Karam, Z. (2014). Investigation of Charge Transport in Percolating Network of PdCu Nanoclusters. *Acta Metallurgica Sinica (English Letters), 27*, 156-160. doi: 10.1007/s40195-013-0015-1

Ayesh, A., Qamhieh, N., Mahmoud, S., & Alawadhi, H. (2012). Fabrication of size-selected bimetallic nanoclusters using magnetron sputtering. *Journal of Materials Research, 27*. doi: 10.1557/jmr.2012.205

Ayesh, A., Thaker, S., Qamhieh, N., & Ghamlouche, H. (2011). Size-controlled Pd nanocluster grown by plasma gas-condensation method. *Journal of Nanoparticle Research, 13*(3), 1125-1131. doi: 10.1007/s11051-010-0104-2

Bayley, H. (2010). Holes with an edge. *Nature, 467*(7312), 164-165. doi: 10.1038/467164a

Becke, A. D. (1988). Density-functional exchange-energy approximation with correct asymptotic behavior. *Physical Review A, 38*(6), 3098-3100. doi: 10.1103/PhysRevA.38.3098

Bolotin, K. I., Sikes, K. J., Jiang, Z., Klima, M., Fudenberg, G., Hone, J., . . . Stormer, H. L. (2008). Ultrahigh electron mobility in suspended graphene. *Solid State Communications, 146*(9), 351-355. doi: https://doi.org/10.1016/j.ssc.2008.02.024

Born, M., & Oppenheimer, R. (1927). Zur Quantentheorie der Molekeln. *Annalen der Physik, 389*(20), 457-484. doi: https://doi.org/10.1002/andp.19273892002

Brandbyge, M., Mozos, J.-L., Ordejón, P., Taylor, J., & Stokbro, K. (2002). Density-functional method for nonequilibrium electron transport. *Physical Review B, 65*(16), 165401. doi: 10.1103/PhysRevB.65.165401

Branton, D., Deamer, D. W., Marziali, A., Bayley, H., Benner, S. A., Butler, T., . . . Schloss, J. A. (2008). The potential and challenges of nanopore sequencing. *Nat Biotechnol, 26*, 1146. doi: 10.1038/nbt.1495

Bunimovich, Y. L., Shin, Y. S., Yeo, W.-S., Amori, M., Kwong, G., & Heath, J. R. (2006). Quantitative Real-Time Measurements of DNA Hybridization with Alkylated Nonoxidized Silicon Nanowires in Electrolyte Solution. *Journal of the American Chemical Society, 128*(50), 16323-16331. doi: 10.1021/ja065923u

Bunney, J., Williamson, S., Atkin, D., Jeanneret, M., Cozzolino, D., Chapman, J., . . . Chandra, S. (2017). The Use of Electrochemical Biosensors in Food Analysis. *Current Research in Nutrition and Food Science Journal, 5*, 183-195. doi: 10.12944/CRNFSJ.5.3.02

Carrillo-Torres, R. C., García-Soto, M. J., Morales-Chávez, S. D., Garibay-Escobar, A., Hernández-Paredes, J., Guzmán, R., . . . Álvarez-Ramos, M. E. (2016). Hollow Au–Ag bimetallic nanoparticles with high photothermal stability. *RSC Advances, 6*(47), 41304-41312. doi: 10.1039/C5RA25821A

Cerdá, J., & Soria, F. (2000). Accurate and transferable extended Huckel-type tight-binding parameters. *Physical Review B, 61*(12), 7965-7971. doi: 10.1103/PhysRevB.61.7965

Chandran, G. T., Li, X., Ogata, A., & Penner, R. M. (2017). Electrically Transduced Sensors Based on Nanomaterials (2012–2016). *Analytical Chemistry, 89*(1), 249-275. doi: 10.1021/acs.analchem.6b04687

Chang, P.-H., Liu, H., & Nikolic, B. (2014). First-principles vs. semi-empirical modeling of global and local electronic transport properties of graphene nanopore-based sensors for DNA sequencing. *Journal of Computational Electronics, 13*. doi: 10.1007/s10825-014-0614-8

Chaplin, M. F., & Bucke, C. (1990). *Enzyme technology,* Cambridge University Press, Cambridge.

Chen, X., Rungger, I., Pemmaraju, C. D., Schwingenschlögl, U., & Sanvito, S. (2012). First-principles study of high-conductance DNA sequencing with carbon nanotube electrodes. *Physical Review B, 85*(11), 115436. doi: 10.1103/PhysRevB.85.115436

Chin, C.-S., Sorenson, J., Harris, J. B., Robins, W. P., Charles, R. C., Jean-Charles, R. R., . . . Waldor, M. K. (2011). The origin of the Haitian cholera outbreak strain. *The New England journal of medicine, 364*(1), 33-42. doi: 10.1056/NEJMoa1012928

Ci, L., Xu, Z., Wang, L., Gao, W., Ding, F., Kelly, K., . . . Ajayan, P. (2008). Controlled Nanocutting of Graphene. *Nano Research, 1*, 116-122. doi: 10.1007/s12274-008-8020-9

Clark , L., & Lyons, C. (1962). ELECTRODE SYSTEMS FOR CONTINUOUS MONITORING IN CARDIOVASCULAR SURGERY. *Annals of the New York Academy of Sciences, 102*(1), 29-45. doi: 10.1111/j.1749-6632.1962.tb13623.x

Clarke, J., Wu, H.-C., Jayasinghe, L., Patel, A., Reid, S., & Bayley, H. (2009). Continuous base identification for single-molecule nanopore DNA sequencing. *Nat Nanotechnol, 4*(4), 265-270. doi: 10.1038/nnano.2009.12

Cramer, C. J. (2002). *Essentials of computational chemistry : theories and models*: West Sussex, England ; New York : J. Wiley, [2002] ©2002.

Curreli, M., Zhang, R., Ishikawa, F. N., Chang, H., Cote, R. J., Zhou, C., & Thompson, M. E. (2008). Real-Time, Label-Free Detection of Biological Entities Using Nanowire-Based FETs. *IEEE Transactions on Nanotechnology, 7*(6), 651-667. doi: 10.1109/TNANO.2008.2006165

Datta, S. (1995). *Electronic Transport in Mesoscopic Systems*. Cambridge: Cambridge University Press.

Datta, S. (2005). *Quantum Transport: Atom to Transistor*. Cambridge: Cambridge University Press.

Datta, S., Strachan, D., Khamis, S., & Johnson, c. (2008). Crystallographic Etching of Few-Layer Graphene. *Nano Letters, 8*, 1912-1915. doi: 10.1021/nl080583r

de Souza, F. A., Amorim, R. G., Scopel, W. L., & Scheicher, R. H. (2017). Electrical detection of nucleotides via nanopores in a hybrid graphene/h-BN sheet. *Nanoscale, 9*(6), 2207-2212. doi: 10.1039/c6nr07154f

Demirbas, A., Yilmaz, V., Ildiz, N., Baldemir, A., & Ocsoy, I. (2017). Anthocyanins-rich berry extracts directed formation of Ag NPs with the investigation of their antioxidant and antimicrobial activities. *Journal of Molecular Liquids, 248*, 1044-1049. doi: 10.1016/j.molliq.2017.10.130

Dewar, M. J. S., Hashmall, J. A., & Venier, C. G. (1968). Ground states of conjugated molecules. IX. Hydrocarbon radicals and radical ions. *Journal of the American Chemical Society, 90*(8), 1953-1957. doi: 10.1021/ja01010a005

Dong, X., Shi, Y., Huang, W., Chen, P., & Li, L.-J. (2010). Electrical Detection of DNA Hybridization with Single-Base Specificity Using Transistors Based on CVD-Grown Graphene Sheets. *Advanced Materials, 22*(14), 1649-1653. doi: 10.1002/adma.200903645

Dontschuk, N., Stacey, A., Tadich, A., Rietwyk, K. J., Schenk, A., Edmonds, M. T., . . . Cervenka, J. (2015). A graphene field-effect transistor as a molecule-specific probe of DNA nucleobases. *Nature Communications, 6*(1), 6563. doi: 10.1038/ncomms7563

Drmanac, R., Sparks, A. B., Callow, M. J., Halpern, A. L., Burns, N. L., Kermani, B. G., . . . Reid, C. A. (2010). Human Genome Sequencing Using Unchained Base Reads on Self-Assembling DNA Nanoarrays. *Science, 327*(5961), 78-81. doi: 10.1126/science.1181498

Duan, X., Li, Y., Rajan, N. K., Routenberg, D. A., Modis, Y., & Reed, M. A. (2012). Quantification of the affinities and kinetics of protein interactions using silicon nanowire biosensors. *Nat Nanotechnol, 7*(6), 401-407. doi: 10.1038/nnano.2012.82

Eisenstein, M. (2012). Oxford Nanopore announcement sets sequencing sector abuzz. *Nat Biotechnol, 30*(4), 295-296. doi: 10.1038/nbt0412-295

Elahi, N., Kamali, M., & Baghersad, M. H. (2018). Recent biomedical applications of gold nanoparticles: A review. *Talanta, 184*, 537-556. doi: 10.1016/j.talanta.2018.02.088

Elstner, M., Porezag, D., Jungnickel, G., Elsner, J., Haugk, M., Frauenheim, T., . . . Seifert, G. (1998). Self-consistent-charge density-functional tight-binding method for simulations of complex materials properties. *Physical Review B, 58*(11), 7260-7268. doi: 10.1103/PhysRevB.58.7260

Fauzia, V., Irmavianti, D., Roza, L., Elita Hafizah, M. A., Imawan, C., & Umar, A. A. (2019). Bimetallic AuAg sharp-branch mesoflowers as catalyst for hydrogenation of acetone. *Materials Chemistry and Physics, 225*, 443-450. doi: https://doi.org/10.1016/j.matchemphys.2019.01.013

Fiers, W., Contreras, R., Duerinck, F., Haegeman, G., Iserentant, D., Merregaert, J., . . . Ysebaert, M. (1976). Complete nucleotide sequence of bacteriophage MS2 RNA: primary and secondary structure of the replicase gene. *Nature, 260*(5551), 500-507. doi: 10.1038/260500a0

Fischbein, M., & Drndic, M. (2008). Electron Beam Nanosculpting of Suspended Graphene Sheets. *Applied Physics Letters, 93*. doi: 10.1063/1.2980518

Ganguly, A., Chen, C.-P., Lai, Y.-T., Kuo, C.-C., Hsu, C.-W., Chen, K.-H., & Chen, L.-C. (2009). Functionalized GaN nanowire-based electrode for direct label-free voltammetric detection of DNA hybridization. *Journal of Materials Chemistry - J MATER CHEM, 19*. doi: 10.1039/b816556d

Goldman, N., Bertone, P., Chen, S., Dessimoz, C., Leproust, E., Sipos, B., & Birney, E. (2013). Towards practical, high-capacity, low-maintenance information storage in synthesized DNA. *Nature, 494*. doi: 10.1038/nature11875

Greenleaf, W., & Sidow, A. (2014). The future of sequencing: Convergence of intelligent design and market Darwinism. *Genome biology, 15*, 303. doi: 10.1186/gb4168

Gupta, M., Gaur, N., Kumar, P., Singh, S., Jaiswal, N., & Kondekar, N. (2015). Tailoring the electronic properties of a Z-shaped graphene field effect transistor via B/N doping. *Physics Letters A, 379*(7), 710-718. doi: 10.1016/j.physleta.2014.12.046

Hahm, J.-i., & Lieber, C. M. (2004). Direct Ultrasensitive Electrical Detection of DNA and DNA Sequence Variations Using Nanowire Nanosensors. *Nano Letters, 4*(1), 51-54. doi: 10.1021/nl034853b

Haque, F., Li, J., Wu, H. C., Liang, X. J., & Guo, P. (2013). Solid-State and Biological Nanopore for Real-Time Sensing of Single Chemical and Sequencing of DNA. *Nano Today, 8*(1), 56-74. doi: 10.1016/j.nantod.2012.12.008

He, Y., Scheicher, R., Grigoriev, A., Ahuja, R., Long, S., Huo, Z., & Liu, M. (2011). Enhanced DNA Sequencing Performance Through Edge-Hydrogenation of Graphene Electrodes. *Advanced Functional Materials, 21*, 2674-2679. doi: 10.1002/adfm.201002530

He, Y., Shao, L., Scheicher, R., Grigoriev, A., Ahuja, R., Long, S., . . . Liu, M. (2010). Differential conductance as a promising approach for rapid DNA sequencing with nanopore-embedded electrodes. *Appl. Phys. Lett.* 97 (4), 043701, doi: 10.1063/1.3467194.

Healy, K., Schiedt, B., & Morrison, A. P. (2008). Solid-state nanopore technologies for nanopore-based DNA analysis. *Nanomedicine*, 2(6), 875–897. doi:10.2217/17435889.2.6.875

Heerema, S. J., & Dekker, C. (2016). Graphene nanodevices for DNA sequencing. *Nat Nanotechnol, 11*(2), 127-136. doi: 10.1038/nnano.2015.307

Heerema, S. J., Vicarelli, L., Pud, S., Schouten, R. N., Zandbergen, H. W., & Dekker, C. (2018). Probing DNA Translocations with Inplane Current Signals in a Graphene Nanoribbon with a Nanopore. *ACS Nano, 12*(3), 2623-2633. doi: 10.1021/acsnano.7b08635

Hoffmann, R. (1963). An Extended Hückel Theory. I. Hydrocarbons. *J Chem Phys, 39*(6), 1397-1412. doi: 10.1063/1.1734456

Hohenberg, P., & Kohn, W. (1964). Inhomogeneous Electron Gas. *Physical Review, 136*(3B), B864-B871. doi: 10.1103/PhysRev.136.B864

Holley, R. W., Apgar, J., Everett, G. A., Madison, J. T., Marquisee, M., Merrill, S. H., . . . Zamir, A. (1965). Structure of a Ribonucleic Acid. *Science, 147*(3664), 1462. doi: 10.1126/science.147.3664.1462

Homola, J. (2008). Surface Plasmon Resonance Sensors for Detection of Chemical and Biological Species. *Chemical reviews, 108*(2), 462-493. doi: 10.1021/cr068107d

Huang, Jiao, C., Wang, L., Huang, Z., Liang, F., Liu, S., . . . Zhang, S. (2017). Preparation of Rh/Ag bimetallic nanoparticles as effective catalyst for hydrogen generation from hydrolysis of KBH4. *Nanotechnology, 29*(4), 044002. doi: 10.1088/1361-6528/aa9b19

Huang, S., He, J., Chang, S., Zhang, P., Liang, F., Li, S., . . . Lindsay, S. (2010). Identifying single bases in a DNA oligomer with electron tunnelling. *Nat Nanotechnol, 5*(12), 868-873. doi: 10.1038/nnano.2010.213

Hugenholtz, P., & Tyson, G. W. (2008). Metagenomics. *Nature, 455*(7212), 481-483. doi: 10.1038/455481a

Irene Ling, L., Si Fan, C., & Jian Pang, Z. (2015). *The Raman spectrum of graphene oxide decorated with different metal nanoparticles.* Paper presented at the Proc.SPIE.

Jones, S., Hruban, R. H., Kamiyama, M., Borges, M., Zhang, X., Parsons, D. W., . . . Klein, A. P. (2009). Exomic sequencing identifies PALB2 as a pancreatic cancer susceptibility gene. *Science (New York, N.Y.), 324*(5924), 217. doi: 10.1126/science.1171202

Jordan, C. E., Frutos, A. G., Thiel, A. J., & Corn, R. M. (1997). Surface Plasmon Resonance Imaging Measurements of DNA Hybridization Adsorption and Streptavidin/DNA Multilayer Formation at Chemically Modified Gold Surfaces. *Analytical Chemistry, 69*(24), 4939-4947. doi: 10.1021/ac9709763

Jou, W. M., Haegeman, G., Ysebaert, M., & Fiers, W. (1972). Nucleotide Sequence of the Gene Coding for the Bacteriophage MS2 Coat Protein. *Nature, 237*(5350), 82-88. doi: 10.1038/237082a0

Kang, H., Kulkarni, A., Stankovich, S., Ruoff, R. S., & Baik, S. (2009). Restoring electrical conductivity of dielectrophoretically assembled graphite oxide sheets by thermal and chemical reduction techniques. *Carbon, 47*(6), 1520-1525. doi: https://doi.org/10.1016/j.carbon.2009.01.049

Kienle, D., Bevan, K. H., Liang, G. C., Siddiqui, L., Cerda, J. I., & Ghosh, A. W. (2006). Extended Hückel theory for band structure, chemistry, and transport. II. Silicon. *Journal of Applied Physics, 100*(4), 043715. doi: 10.1063/1.2259820

Kienle, D., Cerda, J. I., & Ghosh, A. W. (2006). Extended Hückel theory for band structure, chemistry, and transport. I. Carbon nanotubes. *Journal of Applied Physics, 100*(4), 043714. doi: 10.1063/1.2259818

Kohn, & Sham. (1965). Self-Consistent Equations Including Exchange and Correlation Effects. *Physical Review, 140*(4A), A1133-A1138. doi: 10.1103/PhysRev.140.A1133

Koskinen, P., & Mäkinen, V. (2009). Density-functional tight-binding for beginners. *Computational Materials Science, 47*(1), 237-253. doi: https://doi.org/10.1016/j.commatsci.2009.07.013

Krems, M., Zwolak, M., Pershin, Y. V., & Di Ventra, M. (2009). Effect of Noise on DNA Sequencing via Transverse Electronic Transport. *Biophysical Journal*, *97*(7), 1990–1996. doi:10.1016/j.bpj.2009.06.055

Lagerqvist, J., Zwolak, M., & Di Ventra, M. (2006). Fast DNA Sequencing via Transverse Electronic Transport. *Nano Letters, 6*(4), 779-782. doi: 10.1021/nl0601076

Lagerqvist, J., Zwolak, M., & Di Ventra, M. (2007). Influence of the environment and probes on rapid DNA sequencing via transverse electronic transport. *Biophys J, 93*(7), 2384-2390. doi: 10.1529/biophysj.106.102269

Lander, E. S., Linton, L. M., Birren, B., Nusbaum, C., Zody, M. C., Baldwin, J., . . . The Wellcome, T. (2001). Initial sequencing and analysis of the human genome. *Nature, 409*(6822), 860-921. doi: 10.1038/35057062

Le, D., Kara, A., Schröder, E., Hyldgaard, P., & Rahman, T. (2012). Physisorption of nucleobases on graphene: A comparative van der Waals study. *Journal of physics. Condensed matter : an Institute of Physics journal, 24*, 424210. doi: 10.1088/0953-8984/24/42/424210

Leão de Souza, F., Amorim, R., Scopel, W., & Scheicher, R. (2019). Controlled current confinement in interfaced 2D nanosensor for electrical identification of DNA. *Physical Chemistry Chemical Physics, 21*. doi: 10.1039/C9CP03950C

Lee, J.-H., Choi, Y.-K., Kim, H.-J., Scheicher, R. H., & Cho, J.-H. (2013). Physisorption of DNA Nucleobases on h-BN and Graphene: vdW-Corrected DFT Calculations. *The Journal of Physical Chemistry C, 117*(26), 13435-13441. doi: 10.1021/jp402403f

Lennard-Jones, J. E. (1929). The electronic structure of some diatomic molecules. *Transactions of the Faraday Society, 25*(0), 668-686. doi: 10.1039/TF9292500668

Li, & Du, X. (2017). Molybdenum disulfide nanosheets supported Au-Pd bimetallic nanoparticles for non-enzymatic electrochemical sensing of hydrogen peroxide and glucose. *Sensors and Actuators B: Chemical, 239*, 536-543. doi: https://doi.org/10.1016/j.snb.2016.08.048

Li, Liu, F., Fan, Y., Cheng, G., Song, W., & Zhou, J. (2018). Silver palladium bimetallic core-shell structure catalyst supported on TiO2 for toluene oxidation. *Applied Surface Science, 462*, 207-212. doi: https://doi.org/10.1016/j.apsusc.2018.08.023

Li, Zheng, H., Guo, L., Qu, L., & Yu, L. (2019). Construction of novel electrochemical sensors based on bimetallic nanoparticle functionalized graphene for determination of sunset yellow in soft drink. *Journal of Electroanalytical Chemistry, 833*, 393-400. doi: https://doi.org/10.1016/j.jelechem.2018.11.059

Li, Z., Liu, Z., Sun, H., & Gao, C. (2015). Superstructured Assembly of Nanocarbons: Fullerenes, Nanotubes, and Graphene. *Chemical reviews, 115*(15), 7046-7117. doi: 10.1021/acs.chemrev.5b00102

Ligler, F., Taitt, C., Shriver-Lake, L., Sapsford, K., Shubin, Y., & Golden, J. (2003). Array biosensor for detection of toxins. Anal Bioanal Chem 377:469. *Analytical and bioanalytical chemistry, 377*, 469-477. doi: 10.1007/s00216-003-1992-0

Ling, H.-Q., Zhao, S., Liu, D., Wang, J., Sun, H., Zhang, C., . . . Wang, J. (2013). Draft genome of the wheat A-genome progenitor Triticum urartu. *Nature, 496*(7443), 87-90. doi: 10.1038/nature11997

Liu, Yan, X., Lai, Q., & Su, X. (2019). Bimetallic gold/silver nanoclusters-gold nanoparticles based fluorescent sensing platform via the inner filter effect for hyaluronidase activity detection. *Sensors and Actuators B: Chemical, 282*, 45-51. doi: https://doi.org/10.1016/j.snb.2018.11.040

Liu, X., Wang, D., & Li, Y. (2012). Synthesis and catalytic properties of bimetallic nanomaterials with various architectures. *Nano Today, 7*(5), 448-466. doi: https://doi.org/10.1016/j.nantod.2012.08.003

Lloyd, K. G., Schreiber, L., Petersen, D. G., Kjeldsen, K. U., Lever, M. A., Steen, A. D., . . . Jørgensen, B. B. (2013). Predominant archaea in marine sediments degrade detrital proteins. *Nature, 496*(7444), 215-218. doi: 10.1038/nature12033

Luan, B., Peng, H., Polonsky, S., Rossnagel, S., Stolovitzky, G., & Martyna, G. (2010). Base-by-base ratcheting of single stranded DNA through a solid-state nanopore. *Physical review letters, 104*(23), 238103. doi: 10.1103/physrevlett.104.238103

Luan, B., Wang, D., Zhou, R., Harrer, S., Peng, H., & Stolovitzky, G. (2012). Dynamics of DNA translocation in a solid-state nanopore immersed in aqueous glycerol. *Nanotechnology, 23*(45), 455102. doi: 10.1088/0957-4484/23/45/455102

Magoga, M., & Joachim, C. (1997). Conductance and transparence of long molecular wires. *Physical Review B, 56*(8), 4722-4729. doi: 10.1103/PhysRevB.56.4722

Mahmoud, A., & Lugli, P. (2012). Designing the rectification behavior of molecular diodes. *Journal of Applied Physics, 112*(11), 113720. doi: 10.1063/1.4768924

Margulies, M., Egholm, M., Altman, W. E., Attiya, S., Bader, J. S., Bemben, L. A., . . . Rothberg, J. M. (2005). Genome sequencing in microfabricated high-density picolitre reactors. *Nature, 437*(7057), 376-380. doi: 10.1038/nature03959

Maxam, A. M., & Gilbert, W. (1977). A new method for sequencing DNA. *Proceedings of the National Academy of Sciences, 74*(2), 560. doi: 10.1073/pnas.74.2.560

McFarland, H. L., Ahmed, T., Zhu, J. X., Balatsky, A. V., & Haraldsen, J. T. (2015). First-Principles Investigation of Nanopore Sequencing Using Variable Voltage Bias on Graphene-Based Nanoribbons. *J Phys Chem Lett, 6*(13), 2616-2621. doi: 10.1021/acs.jpclett.5b01014

Meunier, V., & Krstic, P. (2008). Enhancement of the transverse conductance in DNA nucleotides. *J Chem Phys, 128*(4), 041103. doi: 10.1063/1.2835350

Mohanty, N., & Berry, V. (2008). Graphene-Based Single-Bacterium Resolution Biodevice and DNA Transistor: Interfacing Graphene Derivatives with Nanoscale and Microscale Biocomponents. *Nano Letters, 8*(12), 4469-4476. doi: 10.1021/nl802412n

Moskovits, M. (1985). Surface-enhanced spectroscopy. *Reviews of Modern Physics, 57*(3), 783-826. doi: 10.1103/RevModPhys.57.783

Mu, L., Droujinine, I. A., Rajan, N. K., Sawtelle, S. D., & Reed, M. A. (2014). Direct, Rapid, and Label-Free Detection of Enzyme–Substrate Interactions in Physiological Buffers Using CMOS-Compatible Nanoribbon Sensors. *Nano Letters, 14*(9), 5315-5322. doi: 10.1021/nl502366e

Narendar, V., Gupta, S. K., & Saxena, S. (2018). First Principle Study of Doped Graphene for FET Applications. *Silicon, 11*(1), 277-286. doi: 10.1007/s12633-018-9852-x

Nelson, B., Grimsrud, T., Liles, M., Goodman, R., & Corn, R. (2001). Surface Plasmon Resonance Imaging Measurements of DNA and RNA Hybridization Adsorption onto DNA Microarrays. *Analytical Chemistry, 73*(1), 1-7. doi: 10.1021/ac0010431

Nelson, T., Zhang, B., & Prezhdo, O. (2010). Detection of Nucleic Acids with Graphene Nanopores: Ab Initio Characterization of a Novel Sequencing Device. *Nano Letters, 10*, 3237-3242. doi: 10.1021/nl9035934

Novoselov, K. S., Geim, A. K., Morozov, S. V., Jiang, D., Zhang, Y., Dubonos, S. V., . . . Firsov, A. A. (2004). Electric Field Effect in Atomically Thin Carbon Films. *Science, 306*(5696), 666. doi: 10.1126/science.1102896

Ohno, Y., Okamoto, S., Maehashi, K., & Matsumoto, K. (2013). Direct Electrical Detection of DNA Hybridization Based on Electrolyte-Gated Graphene Field-Effect Transistor. *Japanese Journal of Applied Physics, 52*(11R), 110107. doi: 10.7567/jjap.52.110107

Okuda, S., Okamoto, S., Ohno, Y., Maehashi, K., Inoue, K., & Matsumoto, K. (2012). Horizontally Aligned Carbon Nanotubes on a Quartz Substrate for Chemical and Biological Sensing. *The Journal of Physical Chemistry C, 116*(36), 19490-19495. doi: 10.1021/jp301542w

Oliveira-Brett, A., & Paquim, A. M. C. (2003). Atomic Force Microscopy of DNA Immobilized onto a Highly Oriented Pyrolytic Graphite Electrode Surface. *Langmuir, 19*. doi: 10.1021/la027047d

Palaniappan, A., Goh, W. H., Tey, J. N., Wijaya, I. P. M., Moochhala, S. M., Liedberg, B., & Mhaisalkar, S. G. (2010). Aligned carbon nanotubes on quartz substrate for liquid gated biosensing. *Biosensors and Bioelectronics, 25*(8), 1989-1993. doi: https://doi.org/10.1016/j.bios.2010.01.009

Pandey, B. (2018). Transmission spectrum and IV characteristics of dual-gate Z-shaped graphene nanoribbon FET. *Nanomaterials and Energy, 7*(2), 32-36. doi: 10.1680/jnaen.17.00013

Pandey, P. C., & Pandey, G. (2016). One-pot two-step rapid synthesis of 3-aminopropyltrimethoxysilane-mediated highly catalytic Ag@(PdAu) trimetallic nanoparticles. *Catalysis Science & Technology, 6*(11), 3911-3917. doi: 10.1039/C5CY02040A

Pantelopoulos, A., & Bourbakis, N. (2010). A Survey on Wearable Sensor-Based Systems for Health Monitoring and Prognosis. *IEEE Transactions on Systems, Man, and Cybernetics, Part C (Applications and Reviews), 40*, 1-12. doi: 10.1109/TSMCC.2009.2032660

Pauli, W. (1925). Über den Zusammenhang des Abschlusses der Elektronengruppen im Atom mit der Komplexstruktur der Spektren. *Zeitschrift für Physik, 31*(1), 765-783. doi: 10.1007/BF02980631

Paulsson, M. (2002). Non Equilibrium Green's Functions for Dummies: Introduction to the One Particle NEGF equations.

Pecchia, A., & Di Carlo, A. (2004). Atomistic theory of transport in organic and inorganic nanostructures. *Reports on Progress in Physics, 67*, 1497-1561. doi: 10.1088/0034-4885/67/8/R04

Pecchia, A., Penazzi, G., Salvucci, L., & Di Carlo, A. (2008). Non-equilibrium Green's functions in density functional tight binding: method and applications. *New Journal of Physics, 10*(6), 065022. doi: 10.1088/1367-2630/10/6/065022

Penazzi, G., Carlsson, J. M., Diedrich, C., Olf, G., Pecchia, A., & Frauenheim, T. (2013). Atomistic Modeling of Charge Transport across a Carbon Nanotube–Polyethylene Junction. *The Journal of Physical Chemistry C, 117*(16), 8020-8027. doi: 10.1021/jp312381k

Perdew, J., Burke, K., & Ernzerhof, M. (1996). Generalized Gradient Approximation Made Simple. *Physical review letters, 77*(18), 3865-3868. doi: 10.1103/PhysRevLett.77.3865

Perdew, J., & Zunger, A. (1981). Self-interaction correction to density-functional approximations for many-electron systems. *Physical Review B, 23*(10), 5048-5079. doi: 10.1103/PhysRevB.23.5048

Petrucci, R. H., Harwood, W. S., Herring, G. F., & Madura, J. D. (2007). *General chemistry : principles and modern applications*. Upper Saddle River; New Jersey: Pearson Prentice Hall.

Porezag, D., Frauenheim, T., Köhler, T., Seifert, G., & Kaschner, R. (1995). Construction of tight-binding-like potentials on the basis of density-functional theory: Application to carbon. *Physical Review B, 51*(19), 12947-12957. doi: 10.1103/PhysRevB.51.12947

Postma, H. (2010). Rapid Sequencing of Individual DNA Molecules in Graphene Nanogaps. *Nano Letters, 10*, 420-425. doi: 10.1021/nl9029237

Prasongkit, J., Grigoriev, A., Pathak, B., Ahuja, R., & Scheicher, R. (2011). Transverse conductance of DNA nucleotides in a graphene nanogap from first principles. *Nano Lett, 11*(5), 1941-1945. doi: 10.1021/nl200147x

Qiu, H., Sarathy, A., Leburton, J.-P., & Schulten, K. (2015). Intrinsic Stepwise Translocation of Stretched ssDNA in Graphene Nanopores. *Nano Lett, 15*(12), 8322-8330. doi: 10.1021/acs.nanolett.5b03963

Qiu, H., Sarathy, A., Leburton, J.-P., & Schulten, K. (2016). Stepwise Transport of Stretched ssDNA Through Graphene Nanopores. *Biophysical journal, 110*(3), 508a. doi: 10.1016/j.bpj.2015.11.2716

Qiu, W., Nguyen, P., & Skafidas, E. (2014). Graphene nanopores: electronic transport properties and design methodology. *Phys Chem Chem Phys, 16*(4), 1451-1459. doi: 10.1039/c3cp53777c

Rai, M., Ingle, A. P., Birla, S., Yadav, A., & Santos, C. A. (2016). Strategic role of selected noble metal nanoparticles in medicine. *Crit Rev Microbiol, 42*(5), 696-719. doi: 10.3109/1040841X.2015.1018131

Robinson, J. T., Thorvaldsdóttir, H., Winckler, W., Guttman, M., Lander, E. S., Getz, G., & Mesirov, J. P. (2011). Integrative genomics viewer. *Nat Biotechnol, 29*(1), 24-26. doi: 10.1038/nbt.1754

Rodriguez-Proenza, C. A., Palomares-Baez, J. P., Chavez-Rojo, M. A., Garcia-Ruiz, A. F., Azanza-Ricardo, C. L., Santovena-Uribe, A., . . . Esparza, R. (2018). Atomic Surface Segregation and Structural Characterization of PdPt Bimetallic Nanoparticles. *Materials (Basel), 11*(10). doi: 10.3390/ma11101882

Rothberg, J. M., Hinz, W., Rearick, T. M., Schultz, J., Mileski, W., Davey, M., . . . Bustillo, J. (2011). An integrated semiconductor device enabling non-optical genome sequencing. *Nature, 475*(7356), 348-352. doi: 10.1038/nature10242

Saha, K., Drndić, M., & Nikolić, B. (2012). DNA Base-Specific Modulation of Microampere Transverse Edge Currents through a Metallic Graphene Nanoribbon with a Nanopore. *Nano Letters, 12*(1), 50-55. doi: 10.1021/nl202870y

Sahoo, A., Tripathy, S. K., Dehury, N., & Patra, S. (2015). A porous trimetallic Au@Pd@Ru nanoparticle system: synthesis, characterisation and efficient dye degradation and removal. *Journal of Materials Chemistry A, 3*(38), 19376-19383. doi: 10.1039/C5TA03959B

Said, A. R., Said, K., Awwad, F., Qamhieh, N. N., Mahmoud, S. T., Meetani, M. A., . . . Ayesh, A. I. (2018). Design, fabrication, and characterization of Hg2+ sensor based on graphite oxide and metallic nanoclusters. *Sensors and Actuators A: Physical, 271*, 270-277. doi: 10.1016/j.sna.2018.01.033

Said, K., Ayesh, A., Qamhieh, N., Awwad, F., Mahmoud, S., & Hisaindee, S. (2017). Fabrication and characterization of graphite oxide – nanoparticle composite based field effect transistors for non-enzymatic glucose sensor applications. *Journal of Alloys and Compounds, 694*, 1061-1066. doi: https://doi.org/10.1016/j.jallcom.2016.10.168

Sanger, F., Brownlee, G. G., & Barrell, B. G. (1965). A two-dimensional fractionation procedure for radioactive nucleotides. *Journal of Molecular Biology, 13*(2), 373-IN374. doi: https://doi.org/10.1016/S0022-2836(65)80104-8

Sanger, F., & Coulson, A. R. (1975). A rapid method for determining sequences in DNA by primed synthesis with DNA polymerase. *Journal of Molecular Biology, 94*(3), 441-448. doi: https://doi.org/10.1016/0022-2836(75)90213-2

Sathe, C., Zou, X., Leburton, J.-P., & Schulten, K. (2011). Computational Investigation of DNA Detection Using Graphene Nanopores. *ACS Nano, 5*(11), 8842-8851. doi: 10.1021/nn202989w

Scheuermann, G. M., Rumi, L., Steurer, P., Bannwarth, W., & Mülhaupt, R. (2009). Palladium Nanoparticles on Graphite Oxide and Its Functionalized Graphene Derivatives as Highly Active Catalysts for the Suzuki−Miyaura Coupling Reaction. *Journal of the American Chemical Society, 131*(23), 8262-8270. doi: 10.1021/ja901105a

Schneider, G. F., Kowalczyk, S. W., Calado, V. E., Pandraud, G., Zandbergen, H. W., Vandersypen, L. M. K., & Dekker, C. (2010). DNA Translocation through Graphene Nanopores. *Nano Letters, 10*(8), 3163-3167. doi: 10.1021/nl102069z

Schuster, S. C. (2008). Next-generation sequencing transforms today's biology. *Nature Methods, 5*(1), 16-18. doi: 10.1038/nmeth1156

Sh, G., Scheicher, R., Ahuja, R., Pandey, R., & Karna, S. (2007). Physisorption of nucleobases on graphene: Density-functional calculations. *Physical Review B, 76*, 033401. doi: 10.1103/PhysRevB.76.033401

Sheka, E. F. (2014). The uniqueness of physical and chemical natures of graphene: Their coherence and conflicts. *International Journal of Quantum Chemistry*, 114(16), 1079–1095. doi:10.1002/qua.24673

Slater, J. C. (1930). Atomic Shielding Constants. *Physical Review, 36*(1), 57-64. doi: 10.1103/PhysRev.36.57

Slater, J. C. (1951). A Simplification of the Hartree-Fock Method. *Physical Review, 81*(3), 385-390. doi: 10.1103/PhysRev.81.385

Solomon, G., Gagliardi, A., Pecchia, A., Frauenheim, T., Di Carlo, A., Reimers, J., & Hush, N. (2006). The symmetry of single-molecule conduction. *J Chem Phys, 125*, 184702. doi: 10.1063/1.2363976

Song, Y.-m., Lu, X.-l., Yang, M.-l., & Zheng, X.-r. (2005). Study on the interaction of platinum(IV), gold(III) and silver(I) ions with DNA. *Transition Metal Chemistry, 30*(4), 499-502. doi: 10.1007/s11243-005-2663-0

Srinoi, P., Chen, Y.-T., Vittur, V., Marquez, M., & Lee, R. (2018). Bimetallic Nanoparticles: Enhanced Magnetic and Optical Properties for Emerging Biological Applications. *Applied Sciences, 8*(7), 1106. doi: 10.3390/app8071106

Stern, E., Vacic, A., & Reed, M. A. (2008). Semiconducting Nanowire Field-Effect Transistor Biomolecular Sensors. *IEEE Transactions on Electron Devices, 55*(11), 3119-3130. doi: 10.1109/TED.2008.2005168

Stewart, J. J. P. (1990). MOPAC: A semiempirical molecular orbital program. *Journal of Computer-Aided Molecular Design, 4*(1), 1-103. doi: 10.1007/BF00128336

Stokbro, K., Petersen, D., Smidstrup, S., Blom, A., Ipsen, M., & Kaasbjerg, K. (2010). Semi-Empirical Model for Nano-Scale Device Simulations. *Physical Review B, 82*. doi: 10.1103/PhysRevB.82.075420

Syu, Y.-C., Hsu, W.-E., & Lin, C.-T. (2018). Review—Field-Effect Transistor Biosensing: Devices and Clinical Applications. *ECS Journal of Solid State Science and Technology, 7*(7), Q3196-Q3207. doi: 10.1149/2.0291807jss

Tang, X., Bansaruntip, S., Nakayama, N., Yenilmez, E., Chang, Y.-l., & Wang, Q. (2006). Carbon Nanotube DNA Sensor and Sensing Mechanism. *Nano Letters, 6*(8), 1632-1636. doi: 10.1021/nl060613v

Tapasztó, L., Dobrik, G., Lambin, P., & Biró, L. P. (2008). Tailoring the atomic structure of graphene nanoribbons by scanning tunnelling microscope lithography. *Nat Nanotechnol, 3*(7), 397-401. doi: 10.1038/nnano.2008.149

Taylor, J., Guo, H., & Wang, J. (2001). Ab initio modeling of quantum transport properties of molecular electronic devices. *Physical Review B, 63*(24), 245407. doi: 10.1103/PhysRevB.63.245407

Thiel, W., & Voityuk, A. (1996). Extension of MNDO to d Orbitals: Parameters and Results for the Second-Row Elements and for the Zinc Group. *The Journal of Physical Chemistry, 100*(2), 616-626. doi: 10.1021/jp952148o

Tian, M., Xu, S., Zhang, J., Wang, X., Li, Z., Liu, H., . . . Wang, J. (2018). RNA Detection Based on Graphene Field-Effect Transistor Biosensor. *Advances in Condensed Matter Physics, 2018*, 1-6. doi: 10.1155/2018/8146765

Tjoa, V., Wei, J., Dravid, V., Mhaisalkar, S., & Mathews, N. (2011). Hybrid graphene-metal nanoparticle systems: Electronic properties and gas interaction. *J. Mater. Chem., 21*, 15593-15599. doi: 10.1039/C1JM12676H

Torrisi, F., & Carey, T. (2018). Graphene, related two-dimensional crystals and hybrid systems for printed and wearable electronics. *Nano Today, 23*, 73-96. doi: 10.1016/j.nantod.2018.10.009

Toshima, N., & Yonezawa, T. (1998). Bimetallic nanoparticles—novel materials for chemical and physical applications. *New Journal of Chemistry, 22*(11), 1179-1201. doi: 10.1039/A805753B

Tothill, I. E. (2009). Biosensors for cancer markers diagnosis. *Semin Cell Dev Biol, 20*(1), 55-62. doi: 10.1016/j.semcdb.2009.01.015

Traversi, F., Raillon, C., Benameur, S. M., Liu, K., Khlybov, S., Tosun, M., . . . Radenovic, A. (2013). Detecting the translocation of DNA through a nanopore using graphene nanoribbons. *Nat Nanotechnol, 8*, 939. doi: 10.1038/nnano.2013.240

Tsutsui, M., Taniguchi, M., Yokota, K., & Kawai, T. (2010). Identifying single nucleotides by tunnelling current. *Nat Nanotechnol, 5*, 286. doi: 10.1038/nnano.2010.42

Veigas, B., Fortunato, E., & Baptista, P. (2015). Field Effect Sensors for Nucleic Acid Detection: Recent Advances and Future Perspectives. *Sensors, 15*, 10380-10398. doi: 10.3390/s150510380

Venema, L. C., Wildöer, J. W. G., Tuinstra, H. L. J. T., Dekker, C., Rinzler, A. G., & Smalley, R. E. (1997). Length control of individual carbon nanotubes by nanostructuring with a scanning tunneling microscope. *Applied Physics Letters, 71*(18), 2629-2631. doi: 10.1063/1.120161

Vicarelli, L., Heerema, S., Dekker, C., & Zandbergen, H. (2015). Controlling Defects in Graphene for Optimizing the Electrical Properties of Graphene Nanodevices. *ACS Nano, 9*. doi: 10.1021/acsnano.5b01762

Voelkerding, K. V., Dames, S. A., & Durtschi, J. D. (2009). Next-Generation Sequencing: From Basic Research to Diagnostics. *Clinical chemistry, 55*(4), 641-658. doi: 10.1373/clinchem.2008.112789

Wakabayashi, K., Takane, Y., Yamamoto, M., & Sigrist, M. (2009). Electronic transport properties of graphene nanoribbons. *New Journal of Physics, 11*(9), 095016. doi: 10.1088/1367-2630/11/9/095016

Wang, W. U., Chen, C., Lin, K.-h., Fang, Y., & Lieber, C. M. (2005). Label-free detection of small-molecule-protein interactions by using nanowire nanosensors. *Proceedings of the National Academy of Sciences of the United States of America, 102*(9), 3208-3212. doi: 10.1073/pnas.0406368102

Wang, X., Li, X., Zhang, L., Yoon, Y., Weber, P., Wang, H., . . . Dai, H. (2009). N-doping of graphene through electrothermal reactions with ammonia. *Science, 324*(5928), 768-771. doi: 10.1126/science.1170335

Wang, Z., Zhang, J., Chen, P., Zhou, X., Yang, Y., Wu, S., . . . Zhang, H. (2011). Label-free, electrochemical detection of methicillin-resistant Staphylococcus aureus DNA with reduced graphene oxide-modified electrodes. *Biosens Bioelectron, 26*(9), 3881-3886. doi: 10.1016/j.bios.2011.03.002

Wasfi, A., & Awwad, F. (2019a, 27-30 Oct. 2019). *First-Principles Modeling for DNA Bases via Z-shaped Graphene Nanoribbon with a Nanogap.* Paper presented at the 2019 IEEE SENSORS.

Wasfi, A., & Awwad, F. (2019b, 21-24 Nov. 2019). *Semi-empirical Modeling for DNA Bases via Z-shaped Graphene Nanoribbon with a Nanopore.* Paper presented at the 2019 IEEE 13th International Conference on Nano/Molecular Medicine & Engineering (NANOMED).

Wasfi, A., Awwad, F., & Ayesh, A. (2019). Electronic signature of DNA bases via Z-shaped graphene nanoribbon with a nanopore. *Biosensors and Bioelectronics: X*, 100011. doi: 10.1016/j.biosx.2019.100011

Wasfi, A., Awwad, F., & Ayesh, A. (2020). DNA sequencing via Z-shaped graphene nano ribbon field effect transistor decorated with nanoparticles using first-principle transport simulations. *New Journal of Physics, 22*(6), 063004. doi: 10.1088/1367-2630/ab87ef

Wasfi, A., Awwad, F., & Ayesh, A. I. (2018). Graphene-based nanopore approaches for DNA sequencing: A literature review. *Biosensors and Bioelectronics, 119*, 191-203. doi: https://doi.org/10.1016/j.bios.2018.07.072

Wen, Y., Xing, F., He, S., Song, S., Wang, L., Long, Y., . . . Fan, C. (2010). A graphene-based fluorescent nanoprobe for silver(i) ions detection by using graphene oxide and a silver-specific oligonucleotide. *Chemical Communications, 46*(15), 2596-2598. doi: 10.1039/B924832C

Weng, L., Zhang, L., Chen, Y., & Rokhinson, L. (2008). Atomic force microscope local oxidation nanolithography of graphene. *Birck and NCN Publications, 93*. doi: 10.1063/1.2976429

Wu, Ding, P., Ye, X., Li, L., He, X., & Wang, K. (2019). One-pot synthesized Cu/Au/Pt trimetallic nanoparticles as a novel enzyme mimic for biosensing applications. *RSC Advances, 9*(26), 14982-14989. doi: 10.1039/C9RA00603F

Wu, M., Kempaiah, R., Huang, P.-J. J., Maheshwari, V., & Liu, J. (2011). Adsorption and Desorption of DNA on Graphene Oxide Studied by Fluorescently Labeled Oligonucleotides. *Langmuir, 27*(6), 2731-2738. doi: 10.1021/la1037926

Wu, X., Mu, F., Wang, Y., & Zhao, H. (2018). Graphene and Graphene-Based Nanomaterials for DNA Detection: A Review. *Molecules, 23*, 2050. doi: 10.3390/molecules23082050

Xin, N., Guan, J., Zhou, C., Chen, X., Gu, C., Li, Y., . . . Guo, X. (2019). Concepts in the design and engineering of single-molecule electronic devices. *Nature Reviews Physics, 1*(3), 211-230. doi: 10.1038/s42254-019-0022-x

Xu, J., Peng, C., Yu, M., & Zheng, J. (2017). Renal clearable noble metal nanoparticles: photoluminescence, elimination, and biomedical applications. *Wiley Interdiscip Rev Nanomed Nanobiotechnol, 9*(5). doi: 10.1002/wnan.1453

Xu, S., Zhan, J., Man, B., Jiang, S., Yue, W., Gao, S., . . . Zhou, Y. (2017). Real-time reliable determination of binding kinetics of DNA hybridization using a multi-channel graphene biosensor. *Nat Commun, 8*, 14902. doi: 10.1038/ncomms14902

Xue, Y., & Ratner, M. A. (2003). Microscopic study of electrical transport through individual molecules with metallic contacts. II. Effect of the interface structure. *Physical Review B, 68*(11), 115407. doi: 10.1103/PhysRevB.68.115407

Yadav, N., Jaiswal, A. K., Dey, K. K., Yadav, V. B., Nath, G., Srivastava, A. K., & Yadav, R. R. (2018). Trimetallic Au/Pt/Ag based nanofluid for enhanced antibacterial response. *Materials Chemistry and Physics, 218*, 10-17. doi: https://doi.org/10.1016/j.matchemphys.2018.07.016

Ye, X., He, X., Lei, Y., Tang, J., Yu, Y., Shi, H., & Wang, K. (2019). One-pot synthesized Cu/Au/Pt trimetallic nanoparticles with enhanced catalytic and plasmonic properties as a universal platform for biosensing and cancer theranostics. *Chemical Communications, 55*(16), 2321-2324. doi: 10.1039/C8CC10127B

Yin, Z., He, Q., Huang, X., Zhang, J., Wu, S., Chen, P., . . . Zhang, H. (2011). Real-time DNA detection using Pt nanoparticle-decorated reduced graphene oxide field-effect transistors. *Nanoscale, 4*, 293-297. doi: 10.1039/c1nr11149c

Zahid, F., Paulsson, M., & Datta, S. (2003). Electrical Conduction through Molecules. *Advanced Semiconductors and Organic Nano-Techniques, 3*. doi: 10.1016/B978-012507060-7/50022-2

Zerner, M. (2007). Semiempirical Molecular Orbital Methods (Vol. 2, pp. 313-365).

Zhai, Q., Xing, H., Fan, D., Zhang, X., Li, J., & Wang, E. (2018). Gold-silver bimetallic nanoclusters with enhanced fluorescence for highly selective and sensitive detection of glutathione. *Sensors and Actuators B: Chemical, 273*, 1827-1832. doi: https://doi.org/10.1016/j.snb.2018.05.145

Zhang, A., & Lieber, C. (2016). Nano-Bioelectronics. *Chemical reviews, 116*(1), 215-257. doi: 10.1021/acs.chemrev.5b00608

Zhang, H., Lu, L., Cao, Y., Du, S., Cheng, Z., & Zhang, S. (2014). Fabrication of catalytically active Au/Pt/Pd trimetallic nanoparticles by rapid injection of NaBH4. *Materials Research Bulletin, 49*, 393-398. doi: https://doi.org/10.1016/j.materresbull.2013.09.025

Zhang, Q., Xie, J., Lee, J. Y., Zhang, J., & Boothroyd, C. (2008). Synthesis of Ag@AgAu Metal Core/Alloy Shell Bimetallic Nanoparticles with Tunable Shell Compositions by a Galvanic Replacement Reaction. *Small, 4*(8), 1067-1071. doi: 10.1002/smll.200701196

Zhang, Z., Ahn, J., Kim, J., Wu, Z., & Qin, D. (2018). Facet-selective deposition of Au and Pt on Ag nanocubes for the fabrication of bifunctional Ag@Au–Pt nanocubes and trimetallic nanoboxes. *Nanoscale, 10*(18), 8642-8649. doi: 10.1039/C8NR01794H

Zheng, G., Patolsky, F., Cui, Y., Wang, W., & Lieber, C. (2005). Multiplexed electrical detection of cancer markers with nanowire sensor arrays. . *Nat Biotechnol, 23*, 1294-1301. doi: 10.1038/nbt1138

Zupan, A., & Causà, M. (2004). Density functional LCAO calculations for solids: Comparison among Hartree–Fock, DFT local density approximation, and DFT generalized gradient approximation structural properties. *International Journal of Quantum Chemistry, 56*, 337-344. doi: 10.1002/qua.560560419

Zwolak, M., & Di Ventra, M. (2005). Electronic Signature of DNA Nucleotides via Transverse Transport. *Nano Letters, 5*(3), 421-424. doi: 10.1021/nl048289w

Zwolak, M., & Di Ventra, M. (2007). Colloquium: Physical approaches to DNA sequencing and detection. *Reviews of Modern Physics, 80*. doi: 10.1103/RevModPhys.80.141

List of Publications

Journals

Wasfi, A., Awwad, F., & Ayesh, A. I. (2018). Graphene-based nanopore approaches for DNA sequencing: A literature review. *Biosensors and Bioelectronics*, 119, 191-203. doi: 10.1016/j.bios.2018.07.072. https://www.sciencedirect.com/science/article/abs/pii/S0956566318305839

Wasfi, A., Awwad, F., & Ayesh, A. (2019). Electronic signature of DNA bases via Z-shaped graphene nanoribbon with a nanopore. *Biosensors and Bioelectronics: X*, 100011. doi: 10.1016/j.biosx.2019.100011. https://www.sciencedirect.com/science/article/pii/S2590137019300019

Wasfi, A., Awwad, F., & Ayesh, A. (2020). DNA sequencing via Z-shaped graphene nano ribbon field effect transistor decorated with nanoparticles using first-principle transport simulations. *New Journal of Physics*, *22*(6), 063004. doi: 10.1088/1367-2630/ab87ef . https://iopscience.iop.org/article/10.1088/1367-2630/ab87ef

Wasfi, A., Awwad, F., & Ayesh, A. I. (2021). Detection of DNA Bases via Field Effect Transistor of Graphene Nanoribbon with a Nanopore: Semi-empirical Modeling. *IEEE Trans Nanobioscience*, PP. doi: 10.1109/TNB.2021.3077364. https://ieeexplore.ieee.org/document/9422753

Conferences

Wasfi, A., & Awwad, F. (2019a, 27-30 Oct. 2019). First-Principles Modeling for DNA Bases via Z-shaped Graphene Nanoribbon with a Nanogap. Paper presented at the 2019 IEEE SENSORS. https://ieeexplore.ieee.org/document/8956659

Wasfi, A., & Awwad, F. (2019b, 21-24 Nov. 2019). Semi-empirical Modeling for DNA Bases via Z-shaped Graphene Nanoribbon with a Nanopore. Paper presented at the 2019 IEEE 13th International Conference on Nano/Molecular Medicine & Engineering (NANOMED). https://ieeexplore.ieee.org/document/9130612